Computational Studies of Cation and Anion Ordering in Cubic Yttria Stabilized Zirconia

by

Ashley P. Predith

Submitted to the Department of Materials Science and Engineering
in partial fulfillment of the requirements for the degree of

Doctor of Philosophy

at the

MASSACHUSETTS INSTITUTE OF TECHNOLOGY

June 2006

Author .....
Department of Materials Science and Engineering
April 28, 2006

Certified by 5/3/2006
Gerbrand Ceder
R.P. Simmons Professor of Materials Science and Engineering
Thesis Supervisor

Accepted by .....
Samuel M. Allen
POSCO Professor of Physical Metallurgy
Chairperson, Department Committee on Graduate Students

Computational Studies of Cation and Anion Ordering in Cubic Yttria Stabilized Zirconia

by

Ashley P. Predith

Submitted to the Department of Materials Science and Engineering
on April 28, 2006, in partial fulfillment of the
requirements for the degree of
Doctor of Philosophy

Abstract

The investigation of ordering and phase stability in the ZrO_2-Y_2O_3 system involves two sets of calculations. The first set of calculations uses the cluster expansion method. A guide to the practical implementation of the cluster expansion outlines methods for defining a goal and choosing structures and clusters that best model the system of interest. The cluster expansion of the yttria stabilized zirconia system considers 447 configurations across the ZrO_2-Y_2O_3 composition range. The effective cluster interaction for pair clusters show electrostatic repulsion between anions and little interaction between cations. Triplet anion terms largely modify the energy contributions of the pair terms. Separate cluster expansions using structures at single compositions show that cation clusters become more important at high yttria composition.

The cluster expansion led to the discovery of three previously unidentified ordered ground state structures at 25, 29, and 33 % Y on the cubic fluorite lattice. The ground state with 33 % Y is stable with respect to the calculated energies of monoclinic ZrO_2 and the $Y_4Zr_3O_{12}$ ground state. The ground states have the common ordering feature of yttrium and vacancies in [1 1 2] chains, and Monte Carlo simulations show that vacancy ordering upon cooling is contingent on cation ordering.

The second set of calculations consider three driving forces for order: ionic relaxation, vacancy arrangements, and differences in Zr and cation dopant radii. Bond valence sums of fully relaxed and anion relaxed structures are nearly equal at all compositions. In supercells of ZrO_2, the vacancy arrangement of the ground state with 25 % Y is more stable than arrangements maximizing the distance between vacancies or aligning vacancies in [1 1 1]. Comparing the YSZ ground state with structures of the same configuration with scandium replacing yttrium shows different stable phases on the convex hull between cubic ZrO_2 and the dopant M_2O_3 phase. The change in the stability of the configurations may be a result of cation radius sizes. The factors suggest that the driving forces of phase stability depend on composition.

Thesis Supervisor: Gerbrand Ceder
Title: R.P. Simmons Professor of Materials Science and Engineering

Acknowledgments

I first thank my advisor Gerd Ceder . His contagious enthusiasm for science was energizing during the course of study. I appreciated his scientific insight and suggestions about how to analyze and approach this research.

Professors Nicola Marzari and Harry Tuller on my thesis committee had useful suggestions and provided thoughtful discussion.

Early work on the cluster expansion of YSZ was done in collaboration with Chris Wolverton and Alex Bogicevic of Ford Motor Company. Their initial work provided a foundation for the work in this dissertation.

My work also depended on the efforts of past and current members of the research group. The ways people contributed covered the gamut from the physical acts of setting up and maintaining computer systems, to helping sort out VASP issues, giving advice on classes, to late night camaraderie and conversations in lab. While only names are listed here, each person has a unique face and personality very much part of my time in the group: Eric Wu, Chris Marianetti, Elena Arroyo, Dane Morgan, John Reed, Dinesh Balachandran, Anton van der Ven, Stefano Curtarolo, Kristin Persson, Matteo Cococcioni, Shirley Meng, Byungchan Han, Kisuk Kang, Tim Mueller, Chris Fischer, Maria Chan, Fei Zhou, Byoungwoo Kang, Yoyo Hinuma, Thomas Maxisch, Kevin Tibbetts, Caetano Miranda, Lei Wang, Osman Okan, and Kathy Simmons.

The cluster expansion of YSZ was done with the assistance of Anton van der Ven and Tim Mueller. Tim delved in to the cluster expansion process, offering a fresh perspective and succinct approach, and Anton's stream of ideas as well as his readiness and patience in answering questions was met with gratitude by me and many others. I especially thank Kristin Persson for frank analysis of the calculations and for sharing her experience on many levels. Talking with her about the process of research has been greatly valued.

In addition to the people in lab, I was fortunate for the emotional and spiritual support of friends. The large apartment that I lived in housed many people during my time there, and my roommates made it a quirky, interesting place to come home to

after a long day at the computer. Holly Krambeck, Ben Paxton, Max Berniker, Bonna Newman, Megan Carroll, and Ayala Wineman particularly made our apartment a great place to live.

I am thankful to many for their friendship, and I could not name everyone here explicitly. Doug Twisselmann, Douglas Cannon, Bruce Constantine, and Andy Martinez were there from the very beginning. Elizabeth Daake, Shawn Kelly, Christina Silcox, and Joaquin Blaya joyfully celebrated holidays and events with me, and Maureen Long, Christine Ng, Elizabeth Basha, and I experimented our way through many happy dinners. Michael Steinberger enriched my experience in multiple ways. The Tech Catholic Community provided a fantastic environment in which to question, learn, and grow. I thank Paul Reynolds for his caring presence that was steadily felt over the years.

Throughout classes, qualifying procedures, research, teaching, nieces, and nephews, Marc Richard was with me throughout grad school. Jenny Lund was always ready for long talks on the telephone or for heading out on our next trip. Whether listening as I vented about things I was struggling with or making me laugh so that I literally could not walk, Maria Chan has been a genuine and indispensible friend over the past two years. I sincerely thank you, Maria.

Finally, my family. They each had a unique role that contributed to me finishing this dissertation, and I am grateful for their presence and love. Unfailingly listening, supporting, and cheering me on, my mom Patty Predith has been there every step of the way. My dad Jim Predith shares my interest in science and dared to ask more than once for an explanation of what I was working on. My brother and my niece Colin Predith and Meera Kypta and my sister, brother-in-law, and nephew Hilary, Brad, and Brendan Smith gave me a balanced perspective on life and helped me keep an eye on the future. Thank you so much.

The words of family, friends, coworkers, and the wider community made all the difference during my time in graduate school. The path was at times solitary and difficult, at times enlightening and deeply satisfying. Having little previous knowledge of Eleanor Roosevelt, I accidentally discovered her writings and found them to be

particularly meaningful:

"The encouraging thing is that every time you meet a situation, though you may think at the time it is an impossibility..., once you have met it and lived through it you find that forever after you are freer than you ever were before... You gain strength, courage, and confidence by every experience in which you really stop to look fear in the face...

Courage is more exhilirating than fear and in the long run it is easier. We do not have to become heroes overnight. Just a step at a time, meeting each thing that comes up, seeing it is not as dreadful as it appeared, discovering we have the strength to stare it down."

"You must do the thing you cannot do."

Contents

List of Figures

List of Tables

Chapter 1

Introduction

Yttria-stabilized zirconia (YSZ) is an important material for its use as an oxygen ion conductor. An understanding of the interaction among ionic species in the ZrO_2-Y_2O_3 system would be useful for optimizing the material's conductivity. The computational studies in this dissertation show that the ZrO_2-Y_2O_3 system exhibits stable, ordered ground state structures and that driving forces contributing to phase stability depend on composition: oxygen relaxation contributes to stability at low compositions of yttria, and the arrangement of cations contributes to stability at high compositions of yttria.

1.1 Conductivity

Pure monoclinic zirconia exhibits negligible oxygen ion conductivity, but with the addition of yttria, the system takes a cubic fluorite structure. The oxygen conductivity increases to reach a maximum of 10^{-1} $(\text{ohm} \cdot \text{cm})^{-1}$ at 1000 K with 15-18 % $YO_{1.5}$ (8-10 % Y_2O_3) [3, 4]. With the addition of 20 % more $YO_{1.5}$ doping, the conductivity decreases by an order of magnitude. Numerous computer modelling studies have attempted to explain the mechanism of diffusion in doped zirconias and the reason for a peak and subsequent decrease in conductivity with more doping v[5, 6, 7, 8, 9].

For each Y_2O_3 molecule added to ZrO_2, one vacancy forms to maintain charge balance in the material. As yttria is added to zirconia, the concentration of vacan-

cies, and hence available oxygen hopping sites, increases. The conductivity, however, decreases. One possible explanation involves the oxygen diffusion pathway. Oxygen ions diffuse along pathways between two cation sites, and studies suggest a pathway between two large yttrium ions is unfavorable [5, 8]. As the composition of the material increases above 15-18 % $YO_{1.5}$, the Y-Y unfavorable pathways inhibit conductivity. Another possible explanation for the decrease in conductivity is the ordering of oxygen vacancies. A driving force for order would resist oxygen hopping in to ordered vacant sites. Evidence exists for short range order of vacancies [10].

1.2 Structure and phases

Pure zirconia and yttria have fluorite based structures. The cubic fluorite structure has cations on face centered cubic positions and anions in the tetrahedral interstices of the fcc lattice (figure 1-1). Another representation of the structure is to consider anions in a simple cubic array with a cation inside every other oxygen cube. Each cation site has eight nearest neighbor anion sites, and each anion site has four nearest neighbor cation sites.

Pure ZrO_2 is cubic fluorite at high temperatures. From the cubic fluorite structure, zirconia transforms to a tetragonal structure at 2350 °C. The tetragonal structure is a result of a distortion of the oxygen sublattice along the X_2^- mode of vibration, which causes [0 0 1] rows of oxygen to be offset alternately up or down with respect to the fcc cation lattice [11]. Continued cooling yields the monoclinic ground state structure at 1100 °C. The monoclinic structure is a further distortion of the cubic fluorite structure such that each zirconium has seven oxygen at the nearest neighbor positions.

The structure of pure yttria is the C-type lanthanide structure, where the letter C is an abbreviation for cubic. The structure is based on cubic fluorite, but one-fourth of the anion sites are vacant. The conventional unit cell is body centered cubic with 80 atoms. One way to visualize the vacancy arrangement in C-type structure is that the vacancies align along four nonintersecting $\langle 1\ 1\ 1 \rangle$ chains so that every yttrium has

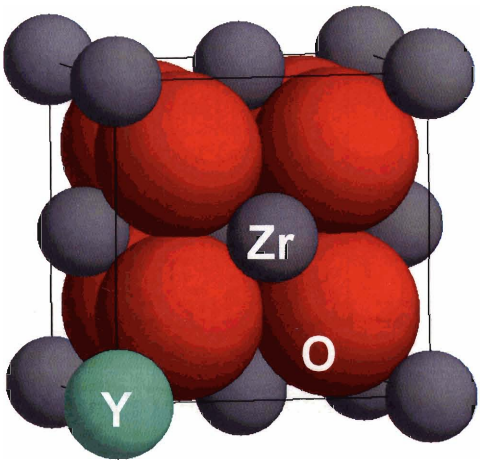

Figure 1-1: The cubic fluorite structure has cations (Y, Zr) on fcc sites and oxygen and vacancies in tetrahedral interstices. The light green cation is yttrium, which is 0.2 Å larger in radius than zirconium in grey.

six oxygen nearest neighbors [12]. The structure may also be visualized as a set of 64 simple anion cubes (a 4x4x4 array) with yttrium filling half of the cubes. Three-fourths of the cubes have two vacancies at face diagonal positions and one-fourth have two vacancies at cube diagonal positions.

When yttria is added to zirconia, the monoclinic zirconia transforms to tetragonal and then cubic fluorite. The term yttria-stabilized zirconia refers to the cubic fluorite phase of zirconia, which is stabilized over the monoclinic structure as a consequence of incorporating yttria. At compositions between pure ZrO_2 and pure Y_2O_3, experiments have verified the existence of one ordered structure with stoichiometry $Y_4Zr_3O_{12}$ [13, 14]. In materials with low yttria (less than 50 % $YO_{1.5}$) concentration, ongoing research investigates the driving forces for short range order of cations and anions. Some studies suggest that phase separation between pure yttria and another ordered compound may occur at compositions between $Y_4Zr_3O_{12}$ and pure yttria [15, 16, 17, 18], but other investigations do not confirm those findings[19, 20, 21, 22].

The compositions of the materials discussed in this dissertation are written with respect to the percentage of $YO_{1.5}$. Useful references are the conversion factors be-

tween % $YO_{1.5}$ and % Y_2O_3:

$$x_{YO_{1.5}} = \frac{2 * x_{Y_2O_3}}{1 + x_{Y_2O_3}} \tag{1.1}$$

$$x_{Y_2O_3} = \frac{x_{YO_{1.5}}}{2 - x_{YO_{1.5}}} \tag{1.2}$$

1.3 Investigations of order and phase stability

This work investigates the ordering and phase stability across the ZrO_2-Y_2O_3 composition range. The calculations show the presence of stable, ordered ground states on the cubic fluorite lattice and composition-dependent driving forces for phase stability. Chapters 2 and 3 describe the cluster expansion technique and its application to the yttria stabilized zirconia system. Chapter 2 is a practical guide for implementing a cluster expansion, and chapter 3 presents the cluster expansion of YSZ. The cluster expansion has led to the identification of previously unknown ordered ground states. An evaluation of the ground state structures in chapter 4 shows the relationships among their atomic ordering and electronic structure.

Chapter 4 also offers insight in to the driving forces for stability in YSZ. Three parts of the chapter describe the complex nature of ordering: a survey of the literature on ordering and phase stability, an analysis of how the cation coordination and relaxation around oxygen varies across the composition range, and Monte Carlo calculations of the configurational changes of one ground state with temperature. Chapter 5 parses some factors that are important for understanding phase stability and quantifies the impact of oxygen relaxation, vacancy ordering, and cation size on the stability of the ground states.

Chapter 2

Cluster expansion implementation

2.1 Developing a cluster expansion

A cluster expansion is a method to model the energetics of a material using insight from both physics and statistics. A cluster expansion in theory provides an exactly converging expression of the energy in terms of configuration variables; in practice, complex systems require the cluster expansion to be optimized for a specific purpose rather than providing the exact energy convergence. This chapter offers a guide for defining the purpose a cluster expansion, methods for choosing structures and clusters to be included in the fit, and metrics for analyzing the results.

Section 2.1 defines the cluster expansion and suggests common purposes. Section 2.2 describes metrics like rms error and cross validation score to quantify how well the fit reproduces the original data, and section 2.3 details factors for consideration or methods that can be employed to choose the structures and clusters used for implementation. Comparing the implementation and results with the purpose of the fit determines whether the cluster expansion is complete.

2.1.1 Cluster expansion background

The main achievement of the cluster expansion formalism is to rigorously quantify the configurational disorder of a system by an orthogonal expansion of basis functions.

This is accomplished by parameterizing the energy in terms of the atom types placed on lattice sites. Given a structure with two components, an Ising lattice provides a model for the lattice sites of the solid. To compare different configurations of atoms within a single material system, all structures must map on to the same Ising lattice type. A spin variable, σ_i, of +1 or -1 denotes what type of atom is on each site i.

Rather than specifying the type of atom on each lattice site within a particular structure, a complete set of orthonormal basis functions can also specify the configuration of a structure. The basis functions called *cluster functions* are polynomials of the discrete variables σ_i. A cluster function, α, is the product of the spin variables at one or more sites. The cluster of just one σ site is called a point cluster. A cluster of two sites is called a pair. A cluster of three sites is a triplet. To simplify the cluster expansion, one can group together clusters that are symmetrically equivalent. If a cluster can be mapped on to one another cluster by operation of one or more symmetry elements of the parent structure, the two clusters belong in the same group called an orbit Ω_α. The average of the spin variable products over all the clusters in the orbit is given by

$$\langle \phi_\alpha(\vec{\sigma}) \rangle = \frac{1}{N} \sum_{\beta \in \Omega_\alpha} \phi_\beta(\vec{\sigma}) \tag{2.1}$$

where N is the number of clusters β in the orbit. $\langle \phi_\alpha(\vec{\sigma}) \rangle$ are called the correlation functions.

Using the cluster functions as the basis for the expansion of the energy, the parameterization of the energy takes the form

$$E(\sigma) = \sum_\alpha m_\alpha V_\alpha \phi_\alpha \tag{2.2}$$

$$m_\alpha = \frac{N}{N_p} \tag{2.3}$$

where m_α is the multiplicity of cluster α and N_p is the number of Bravais lattice points. The coefficients of the expansion V_α are the *effective cluster interactions* (ECI). The cluster expansion is an exact expansion of the energy. Truncating the expansion introduces error. In matrix notation, the cluster expansion becomes a

mathematical fit:

$$\mathbf{E_m} = \mathbf{X_{mxn}} \mathbf{V_n} \tag{2.4}$$

where $\mathbf{E}_m$ is a vector of m structural energies, $\mathbf{X}_{mxn}$ is a matrix of the n correlations for each m structures, and $\mathbf{V}_n$ are the n ECI to be fitted. An excellent summary of the cluster expansion formalism is available in A. van der Ven's thesis [23] and a thorough review is in a book chapter by D. de Fontaine [24].

2.1.2 Purpose of the cluster expansion

The task of someone implementing a cluster expansion is how to choose clusters α and structures (and hence their energies E) for equation 2.2 to create a useful model. The primary result of the cluster expansion is the set of ECI. Since the expansion is exact, the theoretical values of the ECI depend on the overall energetics of the system, but in practice, the truncation of the expansion and the particular cluster functions and structural energies chosen for the fit will determine the specific ECI values obtained. By defining one or more purposes for the cluster expansion, choices during the development of the cluster expansion will guide one to obtain useful results. A cluster expansion has many potential purposes:

- to predict and identify the ground state structures at one or more compositions
- to function as a Hamiltonian for Monte Carlo to model relative phase stability in a specific temperature range (for phase diagram calculations, for example)
- to infer local contributions to a structure's energy and hence driving forces for order/disorder
- to accurately represent the energetics of structures in a particular energy range

Referring to the last item in the list as an example, to go from a statement of purpose to the implementation of the cluster expansion, one must be specific and quantitative. What structures are 'representative' of the system? How many structures are

necessary? What cluster functions give the degrees of freedom necessary for 'representative' energetics? What metric defines an accurate representation: a small difference between the calculated and fitted energies or ECI values following physically rational behavior?

To help answer questions like these, the following sections suggest quantitative measures of accuracy and suggest methods to choose structural energies and clusters for modeling a system of interest. Experience with the cluster expansion of yttria stabilized zirconia provided a foundation of thought and experience for this chapter. For details on the cluster expansion of YSZ, see chapter 3.

2.2 Metrics of the expansion

A cluster expansion is a fit of structural energies to the correlation variables that describe the structures' configurations. The structures included in the fit are a subset of all possible configurations of the system. Metrics quantifying the errors of the cluster expansion help evaluate the usefulness of the resulting fitted ECI. Two systematic types of error can arise in a cluster expansion: the differences between the calculated energies and fitted energies within the subset structures of the expansion and the differences in ECI between the whole set of configurations of the system and the subset of structures included in the fit. Throughout this thesis, the definition of the *calculated* energy is the energy of a structure calculated with DFT, electrostatic, potential model calculations, or other total energy methods. The *fitted* energy of a structure is the energy found by multiplying the fitted ECI with the correlations of the structure.

Consider the difference between the calculated and fitted energies of the structures in the fit. As more cluster functions are included in the cluster expansion, the fitted energies converge upon the calculated energies [24]. A cluster expansion in practice, however, truncates the fit to a finite number of clusters. Removal of clusters that would further converge the fit cause an error called *bias* in the fitted ECI. Now consider the error called *variance*; it is the statistical deviation around a mean value.

As the number of structures in the sample increases, the mean of the sample converges to the mean of the whole population of structures. The average deviation from the mean, however, is sensitive to the particular energies and correlations in the fit. That deviation is the variance. The four metrics below help quantify the errors in the fit.

2.2.1 Root mean squared error

The residual error of a structure's energy is the difference between the calculated energy, E_i, and the fitted energy $\hat{E}_i$. The root mean squared (RMS) error of the fit is the average of the squared residual error of all the structures

$$\text{RMS error} = \sqrt{\frac{\sum_{i=1}^{N}(E_i - \hat{E}_i)^2}{N}} \tag{2.5}$$

RMS error is the simplest estimation of goodness of fit for the set of structures in the cluster expansion. It does not measure the ability of the cluster expansion to predict the energies of structures not in the fit.

2.2.2 Cross validation score

The cross validation score measures the ability of the cluster expansion to predict the energy of a structure left out of the fit. In leave-one-out (n=1) cross validation (cv), one removes a single structure from the fit, uses the remaining structures to obtain ECI, and calculates the residual error on the energy of the removed structure. The procedure is done successively for every structure in the fit. The average root mean squared error of all the residual errors is the cv score.

2.2.3 ECI error

In the least squares fit, a standard error of the fitted ECI arises when there are more structural energies than clusters included in the fit. The fitted ECI minimize the difference between the fitted energies and the calculated energies for all the structures.

The standard error of the ECI, $s_{\vec{V}_i}$ is

$$s_{\vec{V}_i} = (s^2_{\vec{E}_i} * c_{ii})^{1/2} \tag{2.6}$$

$s^2_{\vec{E}_i}$ is the estimated variance of the energy residuals

$$s^2_{\vec{E}_i} = \frac{\sum_{i=1}^{N} \left(E_i - \hat{E}_i\right)^2}{n-k} \tag{2.7}$$

where n is the number of energies in the fit and k is the number of ECI. The c_{ii} are the variances of the ECI. A derivation of the ECI variance is in Appendix A, and the covariance subsection of section 2.3.1 discusses this further.

The appendix explains that each row of the matrix $\mathbf{X}$ contains the correlations for the clusters in one structure, and c_{ii} are the diagonal elements of the matrix $(\mathbf{X}^T\mathbf{X})^{-1}$. If the correlations of the structures have high covariance with each other, then the $\mathbf{X}^T\mathbf{X}$ matrix will approach singularity. As the matrix approaches singularity, the values of c_{ii} will increase indicating that the ECI estimates may be imprecise, and the fitted ECI will deviate from the theoretical ECI.

2.2.4 Cluster expanded energy of trial structures

One useful capacity of a cluster expansion is the ability to quickly obtain estimated energies for uncalculated structures. Given the ECI from a set of fitted structures, one can calculate an approximate energy using the fitted ECI and the correlations for the structure of interest that was not included in the cluster expansion. If the purpose of the cluster expansion includes searching for ground state configurations, knowing approximate energies of unfitted configurations accelerates the search process. High energy structures may be discounted if they are not considered candidate ground states. The cv score offers a predictive measure of the fit using the energies and correlations already in the cluster expansion. Calculating the energy of a set of trial, unfitted structures with the ECI of a fitted sample set offers a predictive measure of the energies in the correlation space not in the fit. The set of trial structures

may be orders of magnitude larger than the set of fitted structures. If some trial structures have energies below the convex ground state hull, these trial structures may potentially be ground state configurations (figure 2-1).

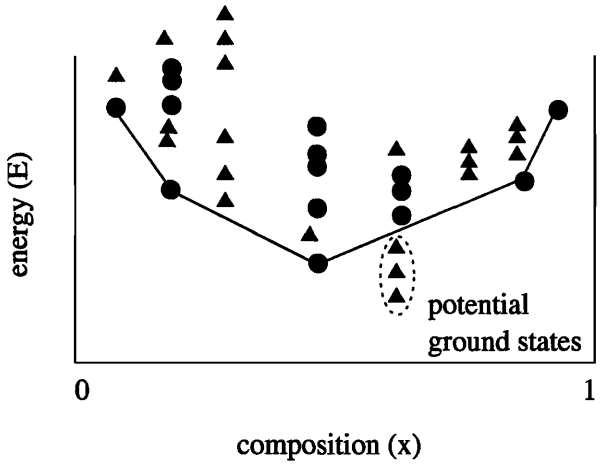

Figure 2-1: Calculating energies of trial structures using the ECI of the fitted configurations can be useful to identify potentially stable structures. Circles denote fitted energies of structures in the cluster expansion. Triangles represent estimated energies of trial structures calculated from ECI. Using DFT or other total energy method, one can calculate the energies of the potential ground state structures (triangles) to determine if one is a true ground state.

2.3 Factors for implementation

Two approaches exist for determining what clusters and structures to include in the cluster expansion. One approach involves choosing clusters and structures that have particular physical or statistical characteristics with the desire that they will adequately model the system. The other approach involves selecting clusters and structures regardless of their individual properties until the final fit has particular statistical characteristics. The two approaches ideally converge on the same solution,

although praxis shows this convergence is not guaranteed.

2.3.1 Cluster choice

In the practice of putting together a cluster expansion, the number of distinct clusters possible to enumerate on a lattice is 2^N, where N is the number of lattice sites. The number of structures for which it is possible to calculate energies is limited by computational resources. Since fitting a larger number of clusters to a fewer number of energies creates an undetermined fit, truncating the cluster expansion to include a subset of the possible cluster functions gives a more rigorous set of ECI. The decision to include a particular cluster in the fit depends on whether it has a desirable physical arrangement of the points in the cluster or whether the cluster's correlations have a desirable affect on the quantitative metrics of the fit. All of the methods described below, except the last one, select clusters based on their physical or statistical properties. The last method follows an outcome approach that chooses clusters arbitrarily to minimize the cross validation score of the final fit.

Including subclusters

A common property of convergent cluster expansions is that every *subcluster* of each included cluster is in the expansion. The subclusters of a pair are the pair clusters that are smaller in range. Figure 2-2 gives an example.

Covariance between clusters

According to standard statistical fitting practice, when variables are highly covariant, the coefficients of those variables do not represent the independent contribution of each variable to the observation. In a cluster expansion, the observation is the calculated energy of the structure. The *covariance* between two clusters is the degree to which the variance of the correlations of one cluster moves with the same sign, opposite sign, or independently of the variance of the correlations of another cluster

$$cov(x_i, x_j) = \langle (x_i - \mu_i)(x_j - \mu_j) \rangle \tag{2.8}$$

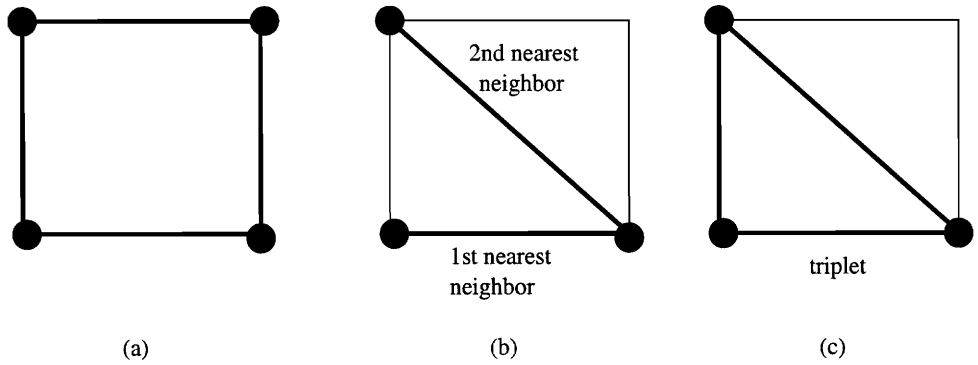

Figure 2-2: The square cluster in (a) has three subclusters: the pair subclusters in (b) and the triplet in (c).

x_i and x_j are two sets of correlations, and μ_i and μ_j are the sample means of x_i and x_j. When $\text{cov}(x_i,x_j) > 0$, then x_j tends to increase when x_i increases. When $\text{cov}(x_i,x_j) < 0$, then x_j tends to decrease when x_i increases. When $\text{cov}(x_i,x_j) = 0$, the correlations are independent. In statistical fitting, independent variables provide the most explanatory power. A cluster expansion, however, is not a pure statistical fit of data. As Sanchez shows, a convergent solution to fitting cluster functions to the energies is possible [25]. In the whole configuration space, the correlations of the clusters create an orthogonal set of vectors. When considering a finite set of correlations for the structures in a cluster expansion, however, subclusters can be highly covariant with their parent cluster. Since the subclusters can, in practice, add covariance to the matrix of correlations, a physical cluster expansion and a statistical fit may be at odds with each other. Note that in statistical literature, the covariance normalized by the product $\sigma_i\sigma_j$ is called the correlation between x_i and x_j, where σ_i and σ_j are the variances of x_i and x_j. The statistical correlation between x_i and x_j is different from the cluster expansion correlation defined earlier in equation 2.1. The term correlation in this thesis always refers to the cluster expansion correlation unless specifically noted otherwise.

Analytical terms

In the standard construction of the cluster expansion, the formation energies of a set of configurations are fit to the correlations of clusters defined by geometrical point arrangements. Subtracting off a known, analytical portion of the energy from the formation energy may improve convergence by removing a degree of freedom from the energies to be fit by the correlations. The electrostatic energy between point charges on a periodic lattice, for example, has been worked out in an Ewald sum [26]. The real space Ewald term E_r is

$$E_r = \frac{1}{2}\sum_{i,j} q_i q_j \frac{erfc(\alpha r_{ij})}{r_{ij}} \tag{2.9}$$

Subtracting off E_r from the energy is analogous to adding a term to the cluster expansion

$$E(\sigma) = V_0 + \sum_i m_i V_i \phi_i(\sigma) + V_k \sum_j m_j \phi_j^{pair}(\sigma) \frac{erfc(\alpha r_i)}{r_i} \tag{2.10}$$

where the last term of equation 2.10 is a weighted sum of the pair correlations. ϕ_j^{pair} are the pair correlations, α is a damping parameter, and r_i is the distance between two points in the i^{th} pair cluster.

Another example of accounting for portions of the energy analytically is in the mixed space cluster expansion (MSCE) [27, 28, 29]. MSCE uses the traditional correlations and ECI for all clusters except the pair terms. Employing earlier work on reciprocal-space expansions [30], it uses the Fourier transforms of the ECI and correlations for the pair terms.

$$E_{notpairs}(\sigma) = \sum_i m_i V_i \phi_i(\sigma) \tag{2.11}$$

$$E_{pairs}(\sigma) = \sum_k V_{pair}(k) |S(k,\sigma)|^2 \tag{2.12}$$

The expansion includes a third term to account for the *constituent strain energy.*

The constituent strain (cs) energy, $\Delta E_{cs}^{eq}(\mathrm{x},\hat{k})$, is the energy necessary to maintain coherency at an interface between regions of each pure component. It depends on the orientation $\hat{k}$ of the interface.

$$E_{cs} = \sum_{k} \frac{\Delta E_{cs}^{eq}(x,\hat{k})}{4x(1-x)} |S(k,\sigma)|^2 F(k) \tag{2.13}$$

Minimizing cross validation score

The previous approaches in section 2.3.1 use a building approach of choosing clusters, whereby clusters are first chosen by their physical or geometrical significance without knowing the final impact on the metrics of the expansion. Outcome approachs are possible that iteratively choose clusters in an arbitrary manner to optimize an aspect or metric of the final cluster expansion. The statistical literature explains the use of leave-one-out cross validation (cv), Mallow's C_p [31] and Akaike's Information Criterion (AIC), as well as describing the bootstrap and jackknife methods [32], for choosing variables/clusters. These five methods are asymptotically equivalent [33, 34].

Li [35] and Shao [36] discuss the use of cross validation methods to choose variables for the best predictive model of a system. Li proves, and van de Walle [37] summarizes, that if the number of observations (structural energies) in the fit increases as the number of variables (clusters) added to the model increases, minimizing the cross validation score finds the the optimal, most predictive model. Van de Walle explains this result using the decomposition of the expected squared error of the cluster expanded energy. A paraphrase of his explanation gives the essential details [37]:

If y_i is the energy of a structure with correlation vector X_i. Each correlation vector X_i contains k elements, one for the average value of each cluster in structure i. $\hat{y}_i$ is the predicted energy of structure i from the cluster expansion of N total structures. A decomposition of the expected squared error gives

$$\left\langle (\hat{y}_i - y_i)^2 \right\rangle = \left\langle (y_i - \langle y_i \rangle)^2 \right\rangle + \left\langle (\hat{y}_i - \langle y_i \rangle)^2 \right\rangle - 2 \left\langle (y_i - \langle y_i \rangle)(\hat{y}_i - \langle y_i \rangle) \right\rangle \tag{2.14}$$

The first term is called the bias term, the second term is called the variance term,

and the last term is the covariance term. In a least squares fit of the N structural energies, the covariance term will be positive and increase as $\frac{k}{N}$ increases. The expected error is therefore sensitive to the number of clusters and structures in the fit, regardless of their individual characteristics. Consider if $\hat{y}_i$ is replaced by $\hat{y}_{i-cv}$, which is the energy of structure i predicted from a cluster expansion of all structural energies except the energy of i (hence N-1 structures in total). Now the covariance term goes to zero, and the change in the variance term goes to zero as N increases. This provides more accurate predictive power. The CV score is the sample average of $(\hat{y}_{i-cv} - y_i)$.

The remaining step is to choose a procedure for adding variables most efficiently to the model. The literature lists several methods: forward selection, backward elimination, stepwise, branch-and-bound, and simulated annealing [32]. Of greatest interest is simulated annealing because of its use as a search method in global minimization problems. Based on Monte Carlo simulations, adding or subtracting a cluster to the cluster expansion will increase or decrease the cv score. When the cv score decreases, the cluster is accepted. When the cv score increases, the cluster is accepted if the probability of it occuring is greater than a randomly chosen number. The author acknowledges Tim Mueller for proposing the Monte Carlo approach of choosing structures.

2.3.2 Structure choice

The calculated energies of structures are the computational observations that lead us to make conclusions about a system's configurational behavior. In standard statistical practice, the sample of a population is a random selection of data points from a whole population. In the cluster expansion, the fit of ECI is not a pure statistical process, and randomly selecting structures may not be the best approach to model a system's configuration. Since the ECI are a convergent series to the exact solution, random selection will invariably lead to the selection of large supercell structures. Existing computers cannot calculate large supercell structures (10^3-10^4 atoms or larger, depending on energy method) in an acceptable amount of time; therefore, calculating

large structures may not be feasible modelling option. Depending also on the purpose of the cluster expansion, all structures of a given system may not be of interest. Inherent in the selection of structures is the decision about whether to choose structures that either widely sample or narrowly sample the available correlation space.

The first four methods below choose structures for the fit based on the structures' physical characteristics. The sections on sensitivities and orthogonality use an approach that chooses structures based on their correlations to directly create a cluster expansion modelling a particular range of correlation space. The last section on weighting describes an approach to add elements to the energy vector and correlation matrix to optimize the cluster expanded convex hull outcome.

Structures by energy

Structures may be sorted by their formation energy. Structures with a high formation energy are unlikely to stabilize experimentally, while structures with a low formation energy are more likely to be stable or metastable phases. Low energy structures model the configurational landscape near the convex hull. One approach in a successful cluster expansion was to include only low energy structures near the convex hull in the fit [38].

Supercell size

The structures that model a material system come from configurations of atoms on various supercells of the primitive lattice unit cell. Small supercell sized structures have simple ion geometries due to the few number of sites for repetition, and larger supercell structures have more complicated geometries. Small sized structures may model some material systems well, while other systems may require large structures. Including complicated geometries adds additional complexity for the cluster expansion to model.

Along with the geometrical attributes of supercell sizes is the effect of choosing different compositions. The supercell size limits the number of compositions that the cluster expansion models. The number of compositions that can be modelled may be

important if many structures at small composition increments are stable (a Devil's staircase) [39].

Experimental information

Experiments on the system of interest can yield clues about what the expected ordering and ground state structures are and guide the selection to a group of possible ordered structures [40].

Cluster expanded predicted structures

Estimating energies of uncalculated trial structures is possible using the coefficients of the cluster expansion. When the cluster expanded energy is lower than the hull of the current fit, the structure may have a true, calculated energy that is also below the hull. To predict the ground state structures of the system, that potential structure needs to be calculated to verify its energy. With enough iterations, this method can find previously unidentified ground state structures, if they exist. Section 2.2.4 also discusses the approach.

Sensitivities

One way to quantify the range of correlation space sampled by the structures' correlations is to use singular value decomposition (SVD). The SVD of the $\mathbf{X}$ matrix of correlations decomposes it into

$$\mathbf{X} = \mathbf{USV^T} \tag{2.15}$$

where the columns of $\mathbf{U}$ are an orthonormal basis of the columns of $\mathbf{X}$, the rows of $\mathbf{V^T}$ are an orthonormal basis of the rows of $\mathbf{X}$, and the elements of the diagonal matrix $\mathbf{S}$ are the singular values [41]. The singular values indicate how the correlations sample the available correlation space. If the singular values are nearly equal, the correlations sample space evenly. If the singular values contain some very large and some very small values, the correlations for those clusters narrowly sample and widely sample correlation space.

Notice that one method to solve equation 2.15 is with

$$\mathbf{X^T X} = \mathbf{V S^2 V^T} \tag{2.16}$$

where by diagonalizing $\mathbf{X^T X}^{-1}$ (the covariance matrix) gives $\mathbf{S}$ and $\mathbf{V}$. The *sensitivities* are the diagonal elements of the $(\mathbf{X^T X})^{-1}$ matrix, as shown in equation A.3. The sensitivities relate how much the correlations vary with each other and hence are directly related to the singular values. A small value of the sensitivity for a cluster signifies that the correlations vary greatly with each other and the correlation space is not widely sampled. The author acknowledges Chris Fischer for proposing the sensitivity approach of choosing structures.

Orthogonalizing configuration space

If the widest possible correlation space is desired, one approach is to include structures that are most orthogonal to the current space of structures. SVD is one technique for determining the structure that is most orthogonal to the current space of correlations [42]. The singular value with the smallest value corresponds to vector $\vec{v}_0$ of $\mathbf{V}$ that is most orthogonal to the correlation space. Including structures with correlations that are similar to $\vec{v}_0$ will expand the region of correlation space in the fit. One method for identifying those structures is to compare $\vec{v}_0$ to a trial database of correlations of known structures. The author acknowledges Chris Fischer for proposing the orthogonalization approach of choosing structures.

Weighting

The previous methods listed in this section describe how to choose structures based on the properties of the correlations of the structure. One technique that changes the fit of ECI is the *weighting* of particular attributes. Increasing weight on an attribute causes its energy to be more or less accurately reproduced by the fit. Weighting is possible on three kinds of attributes: an individual structure's energy, convex hull energies, and the energy difference between a particular structure's energy and

the convex hull energy at its composition. The method to mathematically include weighting into the fit depends on the type of weighting. To weigh an individual structure i, multiply each element m in the row of correlations, σ_m^i, for the structure and the element of the energy vector $\vec{E}_i$ for the structure by a constant factor, w_i .

$$E_i \Rightarrow w_i * E_i \tag{2.17}$$

$$\forall m, \sigma_m^i \Rightarrow w_i * \sigma_m^i \tag{2.18}$$

To weigh the convex hull, an additional row of correlations for the correlation matrix and an energy element for the energy vector are necessary. One correlation row and one energy element are added for each ground state structure (not including the end point structures). Referring to figure 2-3, the energy element for the ground state structure B is

$$E_B = \left(\frac{E_C - E_B}{x_C - x_B} - \frac{E_B - E_A}{x_B - x_A} \right) * w_B \tag{2.19}$$

and the element of the row of correlations for B are

$$\forall m, \sigma_m^B = \left(\frac{\sigma_m^C - \sigma_m^B}{x_C - x_B} - \frac{\sigma_m^B - \sigma_m^A}{x_B - x_A} \right) * w_B \tag{2.20}$$

To weigh the energy difference, E_k, between the energy of a structure D and the energy of the hull, an additional energy element and correlation vector are necessary:

$$E_k = \left\{ E_D - \left[E_B + \left(\frac{E_C - E_B}{x_C - x_B} \right) * (x_D - x_B) \right] \right\} * w_k \tag{2.21}$$

and similarly

$$\forall m, \sigma_m^k = \left\{ \sigma_m^D - \left[\sigma_m^B + \left(\frac{\sigma_m^C - \sigma_m^B}{x_C - x_B} \right) * (x_D - x_B) \right] \right\} * w_k \tag{2.22}$$

The author acknowledges Anton van der Ven for the weighting schemes.

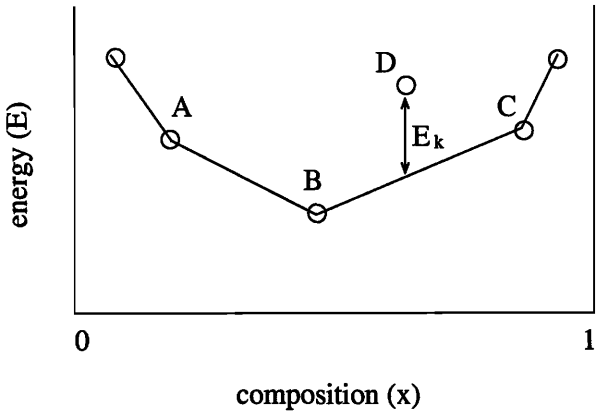

Figure 2-3: Adding elements to the energy vector and correlation matrix will emphasize attributes of the cluster expansion. One attribute, for example, is the energy difference E_k between a structure and the hull.

2.3.3 Mathematical fitting

Several mathematical techniques exist to determine the relationship between the clusters and the energies. Least squares minimization, linear programming, principal components, partial least squares, and Ridge regression are all available techniques. Ridge regression is also known as the weight decay method in neural networks. In cluster expansions, the least squares method and linear programming are the most common methods to determine ECI. Least squares minimization seeks to minimize the root mean squared error of the energies. Linear programming seeks to find a space of available solutions and choose the solution which optimizes an objective function of those variables [44]. The techniques may give similar but distinct results and are both viable options for determining ECI.

Chapter 3

Cluster expansion of ZrO_2-$YO_{1.5}$ using first principles energies

3.1 Expansion on coupled sublattices

The cluster expansion of ZrO_2-$YO_{1.5}$ is different from a traditional binary cluster expansion because configurational disorder exists on two types of sites: the cation fcc sites with Y and Zr and the anion simple cubic sites with oxygen and vacancies. For every two yttrium on the cation sites, one vacancy is necessary on an anion site to maintain charge balance. The cations and anions do not mix between their respective fcc and simple cubic sublattices, but the equilibrium configurations on each sublattice may depend on the other. To model the possible dependence between sublattices, the cluster expansion couples the sublattice configurations by including clusters that contain at least one cation site and one anion site. The model for YSZ only considers structures on a cubic lattices; monoclinic and tetragonal phases of zirconia are not considered.

3.2 Energies from first principles

Configurations of the cluster expansion of YSZ came from a variety of sources. C. Wolverton and A. Bogicevic at the Ford Motor Company chose the first 90 structures

and calculated the total energy of each. Their investigations of YSZ used configurations at 25, 29, 33, 50, and 57 % $YO_{1.5}$ [40, 45, 46]. Using lattice algebra techniques, they determined unique cation configurations on the face-centered cubic sublattice and then decorated the simple cubic anion sublattice[40].

Selection of structures to calculate and add to the initial set for this investigation followed the methods in section 2.3.2. A useful source of structures was a database of all 81827 configurations that are possible in supercells consisting of 9 primitive fcc unit cells or smaller on the fluorite lattice. Each primitive unit cell has 1 cation and 2 anion sites.

The total energy of each structure is obtained with the VASP implementation of Density Functional Theory (DFT) in the Generalized Gradient Approximation (GGA) with the PW91 exchange-correlation functional. The calculations use ultrasoft pseudopotentials. Beginning with configurations of ions in ideal cubic fluorite positions, the calculation allows ion positions and volumes to relax during energy minimization with a 2x2x2 k-point mesh. Starting from the 2x2x2 k-point mesh relaxed configuration, a calculation of the total energy using a 4x4x4 k-point mesh gives the final total energy. Calculations of some structures with a 6x6x6 k-point mesh ensure that the 4x4x4 k-point mesh is adequate for k-point convergence. The fit does not include any structure having ions that relaxed more than half of the distance from its original site to its first nearest neighbor.

The final YSZ cluster expansion contains the energies of 447 structures. Figure 3-1 shows the DFT formation energies of the structures. The ground states of the system are cubic ZrO_2, C-type Y_2O_3, and structures with 25, 29, 33, and 57 % $YO_{1.5}$. The structures with 25, 29, and 33 % $YO_{1.5}$ have not been previously identified on the cubic lattice as stable structures on the convex hull. Descriptions of the ground state structures are in chapter 4.

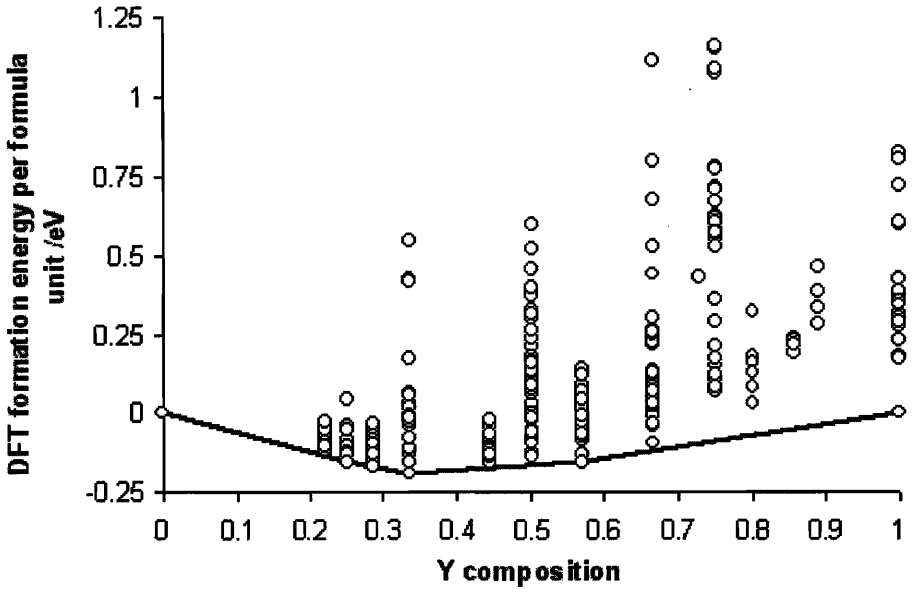

Figure 3-1: The DFT energies of configurations in the cluster expansion are at 15 compositions: 0, 22, 25, 29, 33, 44, 50, 57, 67, 73, 75, 80, 86, 89, 100 % $YO_{1.5}$.

3.3 Cross validation score minimization

3.3.1 Clusters

To select clusters, a Monte Carlo-like approach was used to chose clusters that minimize the cross validation score [47]. Minimizing the cv score theoretically converges the cluster expansion on the optimal fit of the correlations to the energies (see section 2.3.1). To choose clusters for the expansion, the searching algorithm selects a cluster at random from a set of enumerated clusters. If including the correlations of that cluster in the expansion decreases the cv score, the algorithm includes the cluster. If the cluster increases the cv score, the algorithm accepts the cluster when the following condition holds:

$$\exp\left(\frac{\Delta cv}{k_B T}\right) > \text{random number} \tag{3.1}$$

where Δcv is the increase in cross validation score, T is a pseudo-temperature term set to obtain efficient sampling statistics, and the random number is in the range between zero and one. For this expansion, k_BT equals 0.1 meV. The final cluster selection has 111 clusters: an empty term, a point term, 27 pairs, and 82 triplets. The set of triplets contains 51 anion-only clusters, 13 cation-only clusters, and 18 mixed cation-anion clusters. The rms error of the fit is 0.015 eV and the cv score is 0.022 eV. Figures 3-2, 3-3, and 3-4 show the cation, anion, and cation-anion pair clusters.

3.3.2 ECI

The pair ECI from fitting the 447 structures with 111 clusters are in figure 3-5. The anion-anion pair ECI have large values that peak at the fourth nearest neighbor and then roughly decrease with distance. Two third nearest neighbor pairs exist at 4.59 Å apart, given a perfect cubic fluorite lattice with lattice parameter 5.3 Å. The positive third nearest neighbor pair corresponds to a simple cube body diagonal with a cation between the pair sites, and the negative third nearest neighbor pair corresponds to a simple cube body diagonal with no cation between the pair sites.

Large values for the anion-anion terms likely result from the energetics of the repulsion of -2 charges and the physical distortion due to vacancies. In all cases except at third nearest neighbor, the anion-anion interactions show that vacancies repel each other, which is consistent with electrostatic repulsion of effective +2 charges. The negative third nearest neighbor pair term, however, shows that vacancies at body diagonals from each other are attractive when no yttrium or zirconium is between them. If the material energetically favors the cubic fluorite structure, the configuration of body diagonal vacancies may be the ideal arrangement to minimize distortion of the structure.

The cluster expansion also contains cation-anion and cation-cation pair terms. The cation-anion pair ECI show repulsive interactions for zirconium-vacancy (and yttrium-oxygen) pairs in the first and second nearest neighbor. This repulsion is consistent with an electrostatic preference of vacancies to be near the lower +3 valent

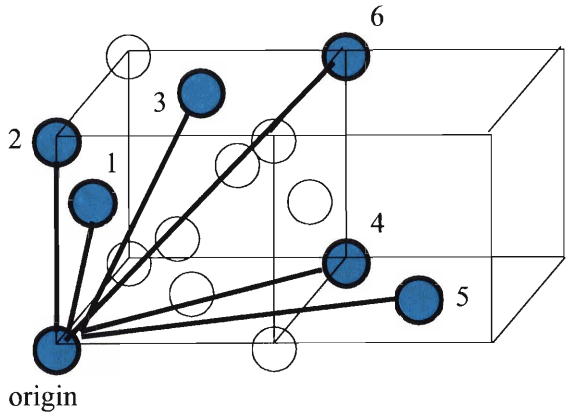

Figure 3-2: The pair clusters of the cation sublattice are on face centered cubic sites. Each pair contains the site at the origin and one of the numbered neighboring sites. The site numbers indicate increasing distance away from the origin. The first through seventh nearest neighbor clusters are in Appendix B labelled #5, 10, 15, 19, 24, 26, 29 (listed by increasing size).

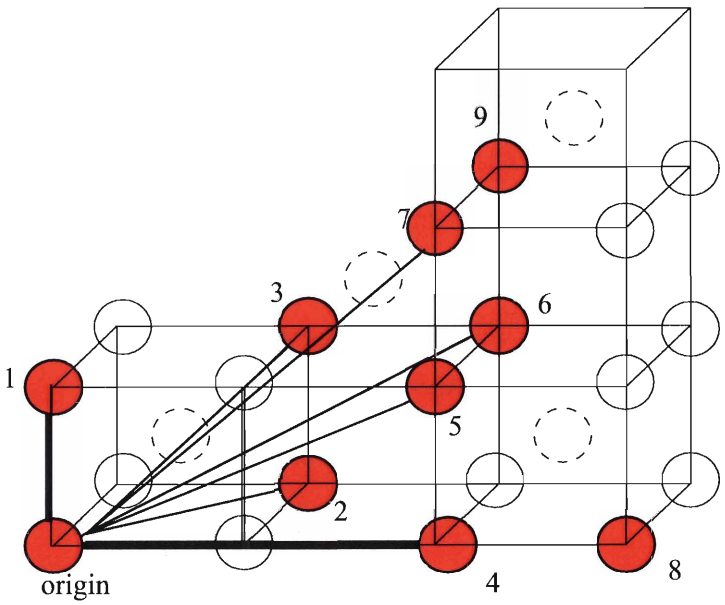

Figure 3-3: The pair clusters of the anion sublattice are on simple cubic lattice sites. The dotted circles are cation sites, and cluster labelling is the same as in figure 3-2. Two distinct 3nn and 9nn pairs exist: the 3nn and 9nn clusters shown here and clusters with the same configurations except no cation between anion sites. Listed by increasing size, the first through ninth nearest neighbors are in Appendix B labelled #4, 6, 8, 9, 11, 13, 14, 18, 21, 22, 23.

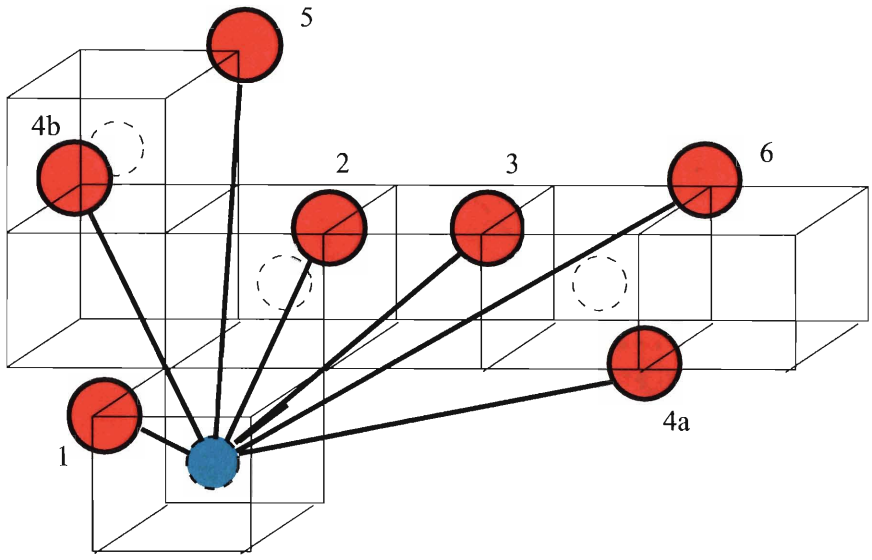

Figure 3-4: Anion sublattice sites are on every simple cube corner. For clarity, only the anion sites in the representative clusters are denoted with solid-line circles. Cation sites (dotted circles) are in the middle of every other anion cube. Listed by increasing size, the first through ninth nearest neighbors are in Appendix B labelled #3, 7, 12, 16, 17, 20, 25, 27, 28, 30.

yttrium rather than the +4 valent zirconium. After the second nearest neighbor, the interactions become slightly attractive and then are negligible with increasing distance. The cation-cation terms are small for all pairs. The large oxygen anions likely screen the smaller cations from each other and hence the cation-cation interactions contribute little to the energy of a structure. The ECI of triplet clusters modify the energetic contribution of the pair ECI. The set of triplets are largely clusters of anions only. In figure 3-6, the four triplets labelled in the figure have relatively large ECI. One triplet (# 41) consists of all anions, and the other three triplets consist of one cation and two anions. Appendix B lists the coordinates and ECI of the triplet clusters.

The coupled cluster expansion of ZrO_2-$GdO_{1.5}$ by P. Tepesch, in comparison to this cluster expansion, showed the anion-anion pair ECI maximized at a large positive value for the first nearest neighbor, and the interactions smoothly decreased with distance[38]. The third nearest neighbor anion ECI were both positive, and the difference between them was less than 0.1 eV. The difference in pair ECI between that

study and this study may be due to the differences in the energies of configurations caused by the size of the dopant ion ($r_{Gd} > r_Y$).

The cluster expanded convex hull contains the same structures as the DFT hull: the experimentally-identified 57 % $YO_{1.5}$ composition (δ-$Y_4Zr_3O_{11}$ [40]) and also ground states at 25, 29, and 33 % $YO_{1.5}$. Chapter 4 describes the structures of the ground states in detail and further investigates the driving forces for order. The ECI of the point, pair, and triplet clusters are in figure 3-6.

3.3.3 Convex hull and monoclinic ZrO_2

The cluster expanded convex hull reproduces the ground state configurations in the DFT hull in figure 3-1. These ground state configuration are at 0, 25, 29, 33, 57 and 100 % $YO_{1.5}$. The experimental ground state of ZrO_2, however, is a distorted-fluorite monoclinic phase, not the cubic fluorite structure in the calculation. Plotting the formation energies with respect to the monoclinic ZrO_2 energy gives a new convex hull (figure 3-7). The convex hull with monoclinic ZrO_2 shows that the ground states with 33 and 57 % Y are both stable intermediate compounds between C-type Y_2O_3 and monoclinic ZrO_2. Experimental studies cite the presence of short range order at compositions in the range 0 - 57 % $YO_{1.5}$ [10], and some experimental and computational phase diagrams suggest a eutectic at 20 % Y_2O_3, which corresponds to 33 % $YO_{1.5}$ [48]. No studies were found in the literature for a stable ordered compound at 33 %.

3.4 Limiting clusters by type of ion

Given the complex nature of interaction among cations, among anions, and between sublattices, more insight in to the driving forces for stability are possible with a separate cluster expansion on each sublattice. Three separate cluster expansions, one with only cation clusters, one with only anion clusters, and one with clusters with at least one cation and one anion, illustrate how each interaction type models the range of compounds. Figure 3-8 shows the pair ECI for the three separate cluster

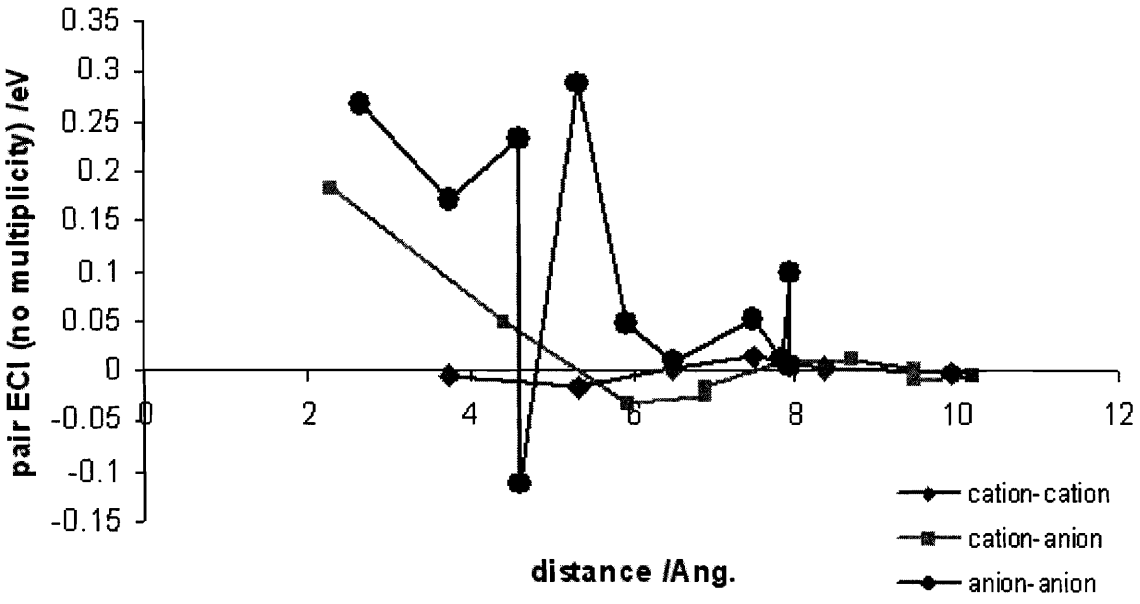

Figure 3-5: The cluster expansion using cv score minimizing clusters had 447 structures with 111 clusters. For each of the pair types (cation-cation, cation-anion, and anion-anion), the plot of the distance between points in a pair versus the ECI for that pair shows the interactions roughly decreases with distance.

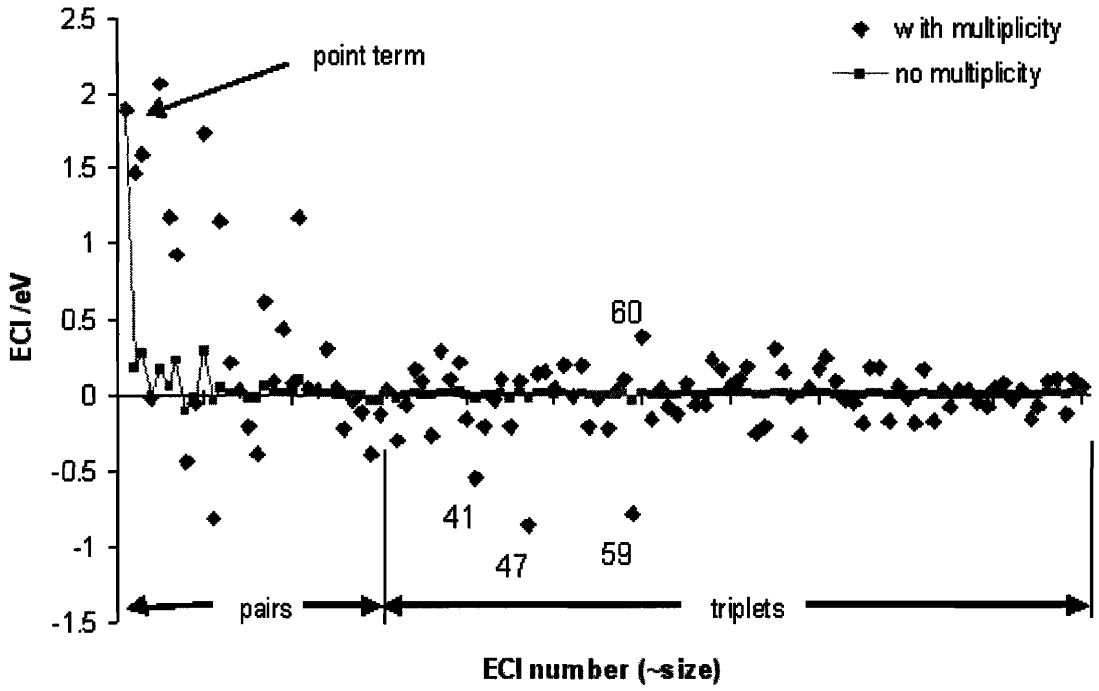

Figure 3-6: The plot of all ECI from the cluster expansion that minimizes the cv score shows large ECI for the pair terms and four distinctively large triplet ECI. The empty term is -4.269 eV. The labels on the four large ECI triplets correspond to the clusters in Appendix B.

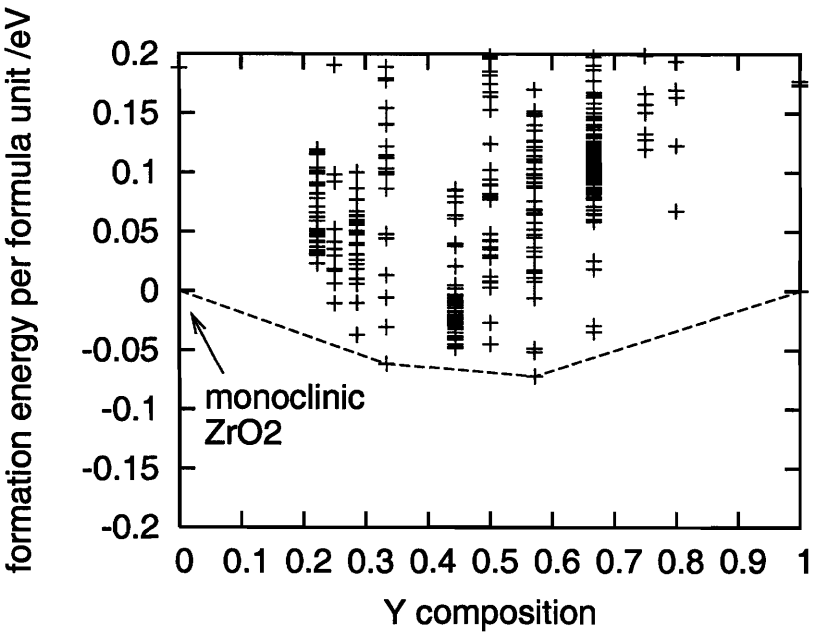

Figure 3-7: The convex hull of DFT energies has monoclinic ZrO_2 and C-type $YO_{1.5}$ as endmembers. Structures at 33 % Y and 57 % Y are the ground states.

expansions. Positive ECI in the cation-anion cluster expansion indicate a repulsive interaction between Y and O. The rms errors for cluster expansions with anion clusters only, cation clusters only, and cation-anion coupling clusters only are 46 meV, 129 meV, and 69 meV, respectively. The cross validation scores for the same expansions are 79 meV, 138 meV, and 103 meV, respectively. The anion cluster fit has the lowest rms error and cv score of the three expansions. Computational studies from other authors also conclude that the anion interactions drive the energetics of ordering in cubic zirconias [49, 50].

3.5 Limiting structures by composition

The configurations at 33, 50, and 57 % Y are an interesting subset of the calculated structures. The 33 % and 57 % Y compositions are on the convex hull of the total cluster expansion. The 50 % Y composition is intermediate between 33 and 57 % Y, and in some zirconias stabilized with dopants larger than Y, the pyrochlore structure stabilizes at this composition. The energies at each composition were each used to fit

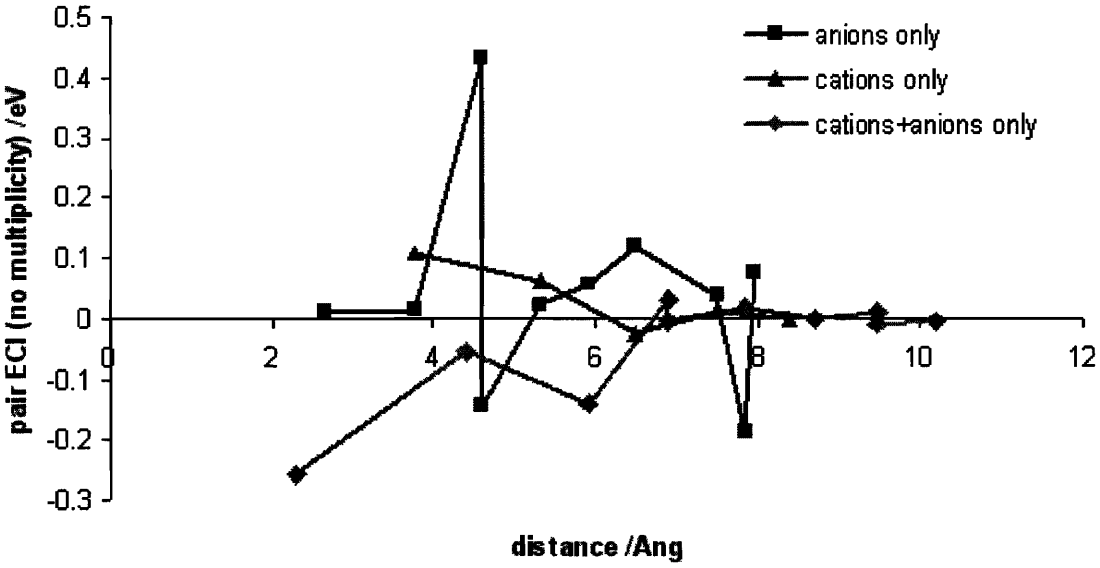

Figure 3-8: Each curve represents the pair ECI from a separate cluster expansion. The curve with red square points represents the expansion containing only anion clusters. The curve with green triangles represents an expansion with only cation clusters. The curve with grey diamonds represents an expansion with clusters that each contain at least one cation and one anion.

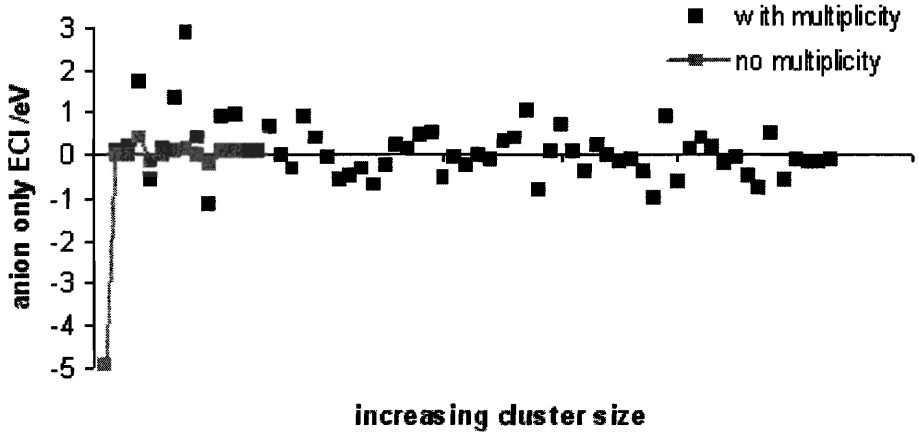

Figure 3-9: The set of ECI from a cluster expansion using clusters with anion sites only contain 11 pairs and 51 triplets. The empty term is 3.907 eV. The point term is the term in the figure at the smallest cluster size. The next 11 data points connected with a line are the pair ECI from figure 3-8. The remaining 51 data points are triplets.

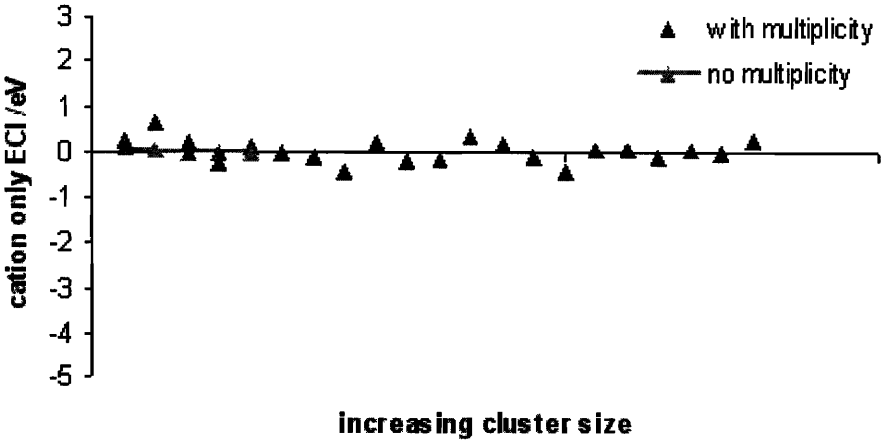

Figure 3-10: The set ECI of a cluster expansion using clusters with cation sites only contain 5 pairs and 15 triplets. The empty term is 0.0980 eV. The ECI from empty and point clusters are labelled as in figure 3-9.

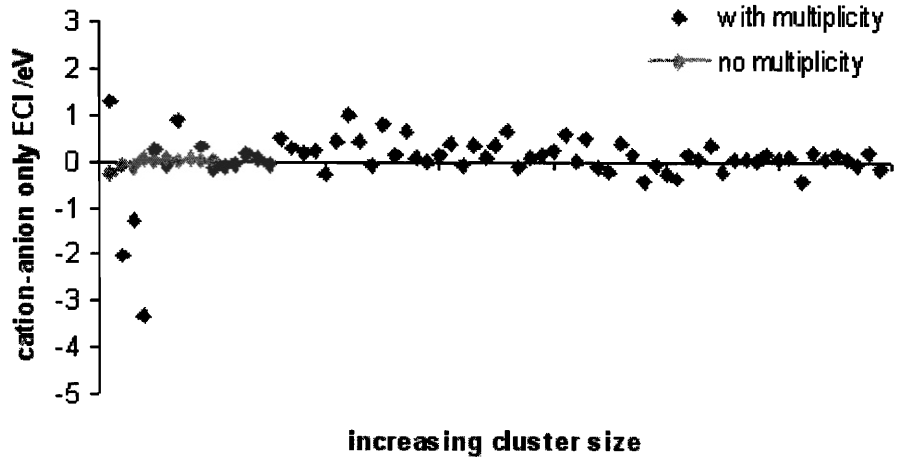

Figure 3-11: The set of ECI for a cluster expansion using clusters with anion sites only contain 10 pairs and 58 triplets. The empty term is 0.0851 eV. The ECI from empty and point clusters are labelled as in figure 3-9.

a separate cluster expansion. Figure 3-12 shows the subset of formation energies for these three compositions. The clusters for each fit are the result of iteratively adding

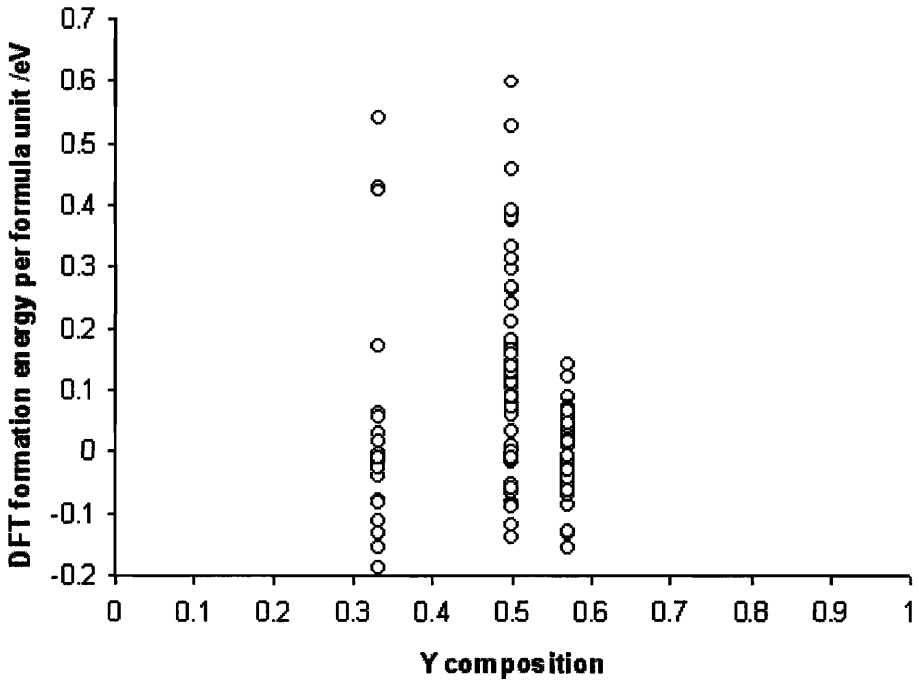

Figure 3-12: The DFT energies for 23 33 % Yconfigurations, 60 50 % Y configurations, and 49 57 % Y configurations.

and subtracting clusters to and from each set to minimize the cv score. The ECI of the three expansions are in figures 3-13, 3-14, and 3-15. Each cluster expansion contains an empty term, a point term, pairs, triplets, and quadruplets. The rms error and cv score for the 33 %, 50 %, and 57 % Y expansions are 0.0082 and 0.0126 eV; 0.0413 and 0.0523 eV; and 0.0093 and 0.0123 eV, respectively.

The cluster expansion of structures with high Y content (the 57 % Y structures) have ECI with a relatively high number of cation-containing clusters. The cluster expansion of structures with low Y content (the 33 % Y structures) have ECI with a relatively low number of cation-containing clusters. The cluster expansion of 50 % Y structures has an intermediate number of cation-containing clusters. The ratio of the total number of cation sites to the total number of anion sites in all the clusters of one

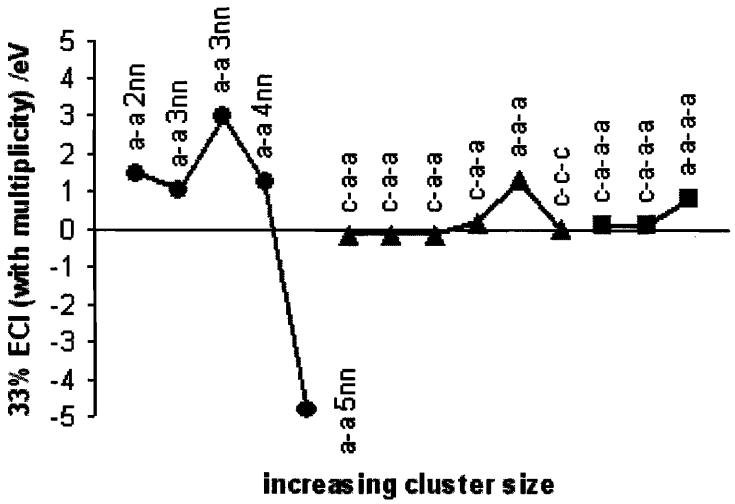

Figure 3-13: The anion pair terms dominate the cluster expansion of the 33 % Y configurations. The empty term is -2.491 eV. Circles denote pair ECI, triangles denote triplet ECI, and squares denote quadruplet ECI. In the labels for triplets and quadruplets, the notation 'c-c-a' indicates a cation-cation-anion triplet, for example.

expansion is a relative indicator of how much the cation sites decrease the cv score of the fits. The ratio is 0.290 (9:31), 0.425 (17:40), and 0.600 (21:35) for the 33 %, 50 %, and 57 % Y expansions, respectively. This suggests that the anion configurations are more important at low Y concentrations and the role of the cations increases in importance as the yttrium content increases. Further discussion on the role of cations to ordering in fluorite oxides is in chapter 4.

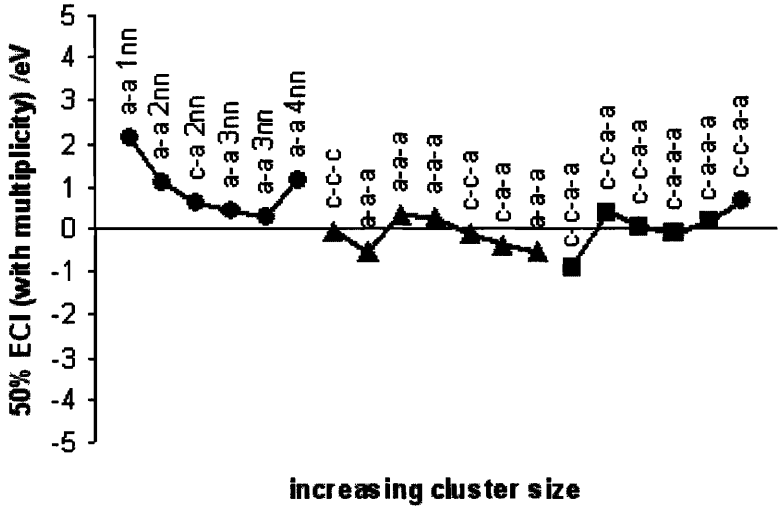

Figure 3-14: The pair terms of the cluster expansion at 50 % Y includes all anion-anion pairs and one cation-anion cluster. The empty term is -2.530 eV.

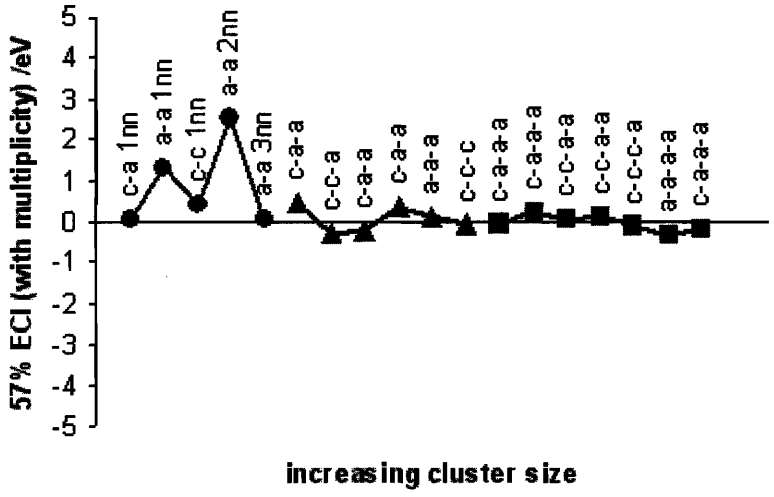

Figure 3-15: The pair terms of the cluster expansion at 57 % Y includes three anion-anion pairs, one cation-anion pair, and one cation-cation pair. The anion-anion 3nn pair does not contain a cation intermediate between the anions. The empty term is -1.844 eV.

Chapter 4

The ground states of YSZ

This chapter discusses ordering in YSZ materials by highlighting the literature on the topic and describing the characteristics of a large set of structures and the ground state structures, in particular, predicted with DFT in chapter 3. The literature suggests many ordering and relaxation trends, but most recent studies agree on the arrangement of yttrium and vacancies at second nearest neighbors. An analysis of almost 300 YSZ structures shows the roles of coordination and relaxation across the composition range. A close look at the ground states shows yttrium ions nearest neighbors to each other in adjacent [1 1 2] chains and vacancies at sixth nearest neighbors to each other on the anion sublattice. Giving further insight in to the system, the density of states gives of the ground state structures suggests hybridization of oxygen p orbitals with Zr d orbitals but not Y d orbitals, and Monte Carlo simulations give preliminary evidence for an important feature in the ordering mechanism with temperature in one of the ground states.

4.1 Literature review of ZrO_2 - $YO_{1.5}$ ordering

In the fluorite structure, cations are in 8 fold coordination by anions, and anions are in 4 fold coordination by cations. In the cubic yttria-stabilized zirconia literature, the arrangement of yttrium and zirconium cations and the oxygen (and vacancy) anions with respect to each other is a topic of discussion. Interpretations of experimental

and computational data suggest both random disorder and short range order on each sublattice. Classical arguments for ordering/disordering of cations and anions reference several driving forces: electrostatic interactions, coordination preference, and elastic strain. The electrostatic interaction of vacancies with cations suggests that positively charged vacancies would associate more closely with lower valent Y^{3+} rather than Zr^{4+}. A coordination driven argument suggests that vacancies in YSZ would associate with Zr rather than Y to decrease the Zr coordination from eight to seven. Zirconium is seven fold coordinated in its ground state ZrO_2 monoclinic phase. Elastic strain could also influence ordering. The differences in sizes of the cations may create strain fields around the larger ions. The presence of a vacancy, in addition, creates a large physical distortion. Frey, et. al. offer a thorough review of studies of structural features of stabilized zirconia [51].

The precise contribution of each of these driving forces to atomic arrangements is unclear. The literature does, however, broadly investigate the structure of YSZ materials. For the purposes of summarizing the literature, experimental and computational results cover four themes: (1) relaxations and displacements of ions from cubic fluorite sites, (2) the vacancy positions relative to zirconium and yttrium ions, (3) microscopic order of ion aggregates, and (4) the affect of cation arrangement on oxygen diffusion.

4.1.1 Relaxations and displacements

Experimental and computational studies of YSZ show that ions are not arranged on perfect cubic fluorite sites. The direction and magnitude of displacement depends on the measurement technique, sample composition, and degree of crystallinity of the material, but some common results do emerge. A thorough summary is available from Frey, et. al. [51]. Neutron diffraction results show that nearest neighbor oxygen atoms relax in $\langle 100 \rangle$ towards vacancies and that cations relax in the $\langle 111 \rangle$ direction either toward or away from vacancies in 22 % and 26 % $YO_{1.5}$ powders and single crystals [52] and in 18, 30, and 39 % powders and single crystals [53, 10]. Studies with synchrotron radiation on a 24 % $YO_{1.5}$ single crystal and EXAFS of a 21 %

$YO_{1.5}$ single crystal support these conclusions [54, 55].

Another fitting of EXAFS data, however, found that half of oxygen relax in ⟨1 1 1⟩ and the other half in ⟨1 0 0⟩ in a 31 % $YO_{1.5}$ powder [56], and an analysis of convergent beam electron diffraction of 18 and 31 % $YO_{1.5}$ single crystals describes both anion and cation displacements in ⟨111⟩ [57]. From electron diffraction data of 18 %, 33 %, and 46 % $YO_{1.5}$ powders, Suzuki, et. al. model the structure of to have a regular anion displacement modulation along ⟨110⟩ present with a series of antiphase boundaries [58, 59, 60]. Welberry, et. al. also model diffuse x-ray scattering and conclude that strain between cation sites gives rise to [1 1 0] and [-1 1 0] distortion in their 39 % $YO_{1.5}$ crystal [61].

Some computational studies provide another perspective on the role of relaxations. An *ab initio* study of a 96 atom supercell (2x2x2 cubic fluorite cells) investigated the effect of vacancies and yttrium in a ZrO_2 matrix. For both a single vacancy and 25% $YO_{1.5}$ models, an oxygen next to a vacancy relaxed in ⟨100⟩ and cations next to a vacancy relax in ⟨1 1 1⟩ [62]. The cation relaxed in ⟨1 1 0⟩ if it was near two vacancies.

From the number and variety of studies summarized, relaxation and atom displacements clearly do not follow simple predictable behavior. Two computational studies do indicate that the effect of the relaxation is important. While not explicitly defining the direction of relaxation, Bogicevic, et. al.'s studies of a range of compositions involved decoupling the electronic and elastic/displacement components of energy [46, 40, 45]. They found that the elastic component of the energy had a larger contribution to the total energy than the electronic component and thus determined which ionic configurations had lowest energy. Stapper also compared energies of a variety of configurations and found that electrostatic energies of different configurations did not explicitly correlate to the DFT total energies [62].

4.1.2 Vacancy position relative to Y and Zr

The direction and magnitude of displacement of ions from their idealized cubic sites may depend on the larger arrangement of cations and vacancies with respect to each other. A number of studies on this topic come to a variety of conclusions.

Several older studies found vacancies at first nearest neighbors to yttrium. Neutron diffraction of single crystal and powder samples with 18-26 % $YO_{1.5}$ [52] and x-ray diffraction of 21% single crystals [54, 63] found evidence for vacancy-yttrium association. Tuilier's EXAFS study on samples across the ZrO_2-$YO_{1.5}$ composition range also concluded that vacancies are at first nearest neighbor to yttrium. The authors do cite the possibility that as the composition of samples increases, yttrium ions have greater oxygen coordination. They found that the anion framework around yttrium changes more than the framework around zirconium as the dopant composition increased [64]. One XPS study found that binding energies of cation electrons did not change among different yttrium compositions suggesting, in contrast, that oxygen coordination is independent of composition [65].

More recent studies of YSZ compounds found that vacancies reside at nearest neighbors to zirconium. Goff's single crystal neutron diffraction study found vacancy pairs at $\langle 111 \rangle$ to each other with a cation between them [10]. They used a bond distance argument to support that the central cation is zirconium. Catlow's EXAFS studies and potential modelling of 31 % $YO_{1.5}$ powders concluded that vacancies reside at first nearest neighbors to zirconium [56, 66]. In an extensive x-ray study of stabilized zirconias, Li, Chen, and Penner-Hahn cite that EXAFS may only be 20 % accurate in determining ion coordinations [67]. They refine their EXAFS study and include x-ray diffraction and XANES studies to conclude that vacancies reside next to the smaller of the zirconium or dopant cation [68, 67, 69, 70, 71, 72]. In the case of doping with Fe and Ga, the vacancies are next to the dopant ion; in the case of doping with Y or Gd, the vacancy is next to the zirconium [70].

The conclusion that vacancies reside next to zirconium also has support from several computational works. Stapper's DFT LDA study of 25% $YO_{1.5}$ found the total energy of supercell configurations decreased by increasing the number of vacancies at second nearest neighbors to yttrium [62]. Ostanin's LMTO computational study supported this finding showing that the lowest energy supercell structures had vacancies at second nearest neighbors to yttrium [73]. Zacate, et. al. calculated binding energies of oxygen in supercells of ZrO_2 using shell models and Buckingham poten-

tials [74]. They found the binding energies varied by the relative size and placement of a metal dopant in the supercell. They suggest that the reason oversized dopants are energetically favorable at second nearest neighbors to vacancies is to allow ions in the supercell to fully relax. When oversized dopants are nearest neighbors to the vacancy, relaxation does not occur.

4.1.3 Microscopic order

Relaxations and relative arrangement of cations and anions reflect ordering on the individual atomic scale. Multiple studies lead to the conclusion that stabilized zirconia is cubic on average across a long range scale, but at the local atomic scale, the fluorite unit cells are distorted [62, 75, 49, 67]. The individual arrangements may give rise to a larger microscopic order. Goff describes short range ordering with three types of defects: isolated vacancies, vacancy pairs in ⟨111⟩ with a cation between them, and aggregates of vacancy pairs in ⟨112⟩ [10]. The ⟨112⟩ ordering is at least 15 Angstroms in size, and more aggregates form and in greater size as the yttria composition increases.

Morinaga suggests that locally ordered regions containing yttrium aligned in ⟨-3 -3 2⟩ exist but without precipitate formation [63]. A selected area diffraction study of the 50% structure shows weak satellite reflections suggesting both ordering similar to C-type Y_2O_3 and to a distorted pyrochlore [76]. This is in contrast to electron diffraction studies of 39 and 48 % $YO_{1.5}$ single crystals by Gallardo-Lopez, et. al. [77, 78]. The diffuse intensity in the patterns of these crystals resembled the δ structure and did not contain pyrochlore and C-type Y_2O_3-like patterns.

4.1.4 Computational diffusion studies

The conductivity of oxygen in yttria stabilized zirconia increases from zero in pure ZrO_2 to a maximimum with 15 - 18 % $YO_{1.5}$ doping. The conductivity then decreases at higher compositions. If the addition of yttria to zirconia creates more vacancies, one would expect the conductivity to increase linearly with composition due to the

availability of more oxygen diffusion sites. One possible explanation for the maximum and subsequent decrease in conductivity with composition involves the oxygen diffusion pathway. An oxygen diffusing in [1 0 0] to a nearest neighbor anion site moves between two cations. The cations form the endpoints of an edge of a cation tetrahedron surrounding the oxygen, and the size of the cations on the endpoints may influence the migration energy through the edge. Large Y-Y cations on the end points could inhibit oxygen diffusion. As the number of vacancies increases with Y doping, the conductivity increases until the the number of large Y-Y edges inhibit oxygen diffusion.

Another explanation for the peak in conductivity involves the ions having thermodynamic driving forces to order. At dopant concentrations higher than 18 % Y, oxygen and vacancies may order on the anion sublattice. Ordering of vacancies would prohibit oxygen diffusing in to vacant sites without high thermal energy.

Molecular dynamics (MD) and Monte Carlo (MC) simulations attempt to model the diffusion of oxygen in YSZ at various compositions and temperatures to explain the peak in oxygen conductivity. Beginning with a random cation arrangement, Khan's MD study using potential energy models and a simulation cell with 18 % $YO_{1.5}$ gave diffuse oxygen-oxygen maxima in the radial distribution function [7]. The diffuse maxima indicate that oxygen are not highly ordered at long range. No cation diffusion occurred in the simulation.

Another MD simulation by Shimojo using potential energy models shows that a YSZ cell with 18 % Y doping had higher oxygen diffusion than cells with 9 and 37 % Y doping [79]. A record of the oxygen diffusion paths in the 18 % Y doped cell shows that oxygen ions diffuse primarily through Zr-Zr edges. Either the starting or ending site of the oxygen, however, has one or two Y ions in the cation coordination tetrahedron that are not on the sites of the diffusing edge. The presence of Y in the neighborhood of the diffusing oxygen promotes migration. Molecular dynamics studies do not show any cation diffusion.

Krishnamurthy's kinetic Monte Carlo study of oxygen diffusion uses migration barriers calculated with DFT [8]. The random yttrium starting configurations in the

YSZ cells are constant, and the oxygen diffusivity peaks at 18 % Y. The activation energy of diffusion increases linearly with Y composition despite the nonlinear change in conductivity with composition. A simple analytic model of diffusion using the DFT migration barriers closely models the Monte Carlo results only when the model includes correlation between oxygen hops up to fifth nearest neighbor.

Many studies of oxygen diffusivity in YSZ only consider the movement of oxygen, but Fevre's Monte Carlo study considers both the diffusion of cations and anions [81]. In a Monte Carlo simulation of a supercell with 43 % $YO_{1.5}$, the vacancies show $\langle 1\ 1\ 1 \rangle$ ordering up to the seventh nearest neighbor on the anion lattice. Yttrium-yttrium configurations show positive deviations from random in the radial distribution functions at a distance up to 1.5 times the lattice parameter. An early analysis of experimental YSZ conductivity led Hohnke to add a free energy functional to a simple theortical model of oxygen conductivity to bring agreement between experimental and theoretical results [82]. He postulated that long range defect interactions may be the correct physical interpretation of the free energy functional that accounts for the limit in oxygen conductivity at high Y doping.

4.2 Coordination and relaxation

The literature comes to a variety of conclusions about atomic arrangements in YSZ. The work in this section investigates how cation coordination and relaxation around oxygen ions impact the stabilization in YSZ materials. The analysis uses a subset of the structures in chapter 3 that contains 269 structures and considers the variation of cation relaxation with formation energy and cluster occupation probability with formation energy. The structures are from six compositions: 22, 33, 44, 50, 67, and 75 % $YO_{1.5}$, and the energies of those structures are given in figure 4-1.

4.2.1 Cation coordination around oxygen

For a given cluster of atomic sites, the probability of a particular occupation depends on a structure's configuration. Take, for example, three corners of the fcc cube as a

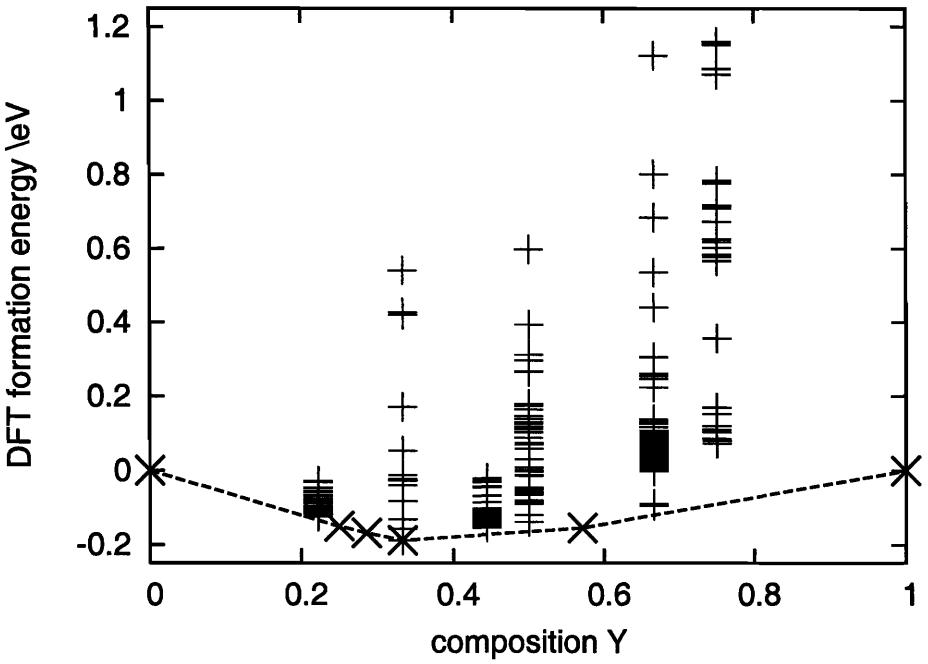

Figure 4-1: The structures used in the coordination and relaxation analysis in section 4.2 are at compositions 22, 33, 44, 50, 67, and 75 % $YO_{1.5}$. The line denotes the DFT convex hull. A plus mark is the energy of one unique structure, and X marks denote the energies of the ground states for reference.

cluster. The probability that the triplet will be occupied by all yttrium will depend on the configuration of atoms in the structure. The probability deviation from random is the difference between the probability of that occupation in the ordered structure and the probability of that occupation occuring in a randomly averaged structure at the same composition. The probability deviation from random of an occupation β on a cluster is given by

$$\rho_\beta = \frac{1}{2^{n_\beta}} \sum_{\alpha \subset \beta} \phi_\alpha \sigma_\alpha - \rho_{\beta-random} \tag{4.1}$$

where α denotes all subclusters of β, including the empty and point terms and β itself. ϕ is the correlation function of the α subcluster in the structure, and σ is the product of the occupation variables for the points in the subcluster. n_β are the number of points in the cluster β [88]. $\rho_{\beta-random}$ is the probability of occupation β occuring in a randomly ordered structure of the same composition and is equal to the product of the concentration of the species (Zr, Y, O, or $\square$) for each point in β in a material at the appropriate composition.

For this analysis, the cluster of interest is a cation tetrahedron with an oxygen at the center, and the different occupations on the tetrahedron are three yttrium with one zirconium (3Y-Zr), two yttrium with two zirconium (2Y-2Zr), and one yttrium with three zirconium (Y-3Zr). Now consider how the occupation probability varies across structures. The probability deviation from random of the cation tetrahedron around an oxygen containing two Y and two Zr, for example, may be different for two structures with the same Y composition but different ionic configurations. Figure 4-2 shows the probability deviation from random of the 2Y-2Zr occupation around oxygen for all the structures with 75 % $YO_{1.5}$ composition. The probabilities are plotted as a function of the formation energy of each structure. The range of the probabilities is from -0.1 to 0.5.

The slope of the plot in figure 4-2 provides some useful information. The plot shows that the higher energy structures have a higher probability of having the 2Y-2Zr occupation around oxygen. High energy structures are relatively less stable than the low energy structures, therefore, less stable structures have a higher probability of the

2Y-2Zr occupation. A positive slope of the probability deviation from random versus formation energy plot indicates the occupation is associated with a destabilizing force in the structures at that composition. A negative slope indicates the occupation is associated with a stabilizing force in the structures at that composition. The plots of all three occupations of interest at six compositions are in appendix C.

For the six compositions of interest, figure 4-3 plots the slopes of three different occupations of the oxygen-cation tetrahedron cluster (3Y-Zr, 2Y-2Zr, Y-3Zr). The plot shows that (1) the 3Y-Zr occupation becomes more stabilizing and the Y-3Zr and 2Y-2Zr occupations less stabilizing as yttrium concentration increases and (2) except at 33 % $YO_{1.5}$, the slopes of Y-3Zr and 2Y-2Zr occupations have the opposite effect from each other on the stability of a particular composition.

In the first result, the probability deviation from random shows that the 3Y-Zr occupation around an oxygen is present in more stable structures at higher Y composition. At each composition, either 3Y-Zr or 2Y-2Zr is the most stabilizing occupation, except at 33 % Y where 2Y-2Zr and Y-3Zr are nearly equal. The stabilizing nature of Y occupying sites next to oxygen may be a consequence of yttrium and vacancies prefering to be second nearest neighbors to each other. As the vacancy concentration increases, the yttrium occupy more sites next to oxygen.

The second result is a more surprising outcome. The Y-3Zr occupation has the opposite trend with yttrium composition to the 3Y-Zr occupation; the 2Y-2Zr occupation, however, does not remain constant across compositions. It oscillates with the Y-3Zr occupation stability. The figure shows, except at 33 % Y, that when the 2Y-2Zr cluster is stabilizing, the Y-3Zr occupation is either destabilizing or has no effect. The reverse is true when Y-3Zr is stabilizing. One possible reason for this is that a constraint imposed by the number of primitive cells at each composition may force particular occupations to form to maximize vacancy separation in the structures. Another possible reason is that either the Y-3Zr or the 2Y-2Zr occupation allows oxygen to relax in the structure more readily depending on the geometry of the unit cells.

A comment is necessary on the data points for the 22 % Y structures since those

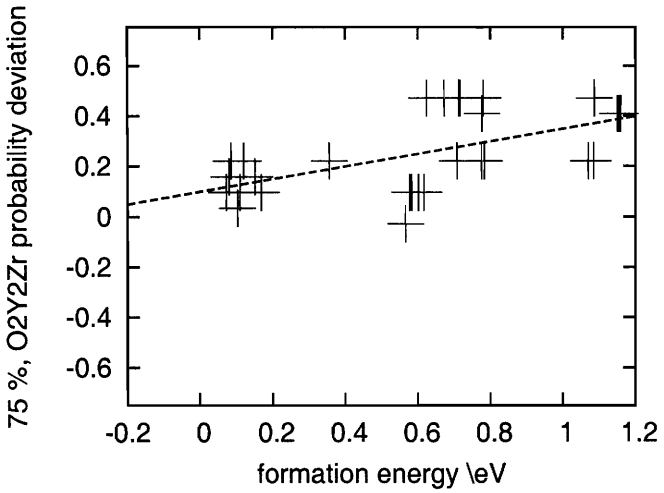

Figure 4-2: Each point represents one 75 % $YO_{1.5}$ structure. The O-2Y-2Zr cluster is less likely to occur in the low energy structures.

magnitudes are relatively large. The range of energies of 22 % Y structures is small (0.1 eV) compared to the ranges of energies for most of the other structures. The slopes associated with relaxation and oxygen coordination are twice as large as for the other compounds. Structures with potentially higher energy were excluded from the analysis because they had ions with very large (1 Å) displacements after relaxation and could no longer be considered the same structure. The configurations that maintained their structures did have large relaxations (section 4.2.2 has further discussion).

4.2.2 Relaxation of cations around oxygen

Similar to the analysis involving the probability of a particular cation coordination is an analysis of the relaxation of cations around oxygen. The average absolute value of displacement of the cations from the unrelaxed cubic fluorite positions to their fully relaxed positions gives the relaxation of the coordination around each oxygen in the unit cell. The average of the relaxations for all oxygen in the unit cell gives the

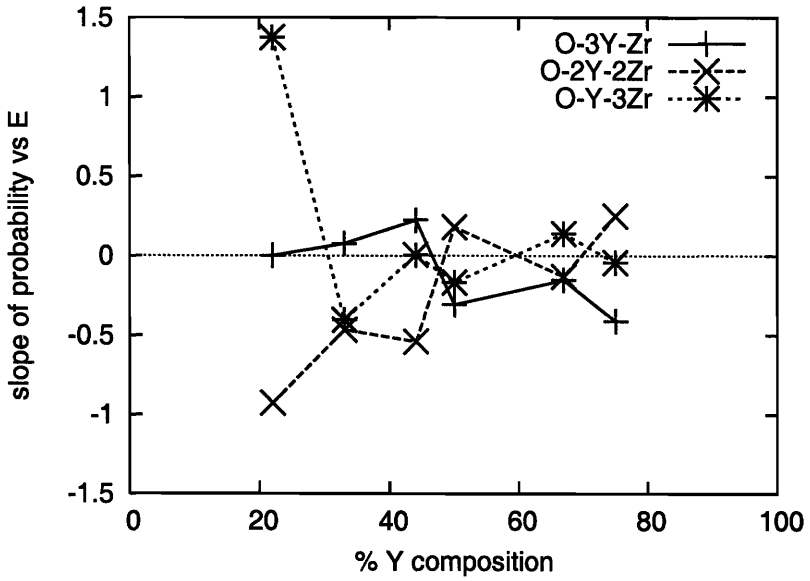

Figure 4-3: The three curves indicate the slope of the probability deviation from random for a particular cluster occupation versus formation energy. The clusters are the three occupation types of a cation tetrahedron around an oxygen. Plus marks on a solid line indicate the tetrahedron with three ytrrium and one zirconium, X marks on a dashed line indicate the tetrahedron with two yttrium and two zirconium, and an asterisk on a dotted line indicates a tetrahedron with one yttrium and three zirconium.

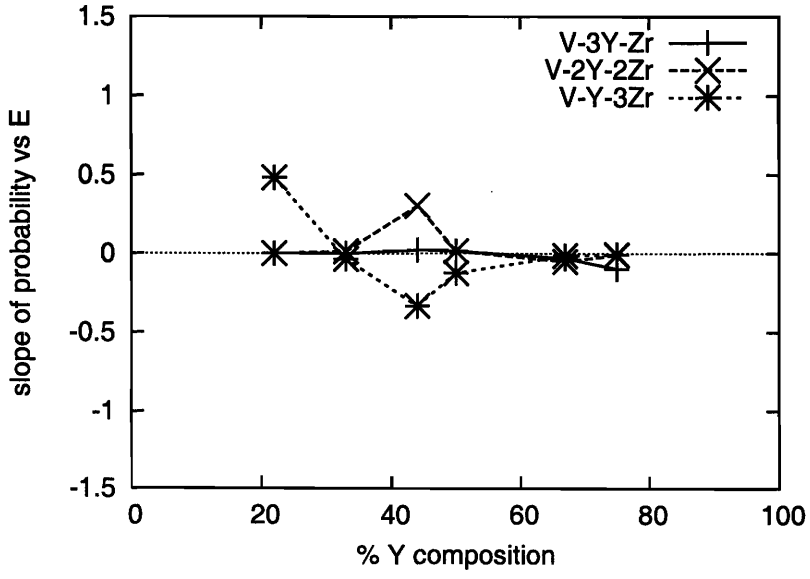

Figure 4-4: An analogous plot to figure 4-3 for the occupation of the cation tetrahedron around a vacancy.

relaxation for a structure:

$$\text{average relaxation} = \frac{1}{N_{oxygen}} \sum_{j=1}^{N_{oxygen}} \left(\frac{1}{4} \sum_{i=1}^{4} |R^j_{i,idealcubic} - R^j_{i,relaxed}| \right) \tag{4.2}$$

where R is the distance from a cation in the tetrahedron to the center oxygen. Figure 4-5 gives an example for the structures at 50 % $YO_{1.5}$. Plotting the slopes of relaxation versus energy at all compositions gives the plot in figure 4-6. Just as in section 4.2.1, a negative slope indicates that more relaxation is present in more stable structures, and a positive slope indicates that the more relaxation is present in less stable structures.

The main conclusion from figure 4-6 is that the effect of relaxation, whether it is stabilizing or destabilizing, decreases with increasing yttrium composition. One possible explanation is that at high yttria concentration, the vacancies cause such a large distortion in the cubic lattice that the relaxations are largely the same across structures of the same composition; hence, the stabilization of structures comes from maximizing electrostatic separation of the vacancies and yttrium or satisfying some other electronic driving force. At low yttria concentration, disruptions to the simple cubic oxygen framework due to only a few vacancies may have a large effect on the energies. In 22 % $YO_{1.5}$ structures, the relatively large stabilizing effect of relaxations may be related to the observation of maximum ionic conductivity occuring at 18 % $YO_{1.5}$. A large degree of instability would be expected in compositions near 18 % because small binding energies and tendency towards allowing disorder would be conducive for ionic conductivity. In the 33 % Y structures, the opposite relaxation effect is present. More relaxation occurs in higher energy structures. At this composition, the lowest energy structure is a ground state structure. The ground state is the optimum structure such that any further deviation from this structure would be unstable.

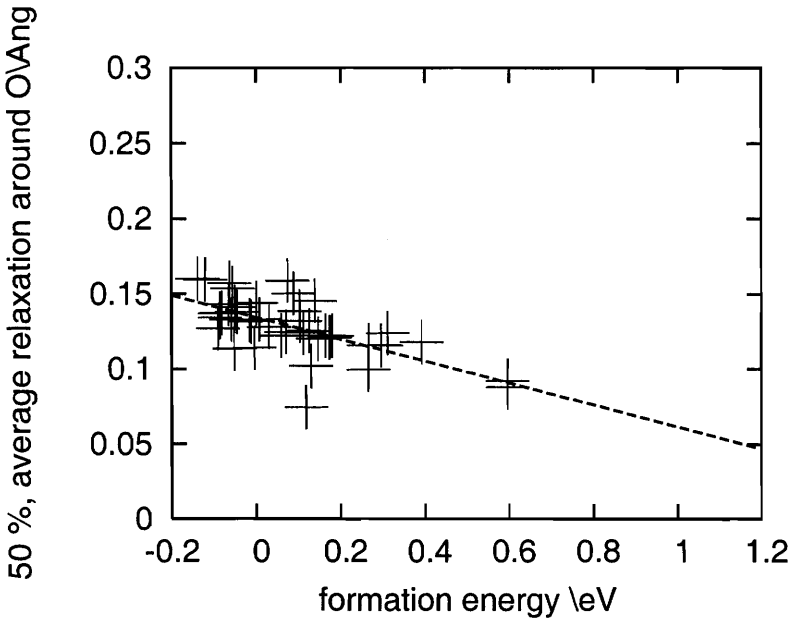

Figure 4-5: Each point represents one 50 % $YO_{1.5}$ structure. The average relaxation around the oxygen in a structure decreases toward higher energy structures.

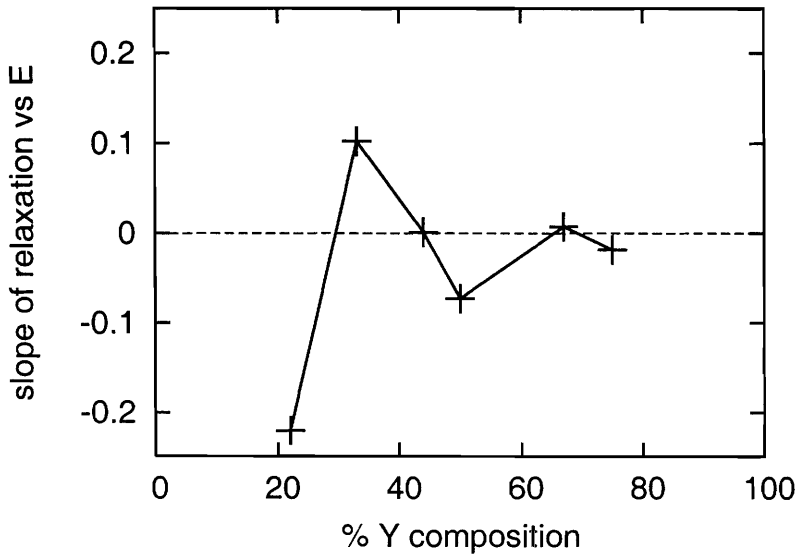

Figure 4-6: Each point represents the slope of the average cation relaxation around oxygen versus formation energy at the six compositions.

4.3 Ground state crystal structures

Section 4.2 looked at the ordering affects on the scale of individual atom coordinations. The analysis of the cation occupations showed that oxygen coordinated by one or two yttrium is largely dominant at low yttrium compositions while oxygen coordinated by three yttrium is dominant at high yttrium concentration. Another analysis showed that the effect of relaxation decreases with increasing yttrium content. This section looks at the system by considering the arrangments of all the ions in the ground state crystal structures obtained in chapter 3. A description of each of the four ground states draws out common ordered features.

4.3.1 Ground state descriptions

Tables 4.1 and 4.2 give the primitive cells of the intermediate composition ground states. The structures have several configurational elements in common, and the descriptions of the structures are given with respect to cubic settings, except where noted. In each of the ground states at 25, 29, 33, and 57 % Y, the yttrium and vacancies are aligned in chains in the [1 1 2] direction within (1 1 1) planes, and the yttrium are in double chains (two chains at first nearest neighbors). Figure 4-7 shows these orientations. Another description of the ground state with 57 % Y is discussed below. The light grey lines outline the $\vec{b}$ and $\vec{c}$ lattice vectors of the primitive cell.

The ground state structure with 25 % $YO_{1.5}$ has the formula $Y_2Zr_6O_{15}$. Figure 4-8 shows two pictures of the structure. In figure 4-8(a), the cation (1 1 1) planes alternate between pure zirconium planes and planes with half yttrium and half zirconium. The mixed cation planes show double rows of yttrium next to double rows of zirconium in the [1 1 2] direction. Each yttrium has eight oxygen in nearest neighbor sites.

Each vacancy's closest four vacancy neighbors are at sixth nearest neighbors on the anion cubic sublattice (see figure 3-3). Two of the neighbors and the central vacancy form part of a vacancy chain in the [1 1 2] direction. In figure 4-8(a), a single small orange sphere shows the perpendicular view along the axis of one [1 1 2] chain. The two other vacancy neighbors in the structure are in parallel vacancy

$\vec{a} = 6.398$ Å	$\alpha = 88.1°$
$\vec{b} = 15.217$ Å	$\beta = 66.4°$
$\vec{c} = 16.029$ Å	$\gamma = 24.5°$

0.607	0.005	0.879	Y
0.268	0.040	0.136	Y
0.168	0.938	0.972	Zr
0.589	0.956	0.496	Zr
0.166	0.999	0.374	Zr
0.168	0.026	0.766	Zr
0.787	0.986	0.234	Zr
0.836	0.008	0.633	Zr
0.665	0.935	0.350	O
0.827	0.670	0.742	O
0.353	0.678	0.636	O
0.492	0.828	0.197	O
0.430	0.714	0.017	O
0.110	0.663	0.515	O
0.294	0.816	0.407	O
0.992	0.738	0.901	O
0.381	0.208	0.822	O
0.633	0.314	0.361	O
0.348	0.263	0.213	O
0.928	0.242	0.720	O
0.752	0.157	0.574	O
0.989	0.288	0.101	O
0.560	0.277	0.985	O

(a)

$\vec{a} = 6.513$ Å	$\alpha = 99.9°$
$\vec{b} = 6.341$ Å	$\beta = 101°$
$\vec{c} = 6.419$ Å	$\gamma = 99.1°$

0.998	0.983	0.011	Y
0.428	0.709	0.835	Y
0.855	0.432	0.750	Zr
0.242	0.141	0.580	Zr
0.710	0.899	0.427	Zr
0.185	0.570	0.285	Zr
0.554	0.263	0.119	Zr
0.760	0.722	0.699	O
0.132	0.471	0.578	O
0.676	0.232	0.441	O
0.009	0.852	0.352	O
0.504	0.589	0.215	O
0.878	0.361	0.078	O
0.311	0.038	0.885	O
0.260	0.237	0.268	O
0.669	0.954	0.098	O
0.127	0.661	0.980	O
0.522	0.367	0.794	O
0.957	0.121	0.698	O
0.402	0.862	0.513	O

(b)

Table 4.1: Table (a) contains the fully relaxed unit cell and atom positions of the 25 % ground state structure. Table (b) contains the fully relaxed unit cell and atom positions of the 29 % ground state structure.

$\vec{a} = 6.422$ Å	$\alpha = 116°$
$\vec{b} = 6.422$ Å	$\beta = 116°$
$\vec{c} = 12.36$ Å	$\gamma = 120°$

0.813	0.153	0.493	Y
0.487	0.480	0.493	Y
0.954	0.994	0.995	Zr
0.681	0.348	0.991	Zr
0.327	0.620	0.995	Zr
0.216	0.883	0.526	Zr
0.493	0.868	0.921	O
0.201	0.160	0.921	O
0.854	0.520	0.892	O
0.202	0.869	0.347	O
0.889	0.274	0.333	O
0.608	0.556	0.333	O
0.383	0.403	0.640	O
0.084	0.751	0.640	O
0.736	0.049	0.640	O
0.179	0.518	0.108	O
0.851	0.845	0.108	O

(a)

$\vec{a} = 6.458$ Å	$\alpha = 98.4°$
$\vec{b} = 6.652$ Å	$\beta = 99.6°$
$\vec{c} = 6.415$ Å	$\gamma = 99.8°$

0.437	0.676	0.840	Y
0.872	0.420	0.757	Y
0.271	0.152	0.529	Y
0.706	0.896	0.446	Y
0.969	0.955	0.991	Zr
0.174	0.616	0.295	Zr
0.571	0.286	0.143	Zr
0.761	0.721	0.731	O
0.154	0.465	0.558	O
0.637	0.227	0.457	O
0.002	0.861	0.314	O
0.484	0.590	0.221	O
0.893	0.403	0.121	O
0.250	0.168	0.165	O
0.659	0.981	0.064	O
0.140	0.711	0.972	O
0.506	0.345	0.828	O
0.988	0.106	0.728	O
0.382	0.851	0.555	O

(b)

Table 4.2: Table (a) contains the fully relaxed unit cell and atom positions of the 33 % ground state structure. Table (b) contains the fully relaxed unit cell and atom positions of the 57 % δ-ground state structure.

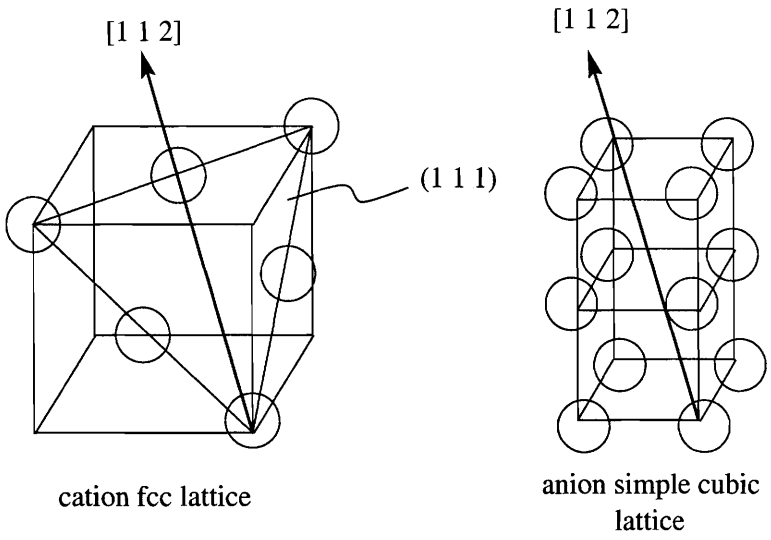

Figure 4-7: Yttrium and vacancies align in the [1 1 2] directions in (1 1 1) planes in the ground states. The figure on the left shows the cations on an fcc lattice, and the figure on the right shows the [1 1 2] direction on a simple cubic lattice.

chains on either side of the original vacancy chain, and these three vacancy chains are in one plane. In the same figure, two of the three vacancy chains are visible within one horizontal anion plane. The next nearest vacancies to the original vacancy are 7.5 Å away in another horizontal anion plane. Each vacancy has four zirconium ions around it.

The ground state structure at 29 % $YO_{1.5}$ has the formula $Y_2Zr_5O_{13}$. Vacancies reside in [1 1 2] chains such that vacancies are at sixth nearest neighbor to each other in the chain. A given vacancy has four vacancies at sixth nearest neighbors on the anion sublattice in the adjacent vacancy chains, as shown in figure 4-9(a). The coordination of each vacancy is four zirconium, and the coordination of each yttrium is eight oxygen. Each cation (1 1 1) plane shows five zirconium rows in [1 1 2] alternating with two yttrium rows.

The ground state structure at 33 % $YO_{1.5}$ has the formula $Y_2Zr_4O_{11}$ and has space group C2/m. This ground state is stable with respect to monoclinic ZrO_2. Figure 4-10(a) shows the primitive cell of the structure. The view in to the page is in [1 1 2] with horizontal (1 1 1) planes. The vacancies in this structure are equally spaced in three dimensions such that each vacancy has eight vacancies at sixth nearest neighbors

to each other on the anion sublattice. The nearest vacancies to a given vacancy are in the ⟨1 1 2⟩ direction. Four zirconium coordinate each vacancy at first nearest neighbors.

The cation (1 1 1) planes alternate between a pure zirconium plane and a plane with two-thirds yttrium and one-third zirconium. The mixed cation planes have a honeycomb pattern such that a zirconium atom has six Y atoms at nearest neighbors in the plane. When viewed in the [1 1 2] direction, each cation planes appears to be repeated units of two yttrium rows with one zirconium row. Each yttrium is first nearest neighbors on the cation sublattice to two other yttrium in the nearest chain. The coordination of each yttrium is eight oxygen.

The ground state structure at 57 % $YO_{1.5}$ has the formula $Y_4Zr_3O_{12}$ and is called the δ-structure. The earliest description of the δ structure for YSZ is from Scott [14], and Bogicevic and Wolverton previously reported the atomic coordinates of the δ structure [40]. The structure in table 4.2(b) is an alternate setting.

Vacancies form [1 1 1] chains in the structure with a zirconium between every other vacancy pair. This corresponds to vacancies being in chains along cube diagonals of the simple cubic anion framework. The nearest neighbor vacancies in a chain closest to a given vacancy are in the [0 1 2] and [1 1 2] direction. Vacancies are therefore third nearest neighbors within the chain and fifth and sixth nearest neighbors to the vacancies in the closest chain. Each vacancy has two yttrium and two zirconium ions at nearest neighbors. The view in the primitive cell in figure 4-11(a) shows horizontal (1 1 1) planes viewed along the [1 1 2] direction. Each plane shows four yttrium rows and three zirconium rows. Each yttrium has seven oxygen and one vacancy as nearest neighbors.

4.3.2 Ordering features

The unrelaxed cubic cells of the ground state structures at 25, 29, and 33 % $YO_{1.5}$ all have yttrium in 8-fold coordination by oxygen and vacancies in 4-fold coordination by zirconium. The ground state structure at 57 % $YO_{1.5}$ has yttrium coordinated by seven oxygen and one vacancy, and the vacancy has two zirconium and two yttrium

ground state (% $YO_{1.5}$)	Zr-O (Å)	Y-O (Å)
0 % (monoclinic)	2.19, 2.19, 2.19, 2.19	–
0 % (cubic)	2.24	–
25 %	2.18, 2.18, 2.19, 2.22, 2.30, 2.32	2.41, 2.42
29 %	2.19, 2.19, 2.19, 2.22, 2.33	2.39, 2.40
33 %	2.18, 2.19, 2.19, 2.21	2.43, 2.43
57 %	2.14, 2.29, 2.29	2.36, 2.36, 2.37, 2.37
100 %	–	2.32 (all 16 ions)

Table 4.3: The table lists the average relaxed metal-oxygen bond lengths for each Zr and Y in a ground state structure.

at nearest neighbors. The description of microscopic ordering found by Goff agrees with the ordering found in the δ structure (section 4.1.3) [10].

In the relaxed ground state structures, the bond distances vary from the exact cubic lattice values. The unrelaxed nearest neighbor bond length for cations and anions is 2.30 Å in a cubic fluorite cell of lattice parameter 5.3 Å. Table 4.3 gives the average relaxed zirconium-oxygen bond length for each zirconium position in the ground state unit cells. In the ground states with 25, 29, and 33 % Y, the Zr-O bond lengths are nearly all 2.18-2.21 Å, which is the same as the monoclinic Zr-O bond length. One or two Zr-O bond lengths at 2.30-2.33 Å are larger than the monoclinic bond length. All Y-O bond lengths are larger than the C-type $YO_{1.5}$ bond length. In the ground state with 57 % $YO_{1.5}$, all Zr-O bondlengths deviate from the monoclinic Zr-O bond length, but the Y-O bond length is closer to C-type $YO_{1.5}$ than the lower composition structures.

4.4 Density of States

The descriptions of the ground states provide atomistic models of the structures, and the density of states of the ground states gives information about the electronic structure of the materials. The density of states for pure ZrO_2 and $YO_{1.5}$ and the intermediate composition ground state structures show degrees of hybridization depending on the amount of zirconium in each structure. Figure 4-12 gives the DOS

for each structure.

For cubic ZrO_2, the DOS for Zr d and O p states are split in to two peaks both above and below the Fermi level. Below the Fermi level, the trough between the two O p peaks and the trough between the two Zr d peaks are at the same energy, and the Zr peaks maximize at the same energy as the O peaks. The coinciding troughs and peaks suggest that the O and Zr states hybridize. Metal-oxide e_g and t_{2g} orbitals are expected to give single peaks of density. Above the Fermi level, however, the splitting of the peaks indicates that the cubic symmetry of the Zr orbitals is also broken. The ground state of ZrO_2 is the monoclinic phase, which is a distortion of the cubic fluorite phase, giving Zr atoms sevenfold coordination by oxygen. The Zr d peaks may be split due to electronic driving forces towards monoclinic while the structure maintains the unstable cubic phase.

Looking at the ground state structures with intermediate composition, the Zr d states above the Fermi level consolidate to a single peak upon the addition of Y. The majority of the yttrium density of states is in unfilled states above the Fermi level. Below the Fermi level, the filled Zr d DOS shift to the lower energy peak while the oxygen peaks combine towards the higher energy peak. This suggests the Zr-O hybridization decreases as yttrium concentration increases.

In the $YO_{1.5}$ DOS below the Fermi level, the oxygen p states are nearly a single peak and the yttrium d states are also a single peak indicating that the metal-oxygen hybridization is not present. Comparing the intermediate composition and pure $YO_{1.5}$ DOS shows that the spread of the oxygen DOS decreases and the median O p state energy increases as yttrium content increases. Zirconium bonding with oxygen pulls the oxygen p states down in energy to stabilize the structures.

4.5 Monte Carlo simulations

4.5.1 Cooling

While earlier sections of the chapter concentrated on static ordering features, Monte Carlo simulations can lend insight in to how ordering evolves across a temperature range. Monte Carlo simulations of the YSZ system require a coupled sublattice approach to model the ordering of anions on the simple cubic lattice and cations on the fcc lattice. The coupled approach is the same as traditional Monte Carlo simulations except that three sites (two cations and one anion) are chosen together to potentially switch to the alternate species rather than one site being chosen to potentially switch as in traditional Monte Carlo. The three sites must be a charge balanced combination, and the eligible combinations are either two yttrium plus one vacancy or two zirconium plus one oxygen. Two cation sites and one anion site are chosen at random from the cell, and when an eligible combination is found, it is tested for whether the energy decreases by changing those sites to the alternate species or whether to accept a higher energy change with a statistical probability.

An important problem of coupled sublattice simulations is the low acceptance rate. At 1000 K, the grand canonical acceptance rate for sites to alternate species is 10^{-4} and the canonical acceptance rate is 10^{-1}. Due to the low acceptance rates of grand canonical simulations, the number of passes to equilibrate and sample the cell was on the order of 10^6. To accelerate some calculations, a combination of grand canonical steps with intermediate nearest neighbor exchange steps allowed equilibration of the local arrangement after each grand canonical step.

Using the cluster expansion of chapter 3, an interesting property of the Monte Carlo simulation on a cell of 33% $YO_{1.5}$ is that the cations and anions order at different temperatures. Comparing the results of two types of simulations generates this conclusion. From canonical nearest-neighbor exchange simulations, cooling of the ground state structure at 33 % Y give a peak in the heat capacity at 1500 K (figure 4-14). The peak suggests a phase transition is present. In figure 4-15, comparing the correlations of the structures before and after cooling shows that the cation

correlations change markedly on cooling. The clusters with the largest change in correlations between 500 K and 3500 K came from the cation-cation second nearest neighbor cluster, the cation-cation fourth nearest neighbor cluster, two triplets with one cation and two anion sites, and nine clusters with two cation and one anion site. The peak in the heat capacity may be attributed to ordering of cation sites.

In a second type of simulation, the cation sites were fixed in each structure, and the ground state structure with 33 % $YO_{1.5}$ cooled and allowed anion nearest neighbor exchanging only. In the simulation, the heat capacity peak occured at 1750 K for the vacancy ordering, and the resulting vacancy configuration is similar to the ground state configuration with some stacking faults. The different ordering temperature of cations and vacancies supports the conclusion that ordering of oxygen and vacancies is dependent on both cation and anion interactions.

4.5.2 Lowest excitation energy

To clarify how the energy of a structure changes by diffusion of an oxygen to a vacant site, the lowest excitation energy is the energy difference, on average, that would occur from switching an oxygen and a vacancy on the anion sublattice. Calculating the lowest excitation energy requires a supercell of the ordered structure and completing one Monte Carlo iteration using the cluster expansion as the energy Hamiltonian. At each randomly selected anion lattice site, the change in energy for switching an oxygen with a nearest neighbor vacancy, whether or not the switch is accepted, is recorded. The average energy difference over all recorded anion sites is the lowest excitation energy. Figure 4-16 shows that the excitation energy increases with composition, which suggests that as Y composition increases, diffusion of oxygen is more difficult. The ground state with 33 % Y is an exception to the trend. Vacancies are distributed homogeneously across the lattice in the ground state with 33 % Y, and, in comparison to the ground state with 29 % Y, switching an oxygen and a vacancy may not greatly perturb the energetics of ordering in the 33 % Y ground state.

4.6 Conclusions

The analysis of 269 ordered YSZ compounds and the ground state structures provides insight in to the driving forces for ordering and phase stability in YSZ. With the 269 ordered structures, the calculation of the probability deviation from random for the occupation of the cation tetrahedron surrounding oxygen shows that the 3Y-Zr tetrahedra are more likely in stable compounds at high compositions than the 2Y-2Zr or Y-3Zr tetrahedra. The probability for a particular cation coordination around oxygen has a compositional dependence. The average relaxation of cations around oxygen similarly have a compositional dependence; relaxation around oxygen has less of an impact in structures with high Y content.

Considering only the ground state structures, the low Y structures have bonding similar to the parent ZrO_2 compound. A comparison of the ground state bond lengths shows that the ground states with low Y composition (25, 29, 33 % Y) have a bimodal distribution of Zr-O bond lengths. The shorter bond lengths are nearly the same as the monoclinic ZrO_2 bond length. The ground state with 57 % Y also shows bimodal bond lengths in both Zr-O and Y-O bond lengths, but neither bond type matches exactly with the bond lengths in monoclinic ZrO_2 or Y_2O_3. The density of states for each of the ground states show changing degrees of hybridization between Zr-d and O-p states across the composition range.

To further understand ordering in the YSZ systen, Monte Carlo simulations show cation and anion ordering changes with temperature. Monte Carlo simulations of the ground state with 33 % Y indicate that cation ordering is necessary to fully order the vacancies of the structure upon cooling. Despite the common practice of modelling cations with a random distribution about fcc sites, these Monte Carlo simulations indicate that cation ordering cannot be ignored in analyzing the ordering of anions.

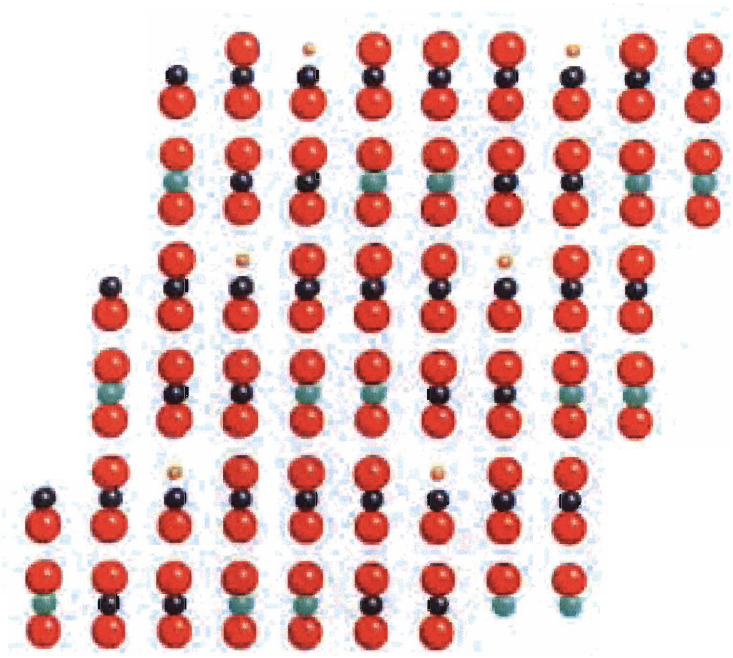

(a)

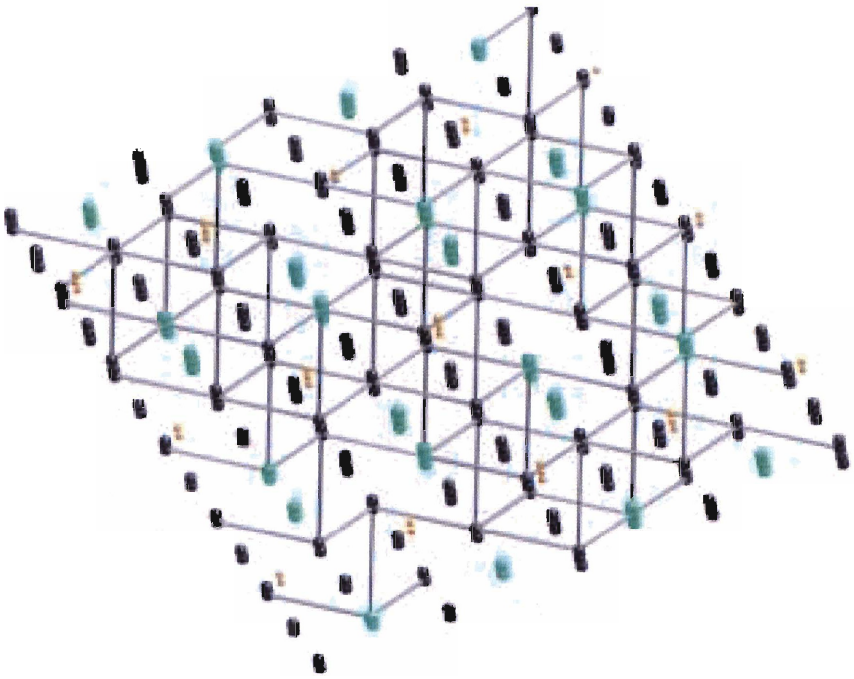

(b)

Figure 4-8: Large red ions are oxygen and small orange spheres represent oxygen vacancies. The middle sized ions represent cations. The dark grey Zr and light green Y cations are on face centered cubic positions. The figure shows the unrelaxed cubic positions. Figure (a) shows a supercell of the ground state at 25 % $YO_{1.5}$. The horizontal planes are (1 1 1), and the viewing direction in to the page is [1 1 2]. Figure (b) shows a supercell of the primitive cell with some cubic cell vectors included.

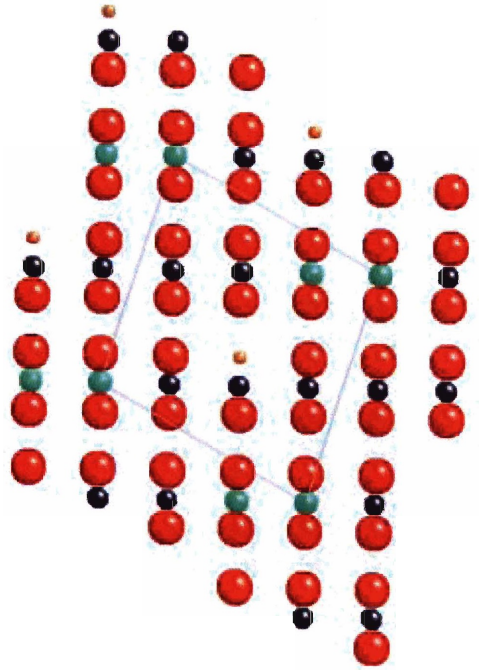

(a)

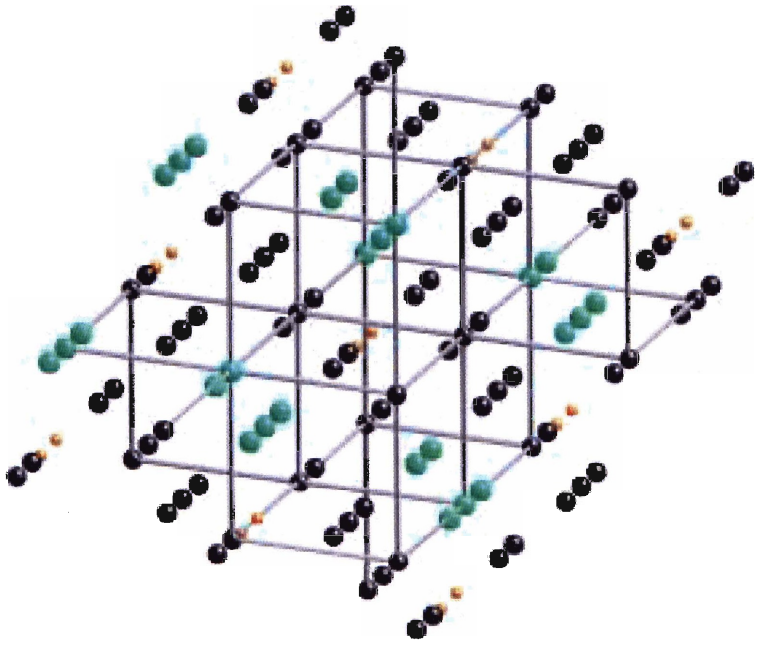

(b)

Figure 4-9: The key is the same as in figure 4-8. This structure is the ground state at 29 % $YO_{1.5}$.

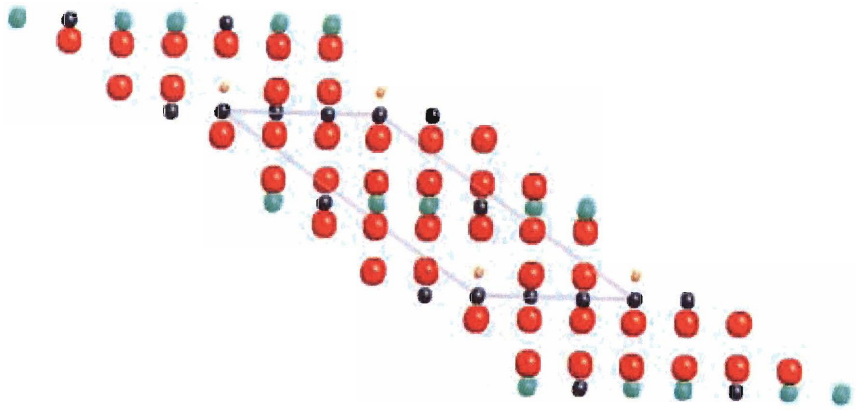

(a)

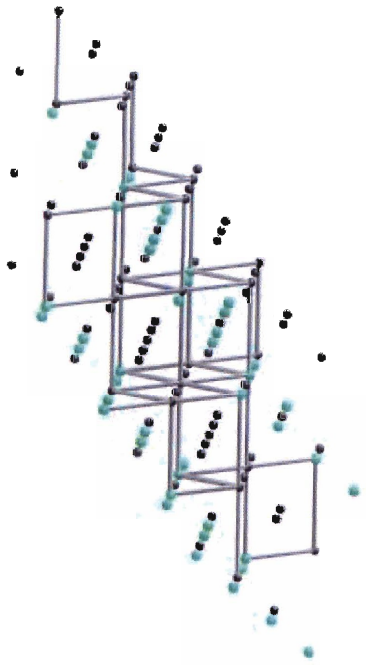

(b)

Figure 4-10: The key is the same as in figure 4-8. This structure is the ground state at 33 % $YO_{1.5}$.

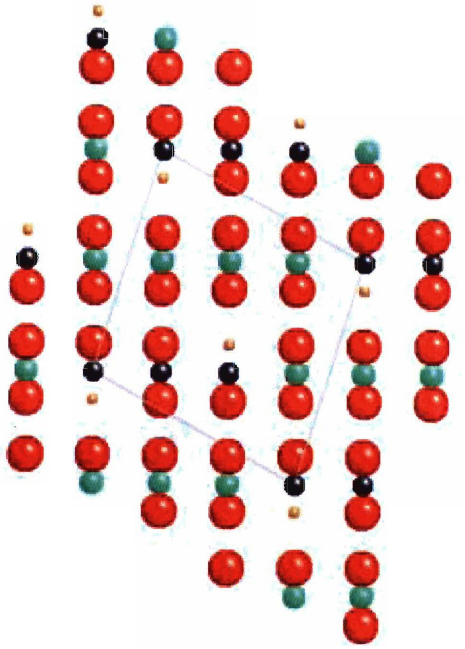

(a)

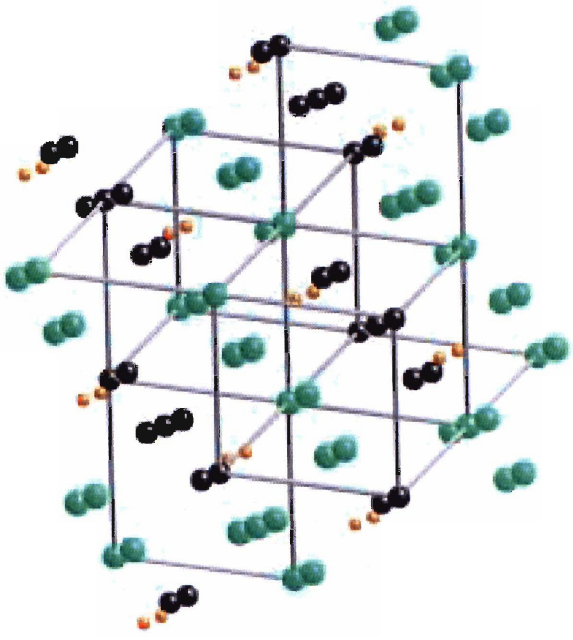

(b)

Figure 4-11: The key is the same as in figure 4-8. This structure is the ground state at 57 % $YO_{1.5}$.

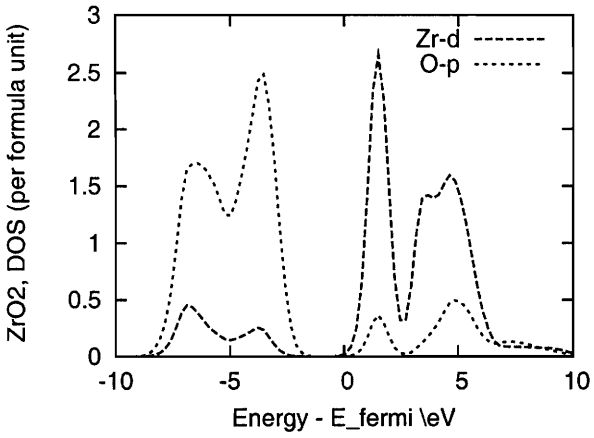

(a)

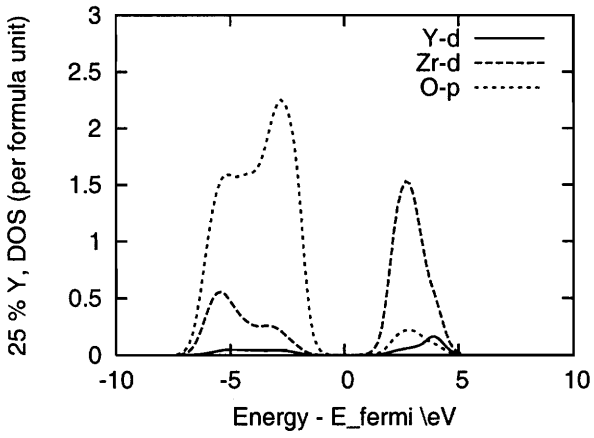

(b)

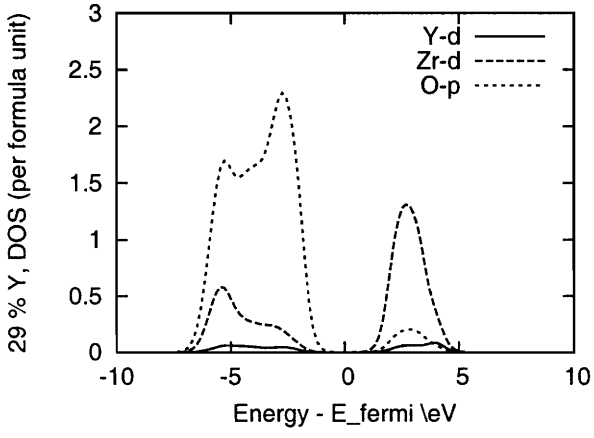

(c)

Figure 4-12: Figure (a) is the density of states for cubic ZrO_2. Figures (b) and (c) show the density of states for the ground states at 25 and 29 % $YO_{1.5}$, respectively. The thick grey dashed lines are Zr d states, and the thin green lines are Y d states. The thin dashed-dotted red lines are O p states. The units of energy are eV.

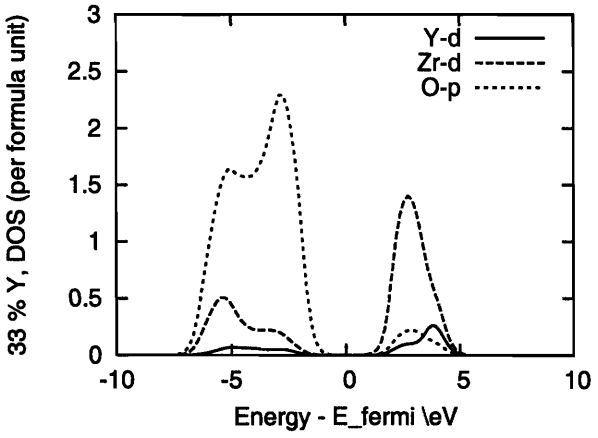

(a)

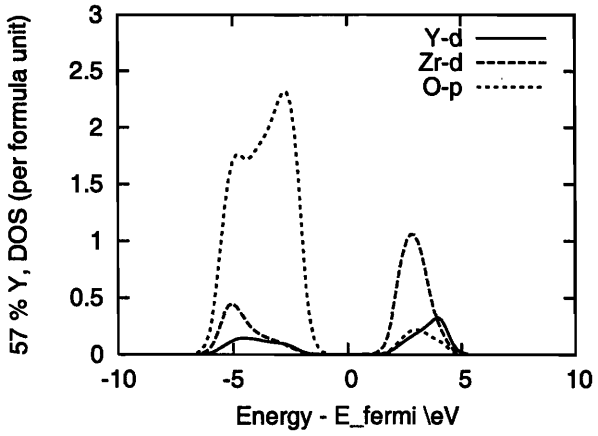

(b)

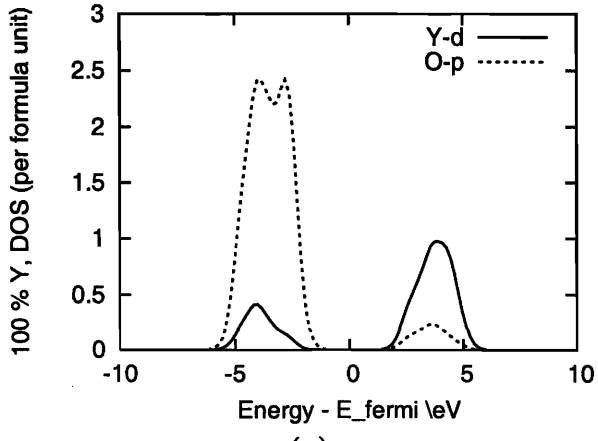

(c)

Figure 4-13: Figures (a), (b), and (c) are the density of states for the ground states at 33, 57, and 100 % $YO_{1.5}$, respectively. The units of energy are eV.

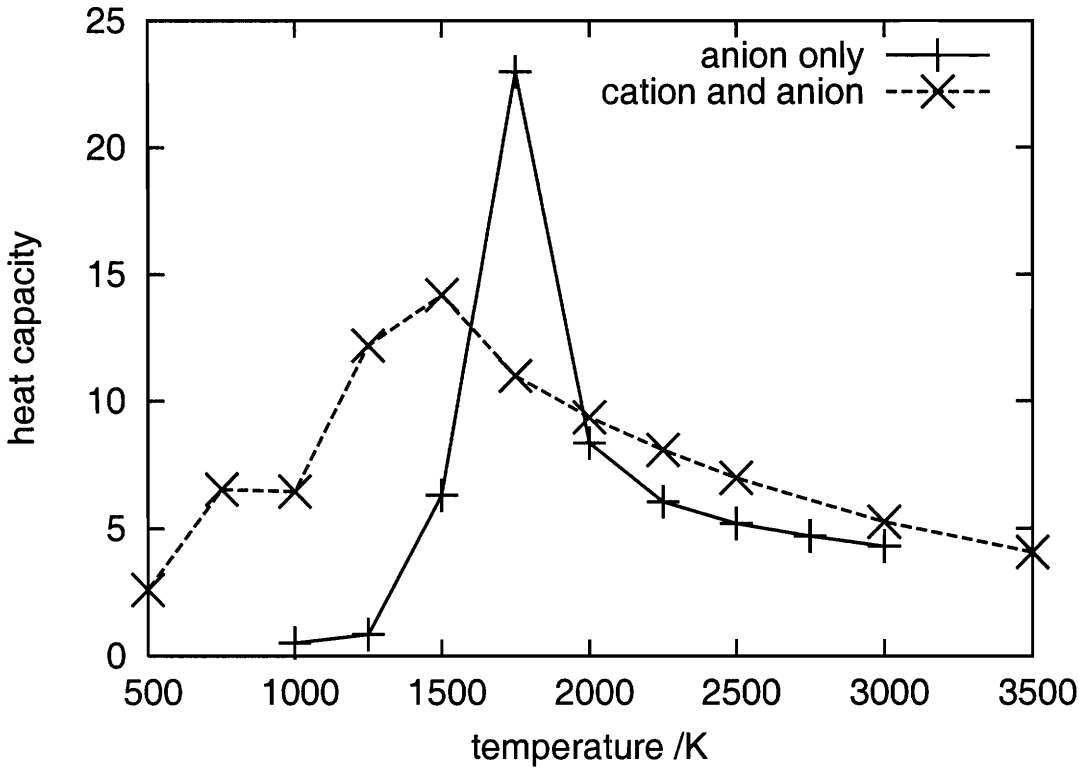

Figure 4-14: In canonical Monte Carlo cooling of the 33 % Y ground state, the peak in heat capacity differs depending on the type of site exchange. For nearest neighbor site exchanging on both cation and anion sublattices, the peak is at 1500 K. With a fixed cation sublattice and only nearest neighbor anion site exchanges, the peak is at 1750 K.

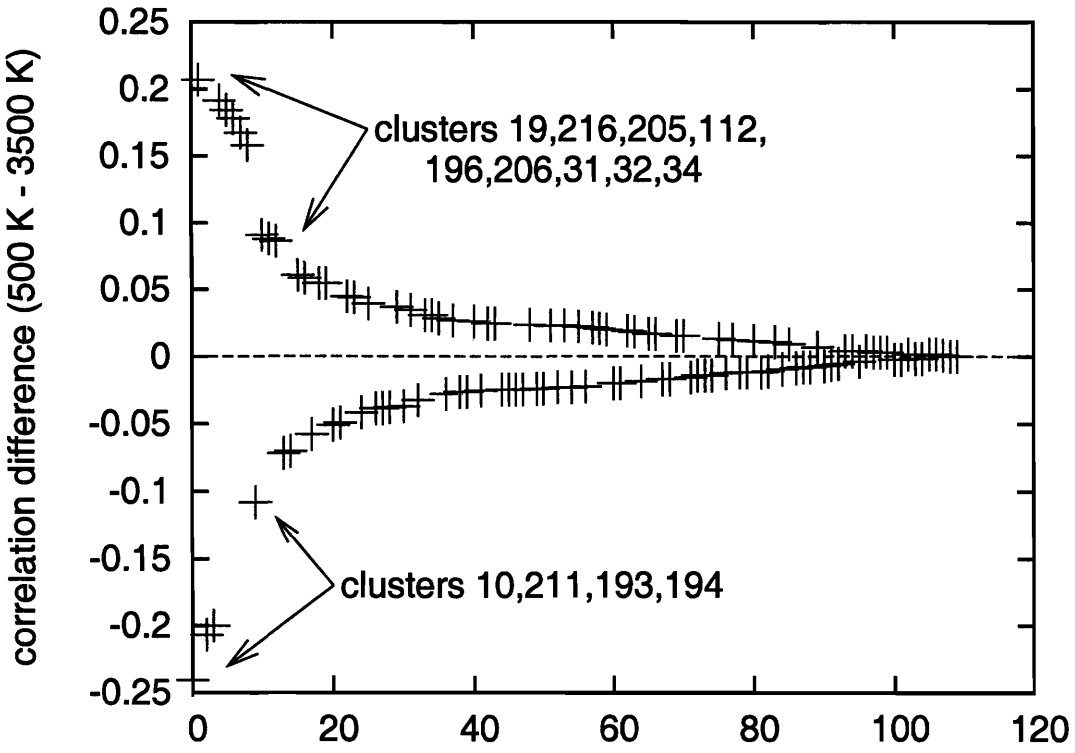

Figure 4-15: The plot contains one data point for each cluster in the cluster expansion. The ordinate value for each point is the difference between the correlations in the cooled 500 K Monte Carlo state and the starting 3500 K state for a canonical nearest neighbor exchange simulation. The points are sorted by decreasing magnitude. The labels of the first thirteen clusters are in the order of decreasing absolute magnitude and correspond to the cluster list in appendix B.

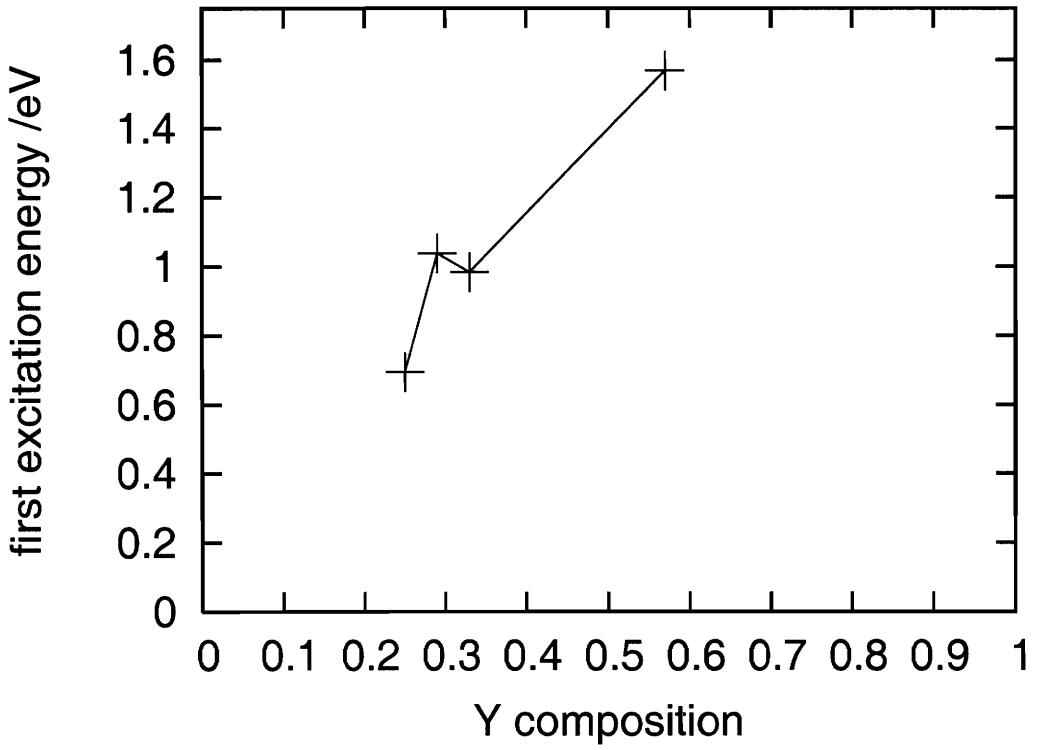

Figure 4-16: The lowest excitation energies for the ground state structures are 0.695, 1.038, 0.984, and 1.568 eV, in order of increasing Y composition.

Chapter 5

Relaxation, coordination, and cation radii

5.1 Driving forces for stability

The literature on yttria stabilized zirconia proposes factors that influence the presence of short and long range ordering in the material. The calculations of this chapter provide a closer study of several mechanisms that impact the stability of the ordered ground states reported in this thesis. The three main factors investigated are ionic relaxation, vacancies arrangements in pure ZrO_2, and the differences between zirconium and yttrium cation radii. Before discussing the main topics, two additional factors also require mention: the roles of electrostatics in ordering and the covalency of the zirconium-oxygen bond.

5.1.1 Electrostatic interaction

The most basic force between ions is the electrostatic attraction and repulsion between charged species. In YSZ, the formal valence of the species gives Zr^{+4}, Y^{+3}, and O^{-2}. Within a material, a vacancy ($\square$) in an O^{-2} site has a relative +2 charge with respect to the lattice. From electrostatic interaction, one would expect the Y-$\square$ nearest neighbor configurations to be more stable than Zr-$\square$. In all the ground states, the

latter configuration is present.

5.1.2 Zirconium-oxygen covalency

Zirconia's ground state configuration is a monoclinic structure with zirconium in seven fold coordination by oxygen. One explanation for the stabilization of monoclinic rather than cubic fluorite is that zirconium is a small ion that is ionically bonded with oxygen. The most satisfactory zirconium-oxygen bonding is seven oxygen coordinating zirconium with shorter, stronger bonds rather than zirconium being in eight fold coordination with longer, weaker bonds. By this argument, doping with a larger metal ion forces oxygen apart putting the metal in eight fold coordination and hence yielding a cubic fluorite structure.

DFT studies reproduce the relative stability of the experimentally observed monoclinic-tetragonal-cubic ZrO_2 structures [90, 91], but attempts to model structures with semi-empirical models require successively more complex pictures of bonding [92, 93, 94, 95, 11]. The basic assumption that the bond between zirconium and oxygen is ionic does not reproduce the monoclinic-tetragonal-cubic order of phase stability. Initial studies found that including the polarizability of oxygen is necessary to accurately reproduce the zirconia polymorphs [94]. Finnis, et. al. present a more elaborate model and conclude that covalency is more important than polarizability in their self-consistent tight-binding model for obtaining the experimental order [95, 11].

The degree of covalency between the oxygen and metal ions in the YSZ ground state structures may contribute to driving the system to order. A calculation of the electron localization function in the ground state with 33 % Y shows that the localization of the charge is quite similar for yttrium and zirconium in the (1 1 1) plane (figure 5-1) [96, 97]. Given this result, the analysis of the ground state structures does not focus on the electronic differences between Y and Zr but instead focuses on steric effects.

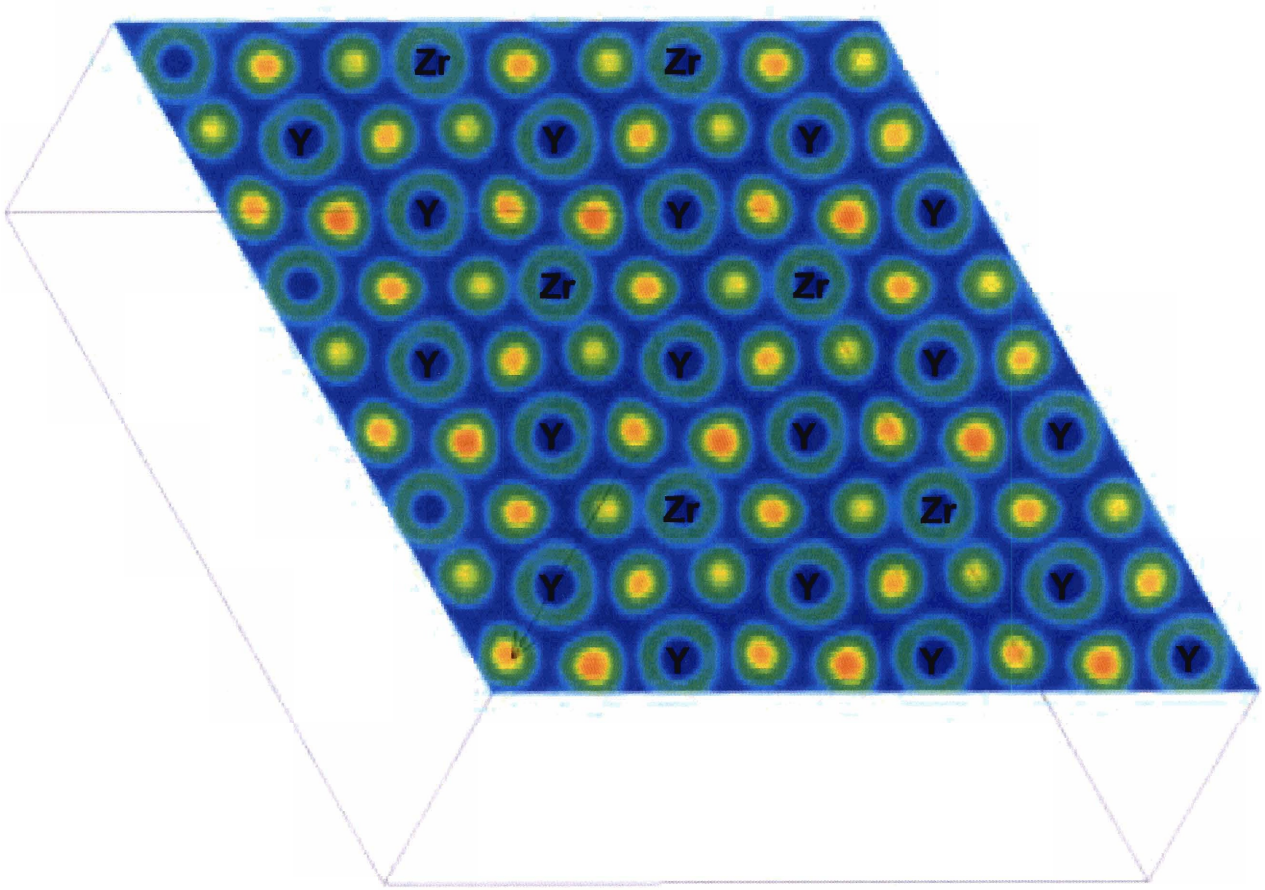

Figure 5-1: The plot of the electron localization function in the (1 1 1) cation plane of the ground state structure with 33 % Y shows rings around cation positions and circles of red where charge localizes on oxygen sites from neighboring (1 1 1) planes. Red indicates the fullest degree of localization and green indicates delocalized charge. The degree of localization for Zr and Y is similar, with the Zr localization extending closer to the neighboring oxygen than the Y localization.

5.2 Relaxation

The defining feature of yttria stabilized zirconia is the stabilization of a cubic form of zirconia upon addition of yttrium. YSZ, however, is not uniformly cubic. Local distortions around ions and vacancies are present across dopant compositions and play a role in stabilizing an overall cubic fluorite structure on the scale of 10-10^2 Å [67]. Using the energetics of relaxation and bond valence summation, we explore the nature of this stabilization.

5.2.1 Energies of cation and anion relaxation

As shown in section 4.1.1, the literature describes many ways that ions relax away from ideal cubic sites. Supercell calculations of ZrO_2 with a single vacancy show that nearest neighbor oxygen ions relax toward the vacancy in ⟨1 0 0⟩ and nearest neighbor cations relax away from the vacancy in ⟨1 1 1⟩ when Y (or larger dopant) is second nearest neighbor to the vacancy [74, 62]. In a computational study of 90 YSZ and scandia stabilized zirconias, Bogicevic, et. al. report that the energy of ions relaxing counteracts the energy of electrostatic repulsion of like species [45]. They argue that this relaxation drives the formation of ⟨1 1 1⟩ vacancy pairs, a short range ordering unit observed by Goff, et. al. [10].

Three types of total energy calculations of the ground state configurations clarify the role of cation and anion relaxation: calculation of the energy with fixed anion sites and cation sites allowed to relax, calculation of the energy with fixed cation sites and anion sites allowed to relax, and calculation of the energy with both anion and cation sites allowed to relax. For all ground states, the calculation with both anion and cation relaxation gives the lowest energy. Figure 5-2 shows the difference in energy for each ground state structure between the fully relaxed structure and the structure with cation relaxation allowed or the structure with anion relaxation allowed. From the figure, the average energy difference between fully relaxed and anion relaxed structures across the ground state configurations is 226 meV. The energy difference increases with increasing $YO_{1.5}$ composition.

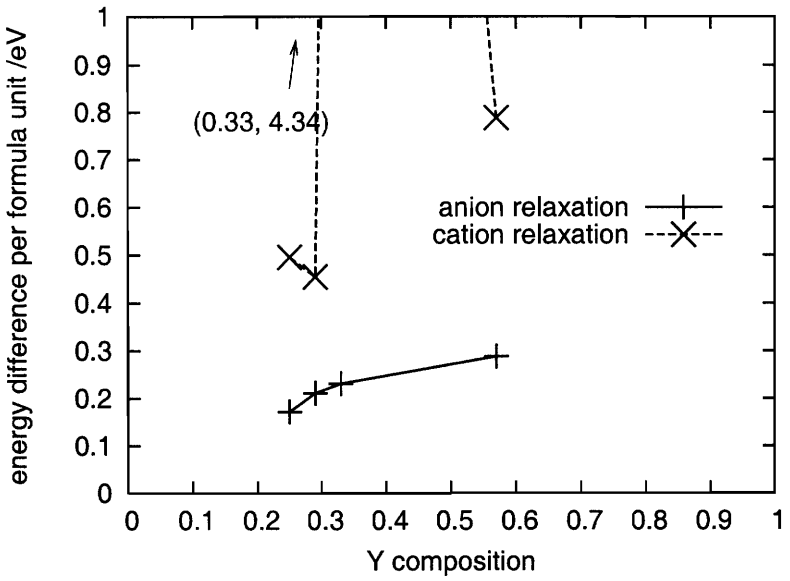

Figure 5-2: The cation relaxation curve gives the difference in energy between the ground state with cation sites allowed to relax and anion sites fixed and the ground state with anion and cation sites relaxed. The anion relaxation curve is the analogous difference in energy but with the first structure being the ground state with anion sites allowed to relax and cation sites fixed.

The differences in energy between the fully relaxed structures and structures with cation relaxation and fixed anion sites are less uniform. The energy difference for ground state with 33 % Y is 4.34 eV. The large energy change for this case is likely due to metal-oxygen bond lengths. Three of the eight yttrium-oxygen distances decrease by 0.2 - 0.3 Å upon cation relaxation. The zirconium-oxygen distances span a large range from 2.03 to 2.48 Å. The large energy difference for the ground state at 33 % Y is reminiscent of the destabilizing affect of cation relaxation around oxygen for structures at this composition in section 4.2.2. The destabilizing nature of cation relaxation in this ground state may be a result of the zirconium being in the monoclinic-like seven fold coordination in the ground states. The driving force for zirconium to be in this coordination may be so great that changes in its position with respect to oxygen greatly impact the energy.

atom pair	R_0 (Å)	B (Å)
Y-O	2.019	0.37
Sc-O	1.849	0.37
Zr-O	1.928	0.37

Table 5.1: The table lists the bond valence parameters for yttrium, scandium, and zirconium with oxygen [1].

5.2.2 Bond valence summation

To take a closer look at how the relaxations affect bonding, consider the bond valence sums for the ions in each groundstate. Bond valence summation is a method that describes the nature of bonding between anions and cations by considering the coordination and distances between atoms. For a central atom i, the bond valence summation V_i is

$$V_i = \sum_j exp\left(\frac{R_0 - R_{ij}}{B}\right) \tag{5.1}$$

R_0 and B are fitted parameters derived from bond lengths between atoms in the Inorganic Crystal Structure Database [1]. R_{ij} is the bond length between a central atom and its neighbor j, and R_0 is the length of a bond of unit valence. Table 5.1 gives the parameters for some relevant atom pairs.

Figure 5-3 shows the bond valence summation for each ground state. Each graph contains the bond valence summation from four energy calculations of the ground state: the structure with ions in unrelaxed cubic fluorite positions, the structure with all cations and anions allowed to relax, the structure with cations in fixed cubic positions and anions allowed to relax, and the structure with anions in fixed cubic positions and cations allowed to relax. For all ground states, the trend between the unrelaxed cubic and fully relaxed states shows that V_i of zirconium changes from approximately 2.5 to 3.5 upon relaxation, and V_i of yttrium shifts from approximately

4 to 2.75 upon relaxation. The increase (decrease) of V_i for zirconium (yttrium) towards 4+ (3+) is in agreement with bond valence summation rules. In structures where the bonding can be described by localized bonds between atoms, the ions have a coordinating environment such that V_i is the same as the formal charge valence [98].

When comparing the structures with cations in fixed positions and anions relaxed and the structures with all cations and anions relaxed, the V_i for the two types of structures across the ground states are nearly the same and are closest in the ground states with 33 and 57 % Y. The relatively small energy difference between the fully relaxed structures and the structures with anion relaxation and cations in fixed cubic positions in figure 5-2 show that anion relaxation is an important driving force in the stabilization of the ground states. Given that the bond valence sums between the two types of structures in the ground state configuration at 57 % Y are nearly the same, but the energy difference between the two structures is largest at that composition, another factor relating to the cation positions must be an important driving force for the stabilization of the fully relaxed ground state at 57 % Y.

In the structures with anions in fixed sites and cations in relaxed positions, the V_i of the zirconium ions is intermediate between the unrelaxed cubic structures and the structures with all anion and cations in relaxed positions. The yttrium ions in the structures with cation relaxation have nearly the same V_i as in the unrelaxed structures. The main stabilization mechanism in the structures with cation relaxation and no anion relaxation is the displacement of zirconium, which may be a result of zirconium being a smaller ion than yttrium and having available space within its coordinating environment to change position.

5.3 Vacancy ordering

An early study by Ho on the coordination of the cations in YSZ claimed that if vacancies always coordinate zirconium and not yttrium, the material becomes cubic when half of the zirconium cations are seven fold coordinated by oxygen [99]. Half

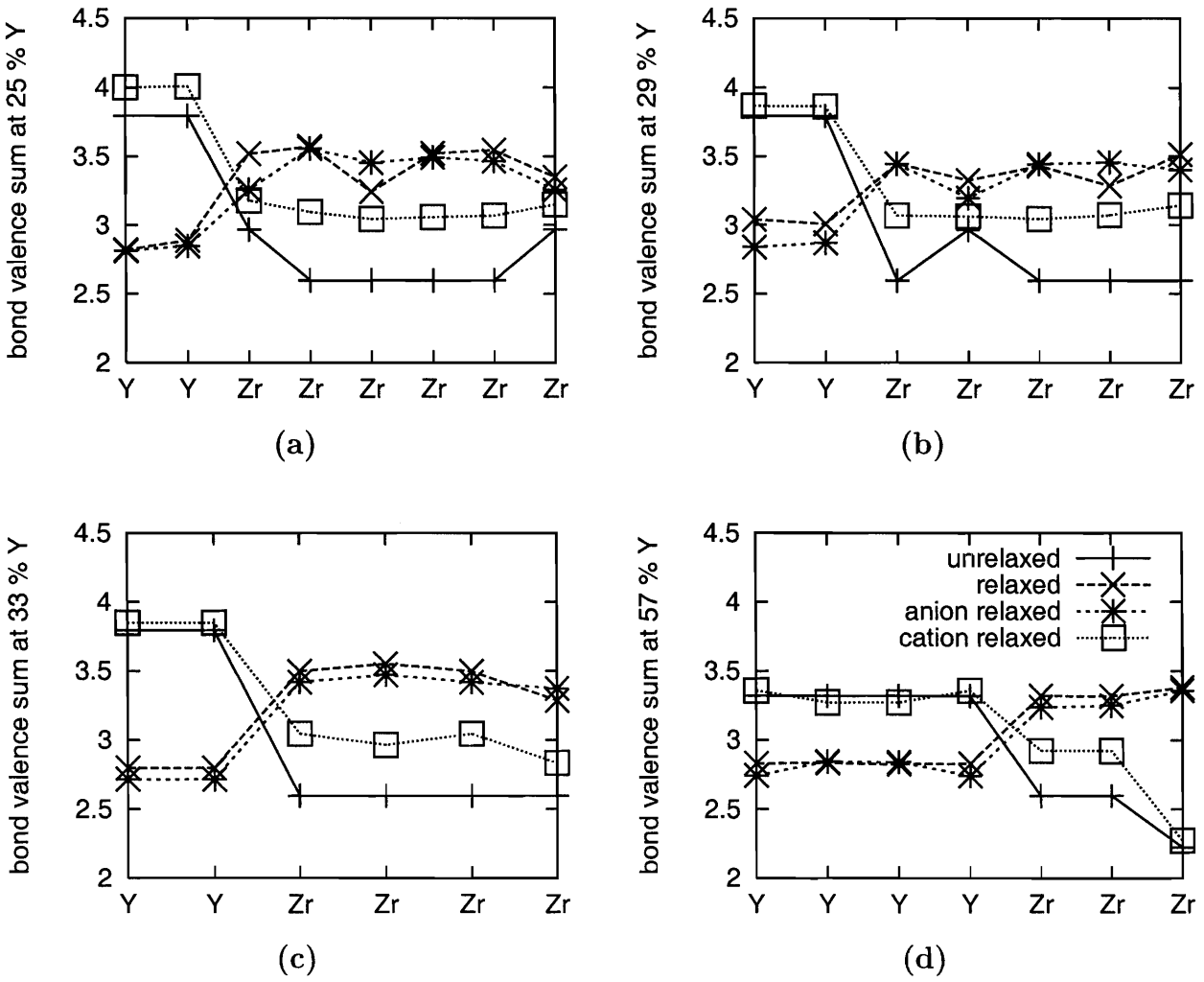

Figure 5-3: Each plot contains V_i for each cation in the unit cell in the unrelaxed, fully relaxed, anion relaxed, and cation relaxed structures for ground states with 25 % (a), 29 % (b), 33 % (c), and 57 % (d) Y.

of zirconium can be seven fold coordinated when 5 % vacancies exist on the anion sublattice, which occurs at 20 % $YO_{1.5}$ doping. The argument further states that zirconium in seven fold coordination and yttrium in eight fold coordination by oxygen would yield the most stable arrangement of vacancies. With 33 % Y, all zirconium can be seven fold coordinated, and the calculated ground state at 33 % Y has this arrangement.

In addition to the sevenfold coordination of zirconium, one may also question how the arrangement of vacancies themselves affects the stability of structures. Using supercells of ZrO_2, Fabris, et. al. add four vacancies to a system of 32 Zr and 64 anions sites [49]. They compare two arrangements of vacancies: vacancies at maximum separation and vacancies in a [1 1 1] chain. The latter arrangement is lower in energy. The arrangement of vacancies clearly impacts the energy of the structure beyond just the energy of electrostatic repulsion.

To compare their findings to the ground state structures, one can consider the vacancy configuration in the ground state with 25 % $YO_{1.5}$. Calculating the DFT energy of three ZrO_2 supercells provides a comparison of vacancy configurations. The vacancy configurations considered were the two used in the Fabris study and the vacancy configuration of the ground state structure with 25 % $YO_{1.5}$ imposed on a supercell of ZrO_2 (i.e. no yttrium were present). Since the ZrO_2 supercells are not charge balanced due to the presence of vacancies but no yttrium, two electrons were removed from the energy calculation for each vacancy. The energy calculations indicated that the 25 % Y ground state configuration of vacancies had the lowest energy. The [1 1 1] vacancy configuration and the maximum vacancy separation are 0.104 eV and 0.127 eV, respectively, higher in energy than the ground state configuration.

The 25 % Y ground state vacancy configuration is similar to the maximum vacancy separation configuration. In the former structure, each vacancy has four neighboring vacancy neighbors at sixth nearest neighbors and two at seventh nearest neighbors. In the latter configuration, the vacancies are all at seventh nearest neighbors. The average V_i of zirconium for the three structures are 3.641, 3.626, and 3.628 for the

25 % Y ground state configuration, the [1 1 1] vacancy configuration, and the maximum vacancy separation. The bond valence sum is the largest for the ground state configuration, suggesting that the bond lengths are able to relax to optimal lengths. This relaxation drives the stabilization of the vacancy arrangement. Kaiser-Bischoff, et. al. propose that a model of rigid Zr-O entities with short interatomic bonds (2.1 Å) that relax as a unit is important for short range ordering [100].

5.4 Cation radii

The difference in size between zirconium and yttrium may contribute to the stabilization of ordered compounds. A variety of studies consider the trends of cation size differences on the cubic fluorite structure of doped transition metal oxides. Many attempts to predict the formation of the ordered pyrochlore structure with formula $A_2B_2O_7$ exist for fluorite based oxides [101]. A map of six fold coordinated, 4+ valent cations versus eight fold coordinated, 3+ valent cations shows that a range of compounds stabilizes in the pyrochlore structures depending on the size of the cations. One estimate is that the $\frac{r(A^{3+})}{r(B^{4+})}$ ion radius ratio must be at least 1.22 for pyrochlore to form [12]. Neutron and x-ray diffraction investigations of pyrochlores find that doping the A and B sites with different sized transition metal oxides will drive order and disorder of the pyrochlore at the $A_2B_2O_7$ composition [102, 103].

Brisse reports that in stannate oxide compounds, the influence of yttrium in the pyrochlore ordering is due to its size and not chemical bonding [104]. If this is true in other fluorite oxides, one may consider how the size of yttrium in zirconia influences ordering. YSZ does not form a pyrochlore structure, but it does form the 57 % Y-δ ground state structure. Brisse suggests that when the $\frac{r(A^{3+})}{r(B^{4+})}$ ratio in A_2O_3-BO_2 compounds is below 1.19, a δ compound forms in favor of a pyrochlore compound [104].

To investigate this phenomenon in YSZ, consider the relative sizes of scandium, yttrium, and zirconium. Table 5.2 shows the cation radii in six fold and eight fold coordination. The scandium ion is smaller than yttrium and larger than zirconium.

ion	6 fold (Å)	7 fold (Å)	8 fold (Å)
Y^{3+}	0.89	N/A	1.02
Sc^{3+}	0.73	N/A	0.87
Zr^{4+}	0.72	0.78	0.84

Table 5.2: The radii of the transition metals vary by their coordination in a compound [2].

Experiments reveal several ordered phases in the Sc_2O_3-ZrO_2 system. Sc_2O_3 takes the C-type lanthanide structure like Y_2O_3, a δ structure is stable at $Sc_4Zr_3O_{12}$ (57 % Sc), an experimentally observed γ compound is stable at $Sc_2Zr_5O_{13}$ (29 % Sc), and a disputed β phase occurs at $Zr_{50}Sc_{12}O_{118}$ (19 % Sc) [105]. Bogicevic, et. al. offer unit cells and atomic positions of the scandium δ and γ compounds [40, 46].

A relevant extension to the observations on pyrochlores is to investigate whether the difference in ion sizes has an impact on stabilization at the 25 %, 29 %, and 33 % compositions where YSZ has ground states. The total energies of the 25 %, 29 %, 33 %, and 57 % doped structures with scandium rather than yttrium, as well as the reported δ and γ structures, were calculated. Figure 5-4 shows the formation energy at each composition with respect to cubic ZrO_2.

At 57 % scandium composition, the reported Sc-δ structure is lower in energy than the YSZ-δ ground state structure by 25 meV. The configurational difference between the YSZ-δ and the Sc-δ depends on the coordination of the cations. In the YSZ ground state, zirconium is six fold coordinated such that vacancies are at the body diagonals of a simple cube with zirconium in the middle. All yttrium are seven fold coordinated. In the lower energy Sc-δ structure, the scandium is in the six fold coordinated sites and zirconium is in seven fold coordination [46].

At 29 % scandium composition, the YSZ ground state configuration is lower in energy than the reported γ structure by 19 meV. The Sc-γ structure has half of its Sc and Zr ions in seven fold coordination by oxygen. The other half of Sc and Zr ions are in eight fold coordination by oxygen, except for one Zr ion, which is in six fold coordination by oxygen. The YSZ configuration, in contrast, has all Sc ions and one Zr ion in eight fold coordination by oxygen and the remaining four Zr ions in seven

fold coordination by oxygen. The structure that maximizes the fraction of zirconium ions with seven coordinating oxygen ions is the most stable.

The formation energies of the structures with respect to monoclinic ZrO_2 show that none of the configurations are stable with respect to pure zirconia and pure scandia. Bogicevic, et. al. found a similar situation in their study of doped zirconias [46]. One possible explanation is that the DFT calculation of monoclinic ZrO_2 does not accurately model the energetics of the material. Another possible explanation is that none of calculated configurations at 29 and 57 % Sc are the true ground states for this system.

Two questions arise from these calculations. Why are the cation arrangements at 57 % dopant in opposite oxygen coordination environments between the Y-doped and Sc-doped zirconias? Why is the 29 % Sc compound stable on the cubic lattice but not the structure at 33 % Sc like the analogous ground state structures with Y doping? A possible explanation involves consideration of electronic and relaxation contributions to the energy. The electronic contribution is the driving force for zirconium preferring to be in seven fold, monoclinic-like coordination by oxygen. The relaxation contribution is the decrease in energy that occurs when oxygen relax toward vacancies. At 57 % doping with yttrium, if the yttrium were in the six fold sites, the large size of the ion may cause large disturbances in the lattice such that oxygen cannot relax evenly. The electronic driving force for zirconium to be in the seven fold sites is less than the relaxation driving force for Y to be in seven fold site. The yttrium, hence, reside in seven fold sites while zirconium are in six fold sites at 57 % Y doping. In scandium doping, scandium is smaller than yttrium and would be expected to cause less disturbance to the relaxation. The zirconium's seven fold electronic driving force then drives the order and scandium is in the six fold sites.

For the second question about stabilization with 29 % doping, consider the same driving forces. With 33 % Y doping, zirconium is in seven fold coordination, and the yttrium are in eight fold coordination. Section 4.2.2 found that additional relaxation beyond the ground state relaxation was unstable in structures at 33 % Y doping. Zirconium maintains seven fold coordination at 29 % and 33 %, but with Sc doping,

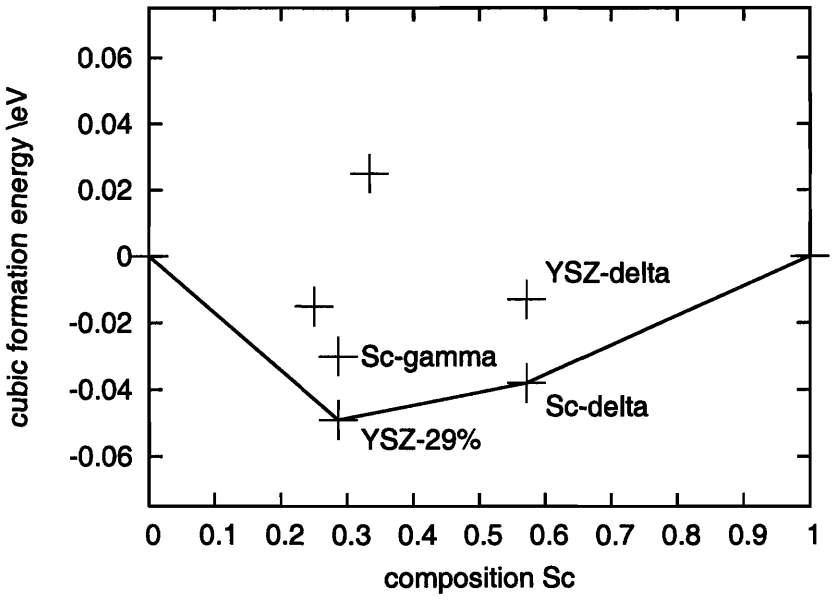

Figure 5-4: The plot shows formation energies of structures in the zirconia-scandia system with respect to cubic ZrO_2 and C-type $ScO_{1.5}$. The structures with 25 and 33 % Sc are the YSZ ground state configurations with Sc replacing Y. Points labelled Sc-delta and Sc-gamma show the energies of the reported stable phases at their compositions. Points labelled YSZ-29% and YSZ-delta show the energies of the YSZ ground state configurations with Sc in Y sites.

however, the relaxation characteristics would be expected to be different. The smaller Sc ion may allow more oxygen relaxation that would then drive the system to stabilize making 29 % be on the cubic convex hull.

5.5 Conclusions

Three factors in this chapter examine driving forces for stability in YSZ. Comparing the total energy of the ground states with full ion relaxation and with relaxed anion positions but fixed cation positions probes the importance of relaxation. Comparing the energy difference and the bond valence summation difference for the two versions of each ground state leads to the conclusion that at the highest yttrium content (57 % Y), anion relaxation alone does not fully account for the stability of the structure.

Another factor considered in chapter 5 is the arrangement of vacancies. The lowest energy vacancy arrangement among three ZrO_2 supercells with the same vacancy concentration is the arrangement from the YSZ ground state with 25 % Y. The lowest energy arrangement has the maximum average bond valence summation, and stability of the configuration may be related to a Zr-O pair relaxing as a unit.

The last factor considered is the role of cation size. Using the set of reported scandia-zirconia ordered structures and the YSZ ground state structures, incorporating scandia in to zirconia creates ground states at 29 % and 57 % Sc on the cubic fluorite lattice. The 57 % dopant structures for YSZ and Sc-ZrO_2 have opposite arrangements of cations, but the 29 % dopant ground states are the same. At the lower composition, anion relaxation may be the same for both types of dopants hence stabilizing the same structures; at higher compositions, though, the difference in sizes of Sc and Y may drive the dopants to seek their unique stable configurations.

Chapter 6

Conclusions

6.1 Summary and contributions

The major contributions of this work are twofold: the discovery of ordered ground states at 25, 29, and 33 % $YO_{1.5}$ on the cubic fluorite lattice and an analysis of the factors driving order and stability across the composition range of ZrO_2-Y_2O_3. The first main contribution was obtained with a coupled cluster expansion of YSZ. The implementation of a cluster expansion involves a blend of standard statistical practice and heuristic understanding to parameterize accurate DFT calculations. Chapter 2 offers a guide for navigating the process. The chapter first emphasizes the importance of defining an explicit purpose and then offers suggestions to achieve that aim.

The results of the cluster expansion of YSZ are in chapter 3. By iteratively identifying prospective low energy structures, the cluster expansion provided a path to find the ordered ground states at 25, 29, and 33 % $YO_{1.5}$. The ground states with 25 % and 29 % Y are the lowest energy structures in their respective compositions, but their energies are higher than the tieline between the energies of monoclinic ZrO_2 and δ-$Y_4Zr_3O_{12}$. The energy of the ground state with 33 % $YO_{1.5}$ is, however, below the tieline of monoclinic ZrO_2 and δ-$Y_4Zr_3O_{12}$ energies, making the ground state part of the convex hull with respect to monoclinic zirconia. The ground state with 33 % $YO_{1.5}$ has all zirconium in seven fold coordination, which is a hallmark of stability in monoclinic zirconia.

The ECI of the cluster expansion show that anion-anion pair clusters follow repulsive energetics for nearly all terms, and cation-anion pair ECI are repulsive for nearest and next nearest neighbors but are negligible for larger pair clusters. The pair ECI follow expected behavior for species interacting electrostatically. The large number of anion triplets modifying the anion pair terms supports the understanding that oxygen relaxation is an integral part of the energetics of this system. Additional cluster expansions at single compositions show that cation clusters become more important in cluster expansions of higher yttria content.

The second major contribution of this work is the analysis of the factors driving order and stability. The driving forces for stability are found to be composition dependent. At low compositions, oxygen relaxation towards vacancies and zirconium in seven fold oxygen coordination is important, while at high compositions, the arrangement of cations is important. The role of cation ordering is not often addressed in the literature of YSZ, and most previous studies concentrate on the position of the cation dopant with respect to vacancies in a dilute regime. The calculations shows that both oxygen relaxation and cation ordering take place across the composition range of structures, but the driving force for stability likely shifts from one mechanism to the other in the 33-50 % Y doping range.

Chapter 4 details several studies that lead to the determination that driving forces are composition dependent. One investigation involves the cation coordination around oxygen in 269 structures. The analysis shows that the probability deviation from random of a given occupation of the cation tetrahedron cluster around oxygen changes across yttria compositions. The preferred oxygen coordination thus changes with composition. A similar investigation on the average relaxation of cations around oxygen shows that relaxation becomes less important in higher yttria compositions.

In all ground state structures, vacancies are nearest neighbors to zirconium, not yttrium, and the density of states for each ground state suggest some hybridization between Zr-d and O-p states that becomes less prominent as the concentration of Y increases. Monte Carlo simulations of the ground state with 33 % $YO_{1.5}$ show that the ordering of the vacancies is not independent of the cation configuration and that

the vacancy ordering upon cooling is sensitive to the ordering of cations. The role of cations must be considered for an accurate analysis of the material.

Further studies on phase stability in chapter 5 consider three factors: anion relaxation, vacancy ordering, and cation radii. In a study of the ground states, the difference in energy between fully relaxed and anion relaxed structures is smallest for zirconia rich compounds and largest for yttria rich compounds. Bond valence sums of the fully relaxed and anion relaxed structures are nearly the same. The smallest difference in bond valence sum between fully relaxed and anion relaxed structures is in the most yttrium rich ground state, which suggests a further driving force besides the zirconium-oxygen bond lengths is important for stabilizing the structure.

To clarify the importance of vacancy ordering and zirconium-oxygen bond lengths in dilute vacancy situations, calculation of the energy of supercells of ZrO_2 with vacancies show that differences in vacancy arrangement impact the energies. The structure with average bond valence sum of zirconium closest to the formal charge valence 4+ is the most stable structure. The last factor of interest are the cation radii. When scandia replaces yttrium in the ground state configurations, a 29 % Sc ground state is stable with respect to cubic ZrO_2 and δ $Sc_4Zr_3O_{12}$ while the 25 % Sc and 33 % Sc configurations are not stable. The lowest energy structures at 29 and 57 % Sc have zirconium primarily in seven fold coordination. In YSZ, the 57 % Y structure has zirconium in six fold coordination. Dopants with different sizes (whether Sc or Y) impact whether the zirconium will be in seven fold coordination and what low dopant compositions are stable.

6.2 Suggestions for further work

Further work on this system is necessary to fully quantify the driving forces for order and to understand how ordering may influence the diffusivity of oxygen. One way to quantify the ordering behavior of the system and the diffusivity of oxygen is to create a more accurate cluster expansion. Since relaxation plays a crucial role in the stability of YSZ especially at low compositions, quantifying relaxation explicitly and

including it in to the expansion would be one approach to further improve the cluster expansion.

The interplay among oxygen relaxation around vacancies, zirconium with seven fold oxygen coordination, and atomic displacements due to the size of the yttrium dopant (particularly in non-dilute concentrations) requires further study. The factors are not necessarily independent. Oxygen relaxation toward vacancies may occur due to neighboring oxygen repulsion and to minimize free volume, or oxygen relaxation may occur to put zirconium in seven fold coordination. Seven fold coordination of zirconium may be favorable due to covalent bonding between zirconium and oxygen. One possible feature of the system may be one zirconium and one oxygen strongly bonded and relaxing together as a unit [100]. Greater insight in to the electronic structure of monoclinic zirconia and the impact of yttrium doping on the bonding behavior of Zr-O is necessary.

This investigation finds a composition dependence in the stabilizing driving forces. As more yttria is added to zirconia, the effect of the vacancies may initially be important for ordering and coordinating zirconium, but with at least 33 % Y doping, enough vacancies are present for all Zr to be seven fold coordinated. Cation configurations that minimize distortion may be the driving force for phase stability at greater Y compositions. Studies that model cation configurations at different compositions with several dopant sizes could clarify the cation driving force. Since the factors for ordering come from both cation ordering, anion relaxation, and possibly covalent bonding of Zr-O, the ultimate driving force may switch from one driving force at low compositions to another driving force at high compositions. Further calculations may be able to identify the composition where the driving force changes.

Appendix A

Derivation of ECI variance

Consider all possible energies and correlations possible for a system. For the vector of all possible $\vec{y}$ of energies; $\mathbf{X}$, a matrix of correlations (one row for each structure); and a vector $\vec{b}$ of eci to be determined, the following is true.

$$\vec{y} = \mathbf{X}\vec{b}$$

$$\mathbf{X}^T\vec{y} = \mathbf{X}^T\mathbf{X}\vec{b}$$

$$\vec{b} = \left(\mathbf{X}^T\mathbf{X}\right)^{-1}\mathbf{X}^T\vec{y} \tag{A.1}$$

The following equality is true if $\mathbf{X}$ is a matrix of constants, $\vec{y}$ is a column vector, and $\mathbf{X}\vec{y}$ exists and is a column vector[106]

$$\sigma^2_{\mathbf{X}\vec{y}} = \mathbf{X}\sigma^2_{\vec{y}}\mathbf{X}^T \tag{A.2}$$

The matrix $\sigma^2_{\vec{b}}$ gives the covariance of the eci:

$$\begin{bmatrix} \sigma^2_{\vec{b}_0} & \sigma^2_{\vec{b}_0\vec{b}_1} & \cdots & \sigma^2_{\vec{b}_0\vec{b}_m} \\ \vdots & \vdots & \ddots & \vdots \\ \sigma^2_{\vec{b}_m\vec{b}_0} & \sigma^2_{\vec{b}_m\vec{b}_1} & \cdots & \sigma^2_{\vec{b}_m} \end{bmatrix}$$

The diagonal terms are the variance of each eci, and the off diagonal terms are the covariance between two eci. The variances may be found from the correlation matrix.

Using A.1

$$\sigma^2_{\vec{b}} = \sigma^2_{(\mathbf{X}^T\mathbf{X})^{-1}\mathbf{X}^T\vec{y}}$$

Using A.2

$$\sigma^2_{\vec{b}} = [(\mathbf{X}^T\mathbf{X})^{-1}\mathbf{X}^T]\sigma^2_{\vec{y}}[(\mathbf{X}^T\mathbf{X})^{-1}\mathbf{X}^T]^T$$

Invoking $(\mathbf{AB})^T$=$\mathbf{B}^T\mathbf{A}^T$

$$\sigma^2_{\vec{b}} = [(\mathbf{X}^T\mathbf{X})^{-1}\mathbf{X}^T]\sigma^2_{\vec{y}}\mathbf{I}[(\mathbf{X}^T\mathbf{X}^T\mathbf{X})^{-1}]^T$$

$$\sigma^2_{\vec{b}} = \sigma^2_{\vec{y}}[(\mathbf{X}^T\mathbf{X})^{-1}\mathbf{X}^T\mathbf{I}\mathbf{X}(\mathbf{X}^T\mathbf{X})^{-1}]$$

$$\sigma^2_{\vec{b}} = \sigma^2_{\vec{y}}[(\mathbf{X}^T\mathbf{X})^{-1}\mathbf{X}^T\mathbf{X}(\mathbf{X}^T\mathbf{X})^{-1}]$$

$$\sigma^2_{\vec{b}} = \sigma^2_{\vec{y}}[(\mathbf{X}^T\mathbf{X})^{-1}\mathbf{I}]$$

$$\sigma^2_{\vec{b}} = \sigma^2_{\vec{y}}(\mathbf{X}^T\mathbf{X})^{-1} \tag{A.3}$$

The variances of the eci, $\sigma^2_{\vec{b}}$, therefore depend on the variance of the energies, $\vec{y}$ and the diagonal elements of the $(\mathbf{X}^T\mathbf{X})^{-1}$ matrix.

For a sample subset of all the possible structures, the variance of the eci for the sample $s^2_{\vec{b}_i}$ can be estimated by

$$s^2_{\vec{b}_i} = s^2_{\vec{y}_i}c_{ii} \tag{A.4}$$

where $s^2_{\vec{y}_i}$ is the variance of the sample energies and c_{ii} are the diagonal elements of the $(\mathbf{X}^T\mathbf{X})^{-1}$ matrix. The variance $s^2_{\vec{y}_i}$ is given by

$$s^2_{\vec{y}_i} = \frac{\sum_{i=1}^{N}(y_i - \hat{y}_i)^2}{n-k} \tag{A.5}$$

where y_i is the computed energy of a structure, $\hat{y}_i$ is the cluster expanded energy of a structure, n is the number of energies in the fit, and k is the number of eci.

Appendix B

Clusters of the YSZ cluster expansion

The cv score minimizing cluster expansion in section 3.3 uses 111 clusters, of which 27 are pairs in the first table and 82 are the triplets in the second table. The coordinate system assumes a cubic fluorite scheme with cations in an fcc cube with anions in tetrahedral interstices. The origin is a cation site at one corner of the fcc cube. Sites with coordinates of 0 or integer multiples of 0.5 and 1 are cation sites; sites with coordinates at integer multiples of 0.25 or 0.75 are anion sites.

(3) 1.472 eV	0 0 0 0.25 0.25 0.25	(4) 1.602 eV	0.25 0.25 0.25 0.25 0.25 0.75	(5) -0.025 eV	0 0 0 0 0.5 0.5
(6) 2.061 eV	0.25 0.25 0.25 0.25 0.75 0.75	(7) 1.182 eV	0 0 0 -0.25 0.25 0.75	(8) 0.931 eV	0.25 0.25 0.25 -0.25 0.75 0.75
(9) -0.447 eV	0.25 0.25 0.25 0.75 0.75 0.75	(10) -0.046 eV	0 0 0 0 0 1	(11) 1.730 eV	0.25 0.25 0.25 0.25 0.25 1.25
(12) -0.808 eV	0 0 0 0.25 0.75 0.75	(13) 1.153 eV	0.25 0.25 0.25 0.25 0.75 1.25	(14) 0.218 eV	0.25 0.25 0.25 -0.25 0.75 1.25
(15) 0.029 eV	0 0 0 -0.5 0.5 1	(16) -0.214 eV	0 0 0 -0.75 0.75 0.75	(17) -0.398 eV	0 0 0 0.25 0.25 1.25
(18) 0.610 eV	0.25 0.25 0.25 0.25 1.25 1.25	(19) 0.091 eV	0 0 0 0 1 1	(20) 0.430 eV	0 0 0 -0.25 0.75 1.25
(21) 0.076 eV	0.25 0.25 0.25 0.25 0.25 1.75	(22) 1.176 eV	0.25 0.25 0.25 -0.25 1.25 1.25	(23) 0.045 eV	0.25 0.25 0.25 0.75 1.25 1.25
(24) 0.030 eV	0 0 0 0 0.5 1.5	(25) 0.299 eV	0 0 0 0.75 0.75 1.25	(27) 0.045 eV	0 0 0 0.25 1.25 1.25
(28) -0.229 eV	0 0 0 0.25 0.25 1.75	(29) -0.036 eV	0 0 0 0.5 1 1.5	(30) -0.122 eV	0 0 0 0.75 1.25 1.25

Table B.1: The table lists the pair clusters of the cv score minimizing cluster expansion with their labels (in parenthesis) and the ECI with multiplicity included.

(31)	0 0 0	(32)	0 0 0	(33)	0 0 0
-0.402	0.25 0.25 0.25	-0.138	0.25 0.25 0.25	-0.028	0 0.5 0.5
eV	-0.25 0.25 0.25	eV	-0.25 -0.25 -0.25	eV	0.25 0.25 0.25
(34)	0 0 0	(35)	0.25 0.25 0.25	(36)	0 0 0
-0.304	0.25 0.25 0.25	-0.070	0.25 0.75 0.75	0.159	-0.25 0.25 0.75
eV	-0.25 -0.25 0.25	eV	0.25 0.25 0.75	eV	-0.25 0.25 0.25
(38)	0 0 0	(39)	0 0 0	(40)	0.25 0.25 0.25
0.089	0 0.5 0.5	-0.264	-0.25 0.25 0.75	0.292	0.25 0.75 0.75
eV	-0.25 0.25 0.75	eV	0.25 0.25 0.25	eV	0.75 0.75 0.75
(41)	0.25 0.25 0.25	(44)	0.25 0.25 0.25	(47)	0 0 0
0.097	0.25 0.75 0.75	0.219	0.25 0.75 0.75	-0.164	-0.25 0.25 0.75
eV	-0.25 0.75 0.75	eV	0.75 0.25 0.75	eV	0.25 -0.25 0.25
(51)	0 0 0	(58)	0.25 0.25 0.25	(59)	0 0 0
-0.546	-0.25 0.25 0.75	-0.208	0.25 0.25 1.25	-0.032	0.25 0.75 0.75
eV	-0.25 0.25 -0.25	eV	0.25 0.75 0.75	eV	-0.25 0.25 0.25
(60)	0 0 0	(63)	0.25 0.25 0.25	(69)	0.25 0.25 0.25
0.097	0.25 0.75 0.75	-0.213	0.25 0.75 0.75	0.094	0.75 0.75 0.75
eV	0.25 0.25 0.75	eV	0.25 -0.25 -0.25	eV	-0.25 0.25 0.25
(74)	0.25 0.25 0.25	(77)	0 0 0	(79)	0.25 0.25 0.25
-0.867	0.25 0.25 1.25	0.135	0.25 0.75 0.75	0.157	0.25 0.25 1.25
eV	0.25 0.75 1.25	eV	0.25 -0.25 0.25	eV	-0.25 0.75 0.75
(83)	0 0 0	(86)	0 0 0	(88)	0 0 0
0.042	0 0.5 0.5	0.202	0.25 0.25 1.25	-0.012	0.25 0.75 0.75
eV	0.25 0.25 1.25	eV	-0.25 0.25 0.75	eV	0.5 0.5 1
(89)	0 0 0	(91)	0.25 0.25 0.25	(92)	0 0 0
0.200	0.25 0.75 0.75	-0.204	0.25 0.75 0.75	-0.020	-0.25 0.25 0.75
eV	-0.25 -0.25 0.25	eV	0.5 -0.5 0	eV	0.5 0.5 1
(96)	0.25 0.25 0.25	(97)	0 0 0	(98)	0 0 0
-0.216	0.25 0.75 1.25	0.028	0 0.5 0.5	0.101	0.25 0.75 0.75
eV	0.75 0.25 0.25	eV	0.75 -0.25 0.75	eV	0.75 0.25 0.75
(99)	0.25 0.25 0.25	(104)	0 0 0	(110)	0.25 0.25 0.25
-0.779	0.25 0.75 0.75	0.383	0.25 0.75 0.75	-0.166	0.25 0.75 1.25
eV	-0.25 -0.25 -0.25	eV	0.75 0.75 0.75	eV	0.25 -0.25 0.75
(111)	0 0 0	(112)	0 0 0	(113)	0 0 0
0.040	0.25 0.25 1.25	-0.085	0 1 1	-0.132	0.25 0.75 0.75
eV	-0.25 -0.25 0.75	eV	0.25 0.75 0.75	eV	0.25 -0.25 -0.25
(116)	0.25 0.25 0.25	(117)	0 0 0	(121)	0 0 0
0.073	-0.25 0.75 0.75	-0.062	0.25 0.75 0.75	-0.075	0.25 0.25 1.25
eV	0.75 -0.25 -0.25	eV	-0.25 -0.25 -0.25	eV	0.5 0.5 1
(122)	0 0 0	(125)	0 0 0	(126)	0.25 0.25 0.25
0.231	0.25 0.25 1.25	0.167	-0.25 0.25 0.75	0.061	0.75 0.75 0.75
eV	-0.25 -0.25 0.25	eV	0.25 0.75 1.25	eV	-0.25 -0.25 0.75

Table B.2: The table lists the triplets of the cv score minimizing cluster expansion with their labels (in parenthesis) and the ECI with multiplicity included.

(129)	0 0 0	(130)	0 0 0	(134)	0.25 0.25 0.25
0.096	0.25 0.25 1.25	0.174	0.25 0.25 1.25	-0.252	0.25 0.75 1.25
eV	-0.5 0 0.5	eV	0.25 0.75 0.75	eV	0.25 0.25 -0.25
(136)	0.25 0.25 0.25	(137)	0.25 0.25 0.25	(142)	0 0 0
-0.213	0.25 0.25 1.25	0.303	0.25 0.75 1.25	0.148	0.25 0.25 1.25
eV	0.25 0.75 -0.25	eV	-0.25 -0.25 0.75	eV	-0.25 0.75 0.75
(145)	0.25 0.25 0.25	(149)	0.25 0.25 0.25	(150)	0 0 0
-0.012	0.25 0.25 1.25	-0.270	0.25 0.75 1.25	0.040	0 0.5 0.5
eV	0 1 0	eV	0.75 -0.25 0.25	eV	1.25 0.25 0.25
(151)	0 0 0	(152)	0.25 0.25 0.25	(154)	0 0 0
0.163	0.25 0.25 1.25	0.242	0.25 0.25 1.25	0.080	-0.25 0.25 0.75
eV	0.25 0.25 -0.25	eV	0 0.5 -0.5	eV	1 0.5 0.5
(155)	0 0 0	(156)	0 0 0	(161)	0.25 0.25 0.25
-0.035	0.25 0.25 1.25	-0.054	0 1 1	-0.198	0.25 0.25 1.25
eV	-0.25 0.75 0.25	eV	0.5 0.5 1	eV	0.25 1.25 0.25
(162)	0.25 0.25 0.25	(164)	0 0 0	(165)	0 0 0
0.181	0.25 0.75 1.25	0.176	0.25 0.25 1.25	-0.176	-0.25 0.25 0.75
eV	-0.25 0.25 -0.25	eV	-0.25 0.25 -0.25	eV	0.25 1.25 0.75
(166)	0 0 0	(171)	0 0 0	(176)	0 0 0
0.059	-0.25 0.25 0.75	-0.014	0 0 1	-0.195	0 0.5 0.5
eV	0.75 0.25 1.25	eV	0.5 1 0.5	eV	1.25 0.25 0.75
(178)	0.25 0.25 0.25	(179)	0.25 0.25 0.25	(182)	0.25 0.25 0.25
0.168	0.25 0.75 1.25	-0.179	0.25 0.75 1.25	0.024	0.25 0.75 1.25
eV	0.75 0.75 -0.25	eV	1 0 0	eV	0.5 0 -0.5
(188)	0 0 0	(192)	0 0 0	(193)	0 0 0
-0.085	0.25 0.25 1.25	0.033	0.25 0.75 0.75	0.020	0 0 1
eV	0.75 0.75 0.25	eV	1.25 0.25 0.75	eV	0.75 0.75 -0.25
(194)	0.25 0.25 0.25	(196)	0 0 0	(197)	0 0 0
-0.047	0.25 0.25 1.25	-0.089	0 1 1	0.038	0 1 1
eV	1 1 0	eV	0.25 -0.25 -0.25	eV	0 -0.5 0.5
(198)	0 0 0	(200)	0 0 0	(201)	0 0 0
0.072	0.25 0.25 1.25	-0.041	0.25 0.25 1.25	0.032	-0.25 0.25 0.75
eV	0 0.5 -0.5	eV	-0.25 0.75 -0.25	eV	0.75 1.25 0.25
(202)	0 0 0	(205)	0 0 0	(206)	0 0 0
-0.156	-0.25 0.25 0.75	-0.089	0 1 1	0.094	0 1 1
eV	1.25 0.25 0.75	eV	0.75 -0.25 0.25	eV	0.75 0.25 1.25
(208)	0 0 0	(209)	0 0 0	(211)	0 0 0
0.111	-0.25 0.25 0.75	-0.135	0.25 0.25 1.25	0.100	0 0 1
eV	1.25 0.75 0.25	eV	0.25 1.25 0.25	eV	0.75 1.25 0.25
(216)	0 0 0				
0.061	0 1 1				
eV	1.25 0.25 0.25				

Table B.3: Table B.3 is a continuation of table B.2.

Appendix C

Cation coordination clusters

Each graph in the following six figures plots the probability deviation from random for a given cluster occupation versus the formation energies in a set of structures having the same composition. Equation 4.1 defines the probability deviation from random and section 4.2 discusses the results. The compositions of interest are 22, 33, 44, 50, 67, and 75 % $YO_{1.5}$ doping in ZrO_2. The clusters are a cation tetrahedron with an oxygen or vacancy (V) in the center with the following occupations: V-1Y-3Zr, V-2Y-2Zr, V-3Y-1Zr, O-1Y-3Zr, O-2Y-2Zr, and O-3Y-1Zr.

The last figure in the appendix is the average cation relaxation around oxygen for the structures at each composition.

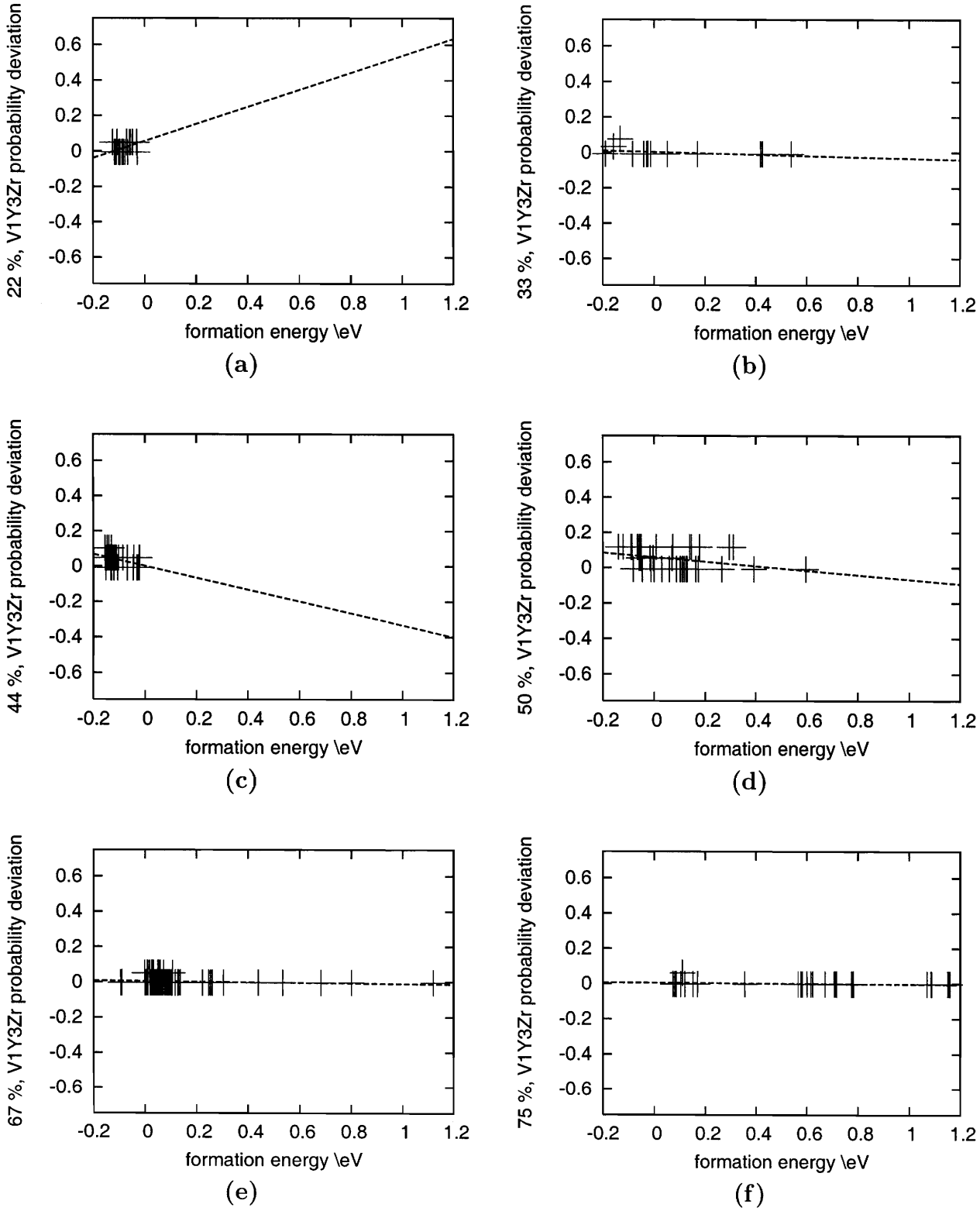

Figure C-1: The probability deviation from random for a vacancy coordinated by one yttrium and three zirconium.

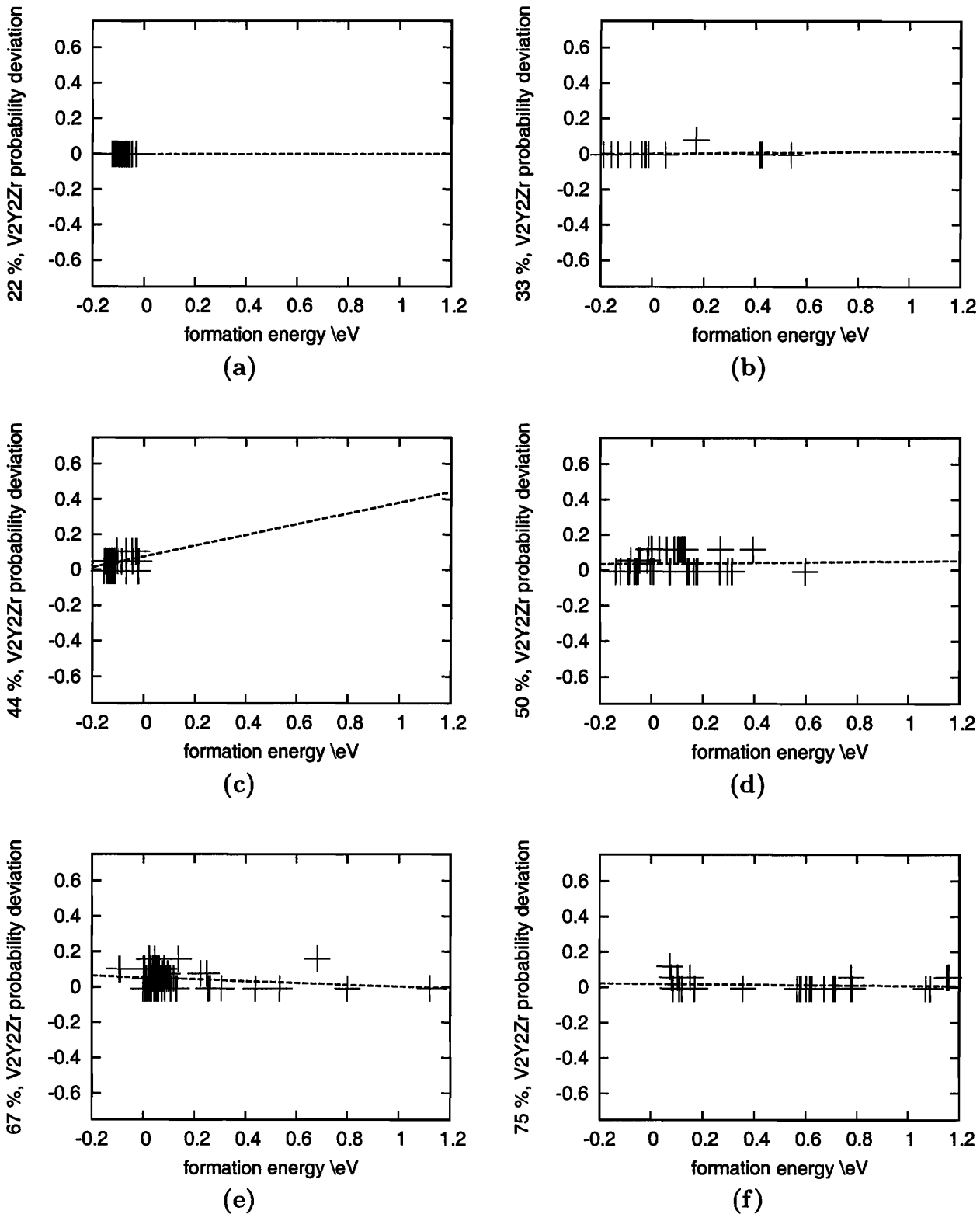

Figure C-2: The probability deviation from random for a vacancy coordinated by two yttrium and two zirconium.

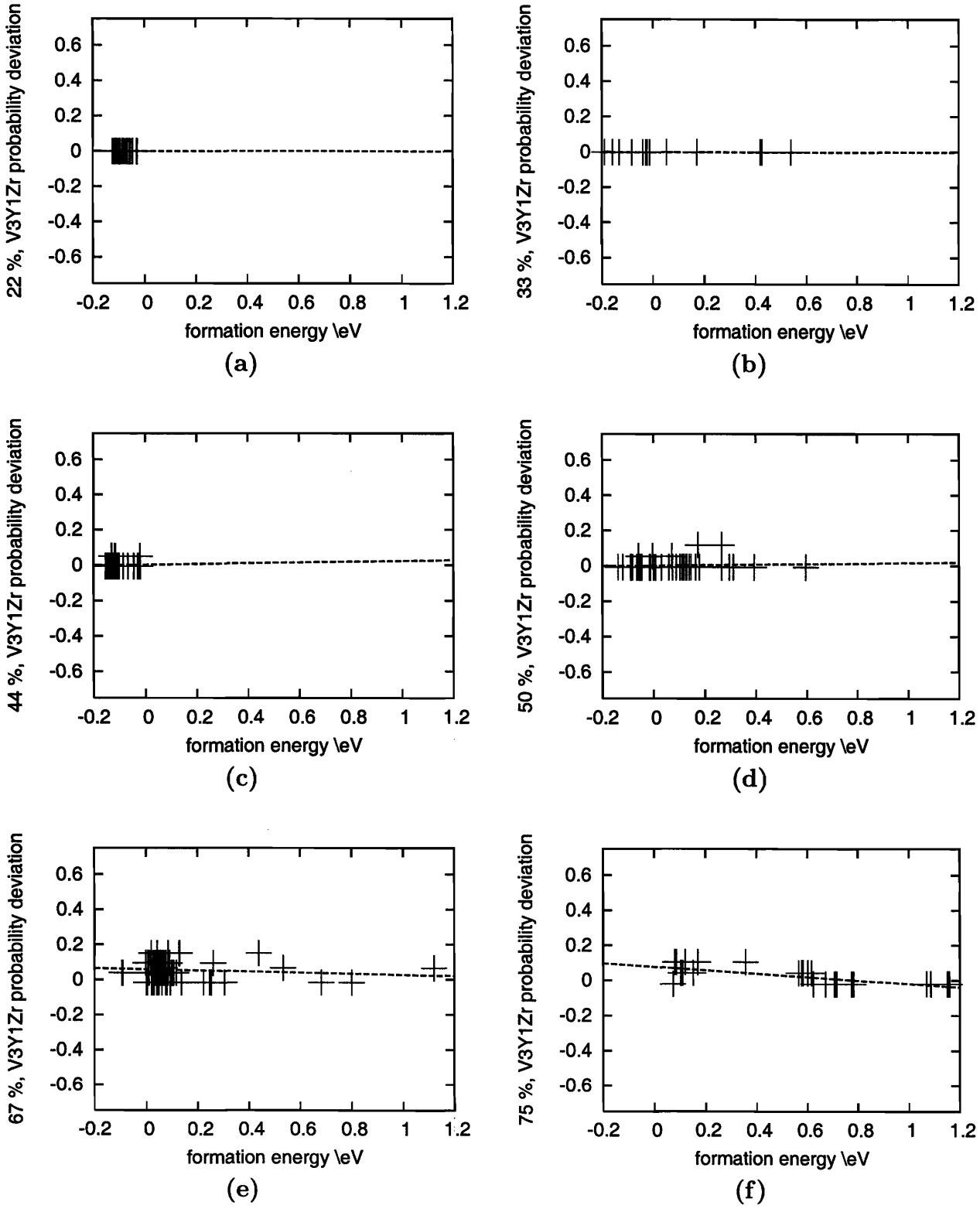

Figure C-3: The probability deviation from random for a vacancy coordinated by three yttrium and one zirconium.

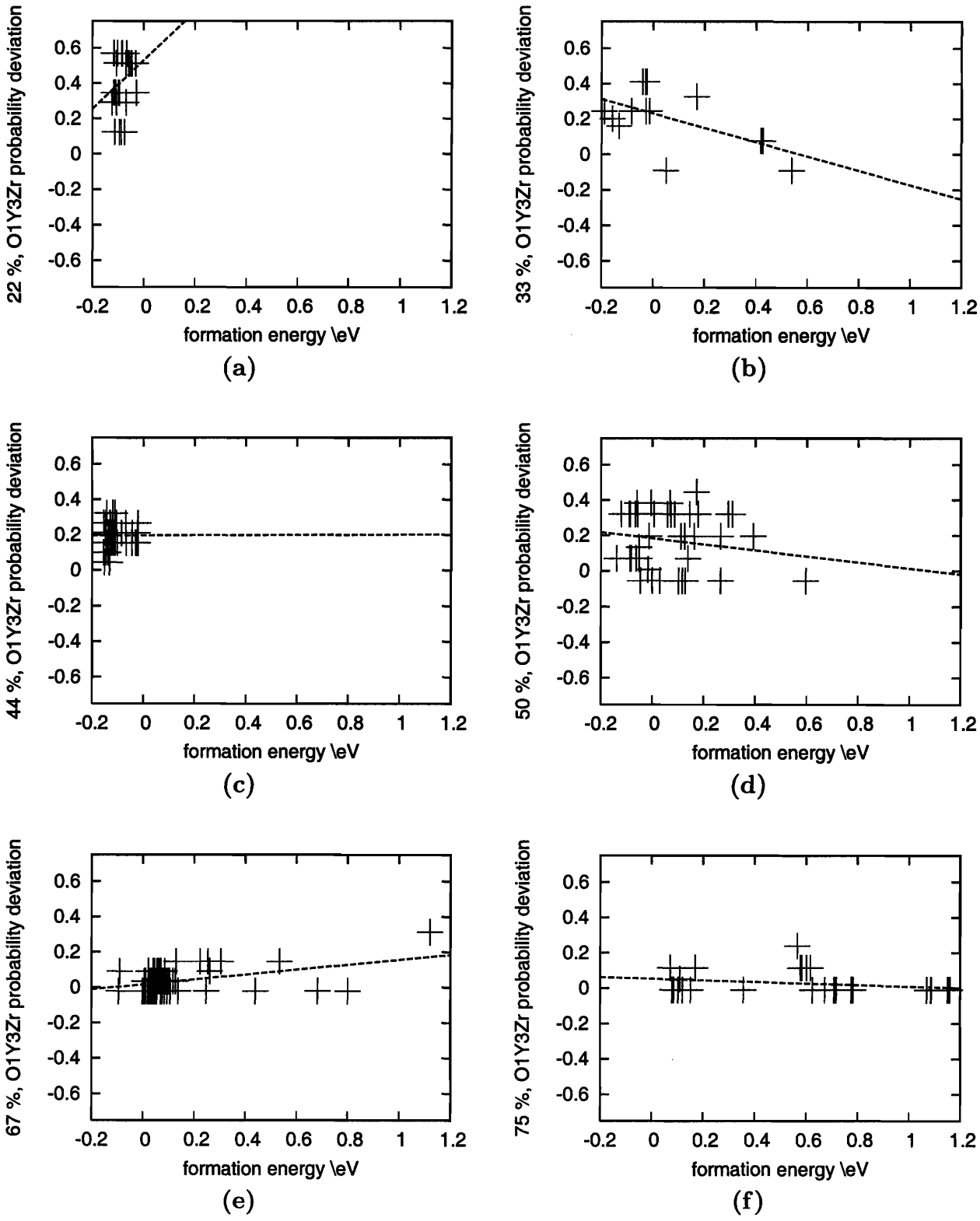

Figure C-4: The probability deviation from random for an oxygen coordinated by one yttrium and three zirconium.

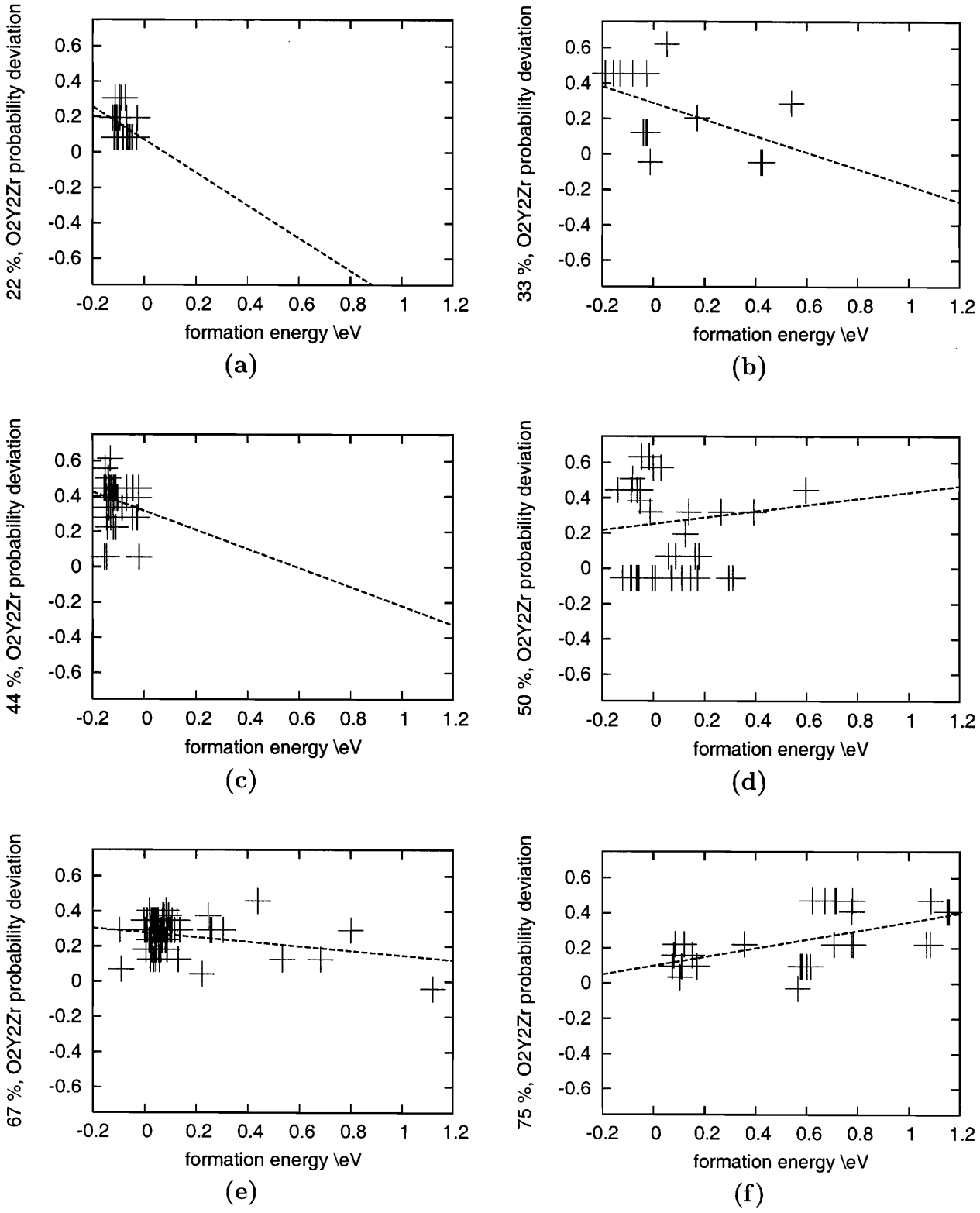

Figure C-5: The probability deviation from random for an oxygen coordinated by two yttrium and two zirconium.

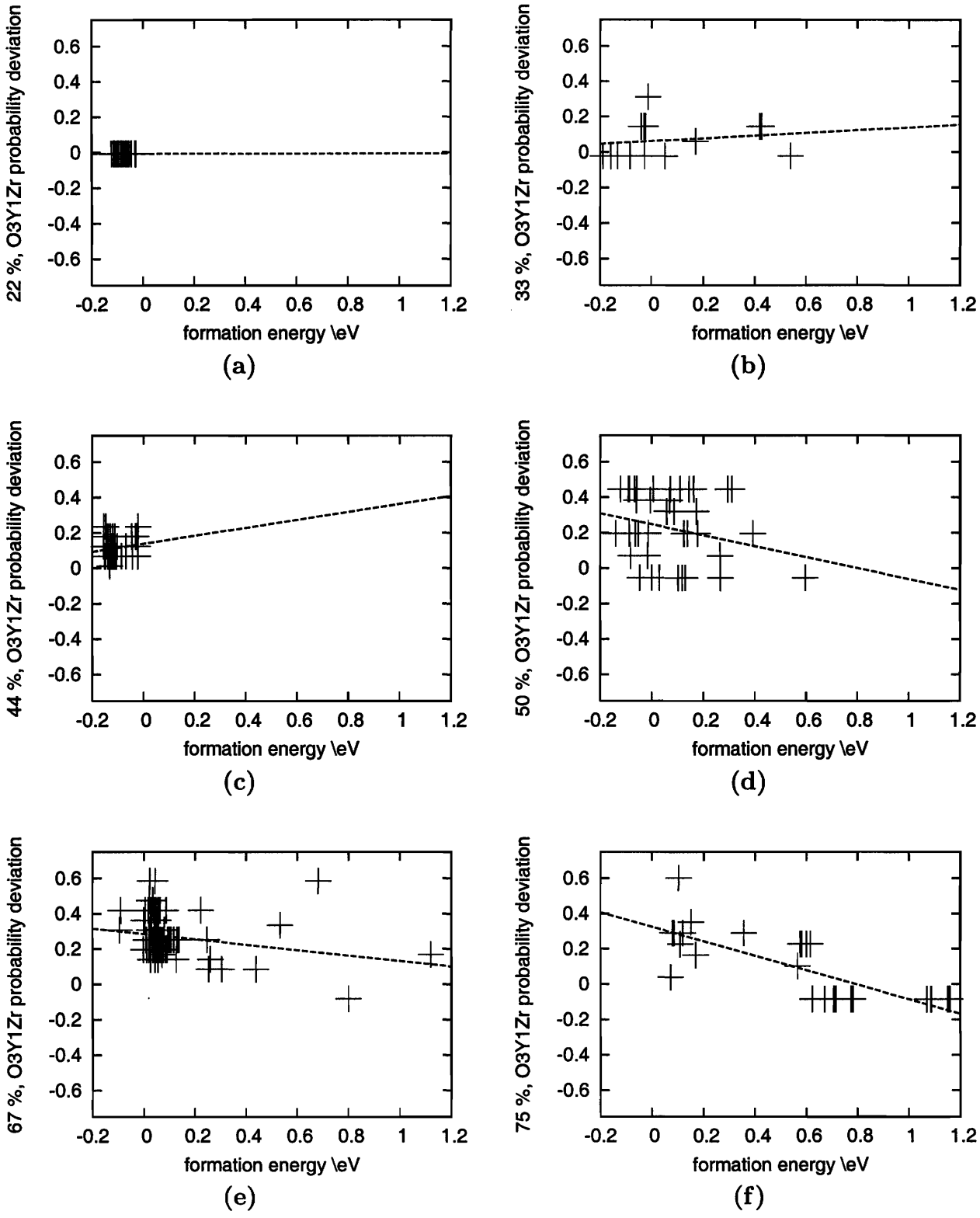

Figure C-6: The probability deviation from random for an oxygen coordinated by three yttrium and one zirconium.

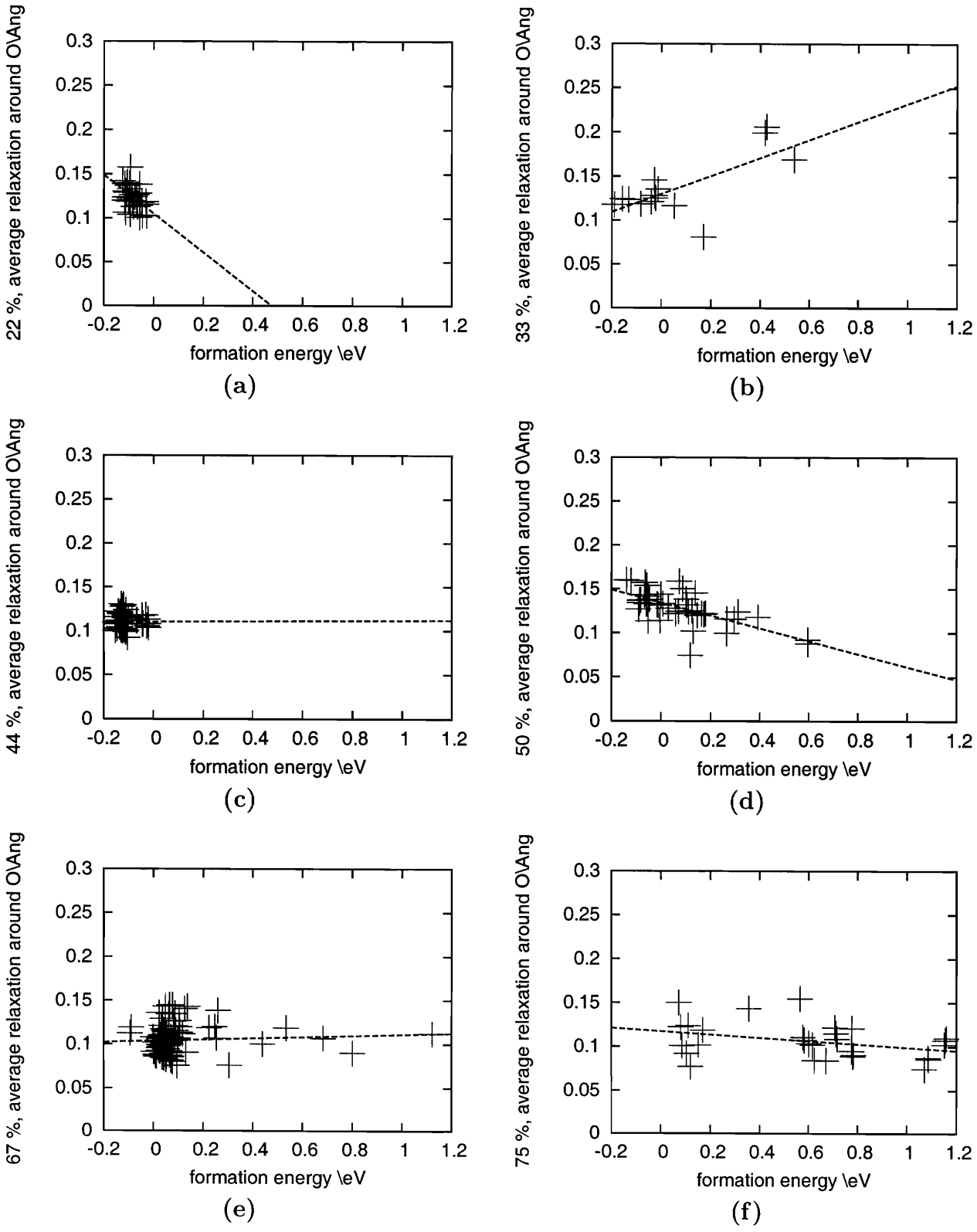

Figure C-7: The average relaxation of cations around oxygen for the six compositions of interest.

Bibliography

[1] I. D. Brown and D. Altermatt. Bond-valence parameters obtained from a systematic analysis of the inorganic crystal structure database. *Acta Crystallographica*, B41:244, 1969.

[2] R. Shannon and C. Prewitt. Effective ionic radii in oxides and fluorides. *Acta Crystallographica*, B25:925, 1969.

[3] M. Kilo, C. Fundenberger, C. Argirusis, M. Taylor, G. Borshardt, M. Weller, and R. Jackson. Experimental and theoretical investigation of oxygen diffusion in stabilised zirconia. *Radiation Effects and Defects in Solids*, 157:1077, 2002.

[4] M. Kilo, C. Argirusis, G. Borshardt, and R. Jackson. Oxygen diffusion in yttria stabilised zirconia - experimental results and molecular dynamics calculations. *Physical Chemistry Chemical Physics*, 5:2219, 2003.

[5] M. Martin. The influence of cation and vacancy distributions on the ionic conductivity of acceptor doped oxygen ion conductors. *Zeitschrift fur Physikalische Chemie*, 219:105, 2005.

[6] V. Zavodinsky. The mechanism of ionic conductivity in stabilized cubic zirconia. *Physics of the Solid State*, 46:453, 2004.

[7] M. Khan, M. Islam, and D. Bates. Cation doping and oxygen diffusion in zirconia: a combined atomistic simulation and molecular dynamics study. *Journal of Materials Chemistry*, 8:2299, 1998.

[8] R. Krishnamurthy, Y. Yoon, D. Srolovitz, and R. Car. Oxygen diffusion in yttria-stabilized zirconia: a new simulation model. *Journal of the American Ceramic Society*, 87:1821, 2004.

[9] M. Kilo, R. Jackson, and G. Borshardt. Computer modelling of ion migration in zirconia. *Philosophical Magazine*, 83:3309, 2003.

[10] J. Goff, W. Hayes, S. Hull, M. Hutchings, and K. Claussen. Defect structure of yttria-stabilized zirconia and its influence on the ionic conductivity at elevated temperatures. *Physical Review B*, 59(22):14202, June 1999.

[11] S. Fabris, A. Paxton, and M. Finnis. Relative energetics and structural properties of zirconia using a self-consistent tight binding model. *Physical Review B*, 61:6617, 2000.

[12] K. Gschneidner, Jr. and L. Eyring, editors. *Handbook on the physics and chemistry of rare earths - Volume 3 - Non-metallic compounds.* North-Holland, Amsterdam, 1979.

[13] S. Ray and V. Stubican. Neutron diffraction investigation of $zr_3y_4o_{12}$. *Materials Research Bulletin*, 15:1419, 1980.

[14] H. Scott. The yttria-zirconia δ phase. *Acta Crystallographica*, B33:281, 1977.

[15] G. Baldinozzi, J. Berar, and G. Calvarin. Reitveld refinement of two-phase Zr-doped Y_2O_3. *Materials Science Forums*, 278-281:680, 1998.

[16] J. Calderon-Moreno and M. Yoshimura. Characterization by Raman spectroscopy of solid solutions in the yttria-rich side of the zirconia-yttria system. *Solid State Ionics*, 154-155:125, 2002.

[17] C. Pascual and P. Duran. Subsolidus phase equilibria and ordering in the system ZrO_2-Y_2O_3. *Journal of the American Cermamic Society*, 66:23, 1982.

[18] H. Scott. Phase relationships in the zirconia-yttria system. *Journal of Materials Science*, 10:1527, 1975.

[19] H. Scott. Phase relationships in the yttria-rich part of the yttria-zirconia system. *Journal of Materials Science*, 12:311, 1977.

[20] V. Stubican, R. Hink, and S. Ray. Phase equilibria and ordering in the system ZrO_2-Y_2O_3. *Journal of the American Ceramic Society*, 61:17, 1978.

[21] Y. Du, Z. Jin, and P. Huang. Thermodynamic assessment of the ZrO_2-$YO_{1.5}$ system. *Journal of the American Ceramic Society*, 74(7):1569–77, 1991.

[22] M. Chen, B. Hallstedt, and L. Gauckler. Thermodynamic modeling of the ZrO_2-$YO_{1.5}$ system. *Solid State Ionics*, 170:255–274, 2004.

[23] A. van der Ven. *First Principles Investigation of Thermodynamic and Kinetic Properties of Lithium Transition Metal Oxides.* PhD thesis, Massachusetts Institute of Technology, 2000.

[24] D. de Fontaine. *Solid State Physics: Advances in Research and Applications*, volume 47, chapter 2: Cluster Approach to Order-Disorder Transformations in Alloys, pages 33–176. Academic Press, San Diego, 1994. Henry Ehrenreich, David Turnbul, editors.

[25] J. Sanchez, F. Ducastelle, and D. Gratias. Generalized cluster description of multicomponent systems. *Physica A*, 128:334, 1984.

[26] C. Kittel. *Introduction to Solid State Physics.* Wiley, New York, 1986.

[27] L. Ferreira, S. Froyen, and A. Zunger. Efficient cluster expansion for substitutional systems. *Physical Review B*, 46:12587, 1992.

[28] C. Wolverton and A. Zunger. Ising-like description of structurally relaxed ordered and disordered alloys. *Physical Review Letters*, 75:3162, 1995.

[29] A. Zunger, L. Wang, G. Hart, and M. Sanati. Obtaining Ising-like expansions for binary alloys from first principles. *Modelling and Simulation n Materials Science and Engineering*, 10:685–706, 2002.

[30] N. Marzari, S. de Gironcoli, and S. Baroni. Structure and phase stability of $Ga_xIn_{1-x}P$ solid solutions from computational alchemy. *Physical Review Letters*, 72:4001, 1994.

[31] C. L. Mallow. Some comments on c_p. *Technometrics*, 15:661–675, 1973.

[32] A. J. Miller. *Subset selection in regression.* Number 95 in Monographs on statistics and applied probability. Chapman and Hall/CRC, Boca Raton, 2nd edition, 2002.

[33] B. Efron. Estimating the error rate of a prediction rule: Improvement on cross-validation. *Journal of the American Statistical Association*, 78:316–331, 1983.

[34] M. Stone. An asymptotic equivalence of choice of model by cross-validation and akaike's criterion. *Journal of the Royal Statistical Society*, 39:44–47, 1977.

[35] Ker-Chau Li. Asymptotic optimality of c_p, c_l, cross-validation and generalized cross-validation: Discrete index set. *The Annals of Statistics*, 15(3):958, 1987.

[36] Jun Shao. Linear model selection by cross-validation. *Journal of the American Statistical Association*, 88(422):486, 1993.

[37] A. van de Walle and G. Ceder. Automating first-principles phase diagram calculations. *Journal of Phase Equilibria*, 23(4):348–359, 2002.

[38] P. Tepesch. *Atomistic Modeling of Ceramic Materials: Predicting Crystal Structures, Thermodynamic Properties, and Diffusion Behavior.* PhD thesis, Massachusetts Institute of Technology, 1996.

[39] F. Ducastelle. *Order and Phase Stability in Alloys.* North-Holland, New York, 1991.

[40] A. Bogicevic, C. Wolverton, G. Crosbie, and E. Stechel. Defect ordering in aliovalently doped cubic zirconia from first principles. *Physical Review B*, 64:014106, 2001.

[41] M. Wall, A. Rechtsteiner, and L. Rocha. *A practical approach to microarray data analysis*, chapter Singular value decomposition and principal component analysis, pages 91–109. LANL LA-UR-02-4001. Kluwer, Norwell, MA, 2003. D. Berrar and W. Dubitzky and M. Granzow, editors.

[42] W. Press, S. Teukolsky, W. Vetterling, and B. Flannery. *Numerical Recipes in C: The Art of Scientific Computing*, chapter 2.6 Singular Value Decomposition, pages 59–70. Cambridge University Press, 2 edition, 1992.

[43] B. Bowerman and R. O'Connell. *Linear Statistical Models: An Applied Approach.* PWS-KENT Publishing, Boston, 1990.

[44] D. Bertsimas and J. Tsitsiklis. *Introduction to Linear Optimization.* Athena Scientific, 1997.

[45] A. Bogicevic and C. Wolverton. Elastic reversal of electrostatically driven defect ordering in stabilized zirconia. *Europhysics Letters*, 56(3):393–399, Nov. 2001.

[46] A. Bogicevic and C. Wolverton. Nature and strength of defect interactions in cubic stabilized-zirconia. *Physical Review B*, 67(2):24106, Jan. 2003. pages 1-13.

[47] The author acknowledges Tim Mueller for the Monte Carlo algorithm. He wrote and implemented the Monte Carlo code to choose cv-score minimizing clusters for the cluster expansion.

[48] H. Ondik and H. McMurdie, editors. *Phase diagrams for zirconium and zirconia systems.* American Cermic Society, Westerville, OH, 1998.

[49] S. Fabris, A. Paxton, and M. Finnis. A stabilization mechanism of zirconia based on oxygen vacancies only. *Acta Materialia*, 50:5171–5178, 2002.

[50] S. Ostanin and E. Salamatov. Microscopic mechanism of stability in yttria-doped zirconia. *JETP Letters*, 74(11):552–555, 2001.

[51] F. Frey, H. Boysen, and I. Kaiser-Bischoff. Diffuse scattering and disorder in zirconia. *Zeitschrift fur Kristallographie*, 220:1017, 2005.

[52] D. Steele and B. Fender. The structure of cubic ZrO_2:$YO_{1.5}$ solid solutions by neutron scattering. *J. Phys. C: Solid State Phys.*, 7:1–11, 1974.

[53] D Argyriou, M. Elcombe, and A. Larson. A neutron scattering investigation of cubic stabilised zirconia (CSZ) - I. the average structure of Y-CSZ. *J. Phys. Chem. Solids*, 57(2):183–193, 1996.

[54] M. Morinaga and J. B. Cohen. X-ray diffraction study of $Zr(Ca,Y)O_{2-x}$. I. The average structure. *Acta Crystallographica*, A35:789–795, 1979.

[55] N. Ishizawa, Y. Matsushima, M. Hayashi, and M. Ueki. Synchrotron radiation study of yttria-stabilized zirconia, $Zr_{0.758}Y_{0.242}O_{1.879}$. *Acta Cryst B*, 55:726–735, 1999.

[56] C. Catlow, A. Chadwick, G. Greaves, and L. Moroney. EXAFS study of yttria-stabilized zirconia. *J. Am. Ceram. Soc.*, 69(3):272–77, 1986.

[57] K. McClellan, S.-Q. Xiao, K. Lagerlof, and A. Heuer. Determination of the structure of the cubic phase in high-zro2 Y_2O_3-ZrO_2 alloys by convergent-beam electron diffraction. *Philosophical Magazine A*, 70(1):185–200, 1994.

[58] S. Suzuki, M. Tanaka, and M. Ishigame. Structural studies in ZrO_2-Y_2O_3 system by electron diffraction and electron microscopy I. *Japanese Journal of Applied Physics, Part 1*, 24:401–410, 1985.

[59] S. Suzuki, M. Tanaka, and M. Ishigame. Structural studies in ZrO_2-Y_2O_3 system by electron diffraction and electron microscopy II. *J. Phys. C: Solid State Phys*, 20:2963–2972, 1987.

[60] S. Suzuki, M. Tanaka, and M. Ishigame. Structural studies in ZrO_2-Y_2O_3 system by electron diffraction and electron microscopy III. *Japanese Journal of Applied Physics*, 26(12):1983–1987, 1987.

[61] T. Welberry, R. Withers, J. Thompson, and B. Butler. Diffuse scattering in yttria-stabilized zirconia. *Journal of Solid State Chemistry*, 100:71–89, 1992.

[62] G. Stapper, M. Bernasconi, N. Nicoloso, and M. Parrinello. Ab initio study of structural and elecronic properties of yttria-stabilized cubic zirconia. *Physical Review B*, 59(2):797–810, January 1999.

[63] M. Morinaga and J. B.Cohen. X-ray diffraction study of $Zr(Ca,Y)O_{2-x}$. II. Local ionic arrangements. *Acta Crystallographica*, A36:520–530, 1980.

[64] M. Tuilier, J. Dexpert-Ghys, H. Dexpert, and P. Lagarde. X-ray absorption study of ZrO_2-Y_2O_3 system. *Journal of Solid State Chemistry*, 69:153–161, 1987.

[65] F. Parmigiani, L. Depero, L. Sangaletti, and G. Samoggia. An XPS study of yttria-stabilised zirconia single crystals. *Journal of Electron Spectroscopy and Related Phenomena*, 63:1–10, 1993.

[66] C. Catlow, A. Chadwick, A. Cormack, G. Greaves, M. Leslie, and L. Moroney. The defect structure of yttria stabilized zirconia. In *Materials Research Society Symposium Proceedings*, volume 60, pages 173–178, 1986.

[67] P. Li, I. Chen, and J. Penner-Hahn. X-ray-absorption studies of zirconia polymorphs. II. Effect of Y_2O_3 dopant on ZrO_2 structure. *Physical Review B*, 48(14):10074–10081, 1993.

[68] P. Li, I. Chen, and J. Penner-Hahn. X-ray-absorption studies of zirconia polymorphs. I. Characteristic local structures. *Physical Review B*, 48(14):10063–10073, 1993.

[69] P. Li, I. Chen, and J. Penner-Hahn. X-ray-absorption studies of zirconia polymorphs. III. Static distortion and thermal distortion. *Physical Review B*, 48(14):10082–10089, 1993.

[70] P. Li, I. Chen, and J. Penner-Hahn. Effect of dopants on zirconia stabilization - an x-ray absorption study: I, trivalent dopants. *Journal of the American Ceramic Society*, 77(1):118–128, 1994.

[71] P. Li, I. Chen, and J. Penner-Hahn. Effect of dopants on zirconia stabilization - an x-ray absorption study: II, tetravalent dopants. *Journal of the American Ceramic Society*, 77(5):1281–1288, 1994.

[72] P. Li, I. Chen, and J. Penner-Hahn. Effect of dopants on zirconia stabilization - an x-ray absorption study: III, charge compensating dopants. *Journal of the American Ceramic Society*, 77(5):1289–1295, 1994.

[73] S. Ostanin, A. Craven, D. McComb, D. Vlachos, A. Alavi, A. Paxton, and M. Finnis. Electron energy-loss near-edge shape as a probe to investigate the stabilization of yttria-stabilized zirconia. *Physical Review B*, 65:224109, 2002.

[74] M. Zacate, L. Minervini, D. Bradfield, R. Grimes, and K. Sickafus. Defect cluster formation in M_2O_3-doped cubic ZrO_2. *Solid State Ionics*, 128:243–254, 2000.

[75] S. Fabris, A. Paxton, and M. Finnis. Free energy and molecular dynamics calculations for the cubic-tetragonal phase transition in zirconia. *Physical Review B*, 63:094101, 2001.

[76] J. Irvine, A. Feighery, D. Fagg, and S. Garcia-Martin. Structural studies on the optimisation of fast oxide ion transport. *Solid State Ionics*, 136-137:879–885, 2000.

[77] A. Gallardo-Lopez, J. Martinez-Fernandez, and A. Dominguez-Rodriguez. Origin of diffuse electron scattering in yttria-cubic-stabilized zirconia single crystals with 24-32% yttria. *Philosophical Magazine A*, 81(7):1675–1689, 2001.

[78] A. Gallardo-Lopez, J. Martinez-Fernandez, and A. Dominguez-Rodriguez. Contribution to the study of the transition to a superstructure in high yttria content YCSZ. *Journal of the European Ceramic Society*, 22:2821–2825, 2002.

[79] F. Shimojo, T. Okabe, F. Tachibana, M. Kobayashi, and H. Okazaki. Molecular dynamics studies of yttria stabilized zirconia. I. Structure and oxygen diffusion. *Journal of the Physical Society of Japan*, 61:2848, 1992.

[80] F. Shimojo and H. Okazaki. Molecular dynamics studies of yttria stabilized zirconia. I. Microscopic mechanism of oxygen diffusion. *Journal of the Physical Society of Japan*, 61:4106, 1992.

[81] M. Fevre, A. Finel, and R. Caudron. Local order and thermal conductivity in yttria-stabilized zirconia. I. Microstructural investigations using neutron diffuse scattering and atomic-scale simulations. *Physical Review B*, 72:104117, 2005.

[82] D. Hohnke. Ionic conduction in doped zirconia. In Vashishta, Mundy, and Shenoy, editors, *Fast Ion Transport in Solids*, page 669. Elsevier North Holland, 1979.

[83] C. Azzoni, P. Camagni, G. Samoggia, and A. Paleari. Defect structures and electronic properties in cubic stabilized zirconia. *Solid State Ionics*, 60:223–226, 1993.

[84] J. Kondoh, S. Kikuchi, Y. Tomii, and Y. Ito. Effect of aging on yttria-stabilized zirconia. *Journal of the Electrochemical Society*, 145(5):1550–1560, 1998.

[85] J. Kondoh, S. Kikuchi, Y. Tomii, and Y. Ito. Aging and composition dependence of electron diffraction patterns in Y_2O_3-stabilized ZrO_2: Relationship between crystal structure and conductivity. *Physica B*, 262:177–189, 1999.

[86] M. Weller and A. Lakki. Defects in cubic zirconia studied by mechanical loss spectroscopy. *Ber. Bunsenges. Phys. Chem.*, 101(9):1297–1302, 1997.

[87] J. Rao, Y. Zhou, and D. Li. Long periodic structure in ZrO_2-Y_2O_3 ceramics. *J. Mater. Sci. Technol.*, 20(2):226–227, 2004.

[88] G. Ceder. *Alloy Theory and Its Applications to Long Period Superstructure Ordering in Metallic Alloys and High Temperature Superconductors.* PhD thesis, University of California at Berkeley, 1991.

[89] E. Ku, E. Yeo, and B. Wuensch. Crystal chemistry of $Y_2(Zr_ySn_{1-y})_2O_7$ pyrochlore solid solutions and its relation to fast-ion conduction. In *Materials Research Society Symposium Proceedings*, volume 547, pages 327–332, 1999.

[90] B. Králik, E. Chang, and S. Louie. Structural properties and quasiparticle band structure of zirconia. *Physical Review B*, 57:7027, 1998.

[91] J. Jaffe, R. Bachorz, and M. Gutowski. Low-temperature polymorphs of ZrO_2 and HfO_2: A density-functional theory study. *Physical Review B*, 75:144107, 2005.

[92] R. Orlando, C. Pisani, C. Roettie, and E. Stefanovich. *Ab initio* Hartree-Fock study of tetragonal and cubic phases of zirconium dioxide. *Physical Review B*, 45:592, 1992.

[93] E. Stefanovich, A. Shluger, and C. Catlow. Theoretical study of the stabilization of cubic-phase ZrO_2 by impurities. *Physical Review B*, 49:11560, 1994.

[94] M. Wilson, U. Schonberger, and M. Finnis. Transferable atomistic model to describe the energetics of zirconia. *Physical Review B*, 54:9147, 1996.

[95] M. Finnis, A. Paxton, M. Methfessel, and M. van Schilfgaarde. Crystal structures of zirconia from first principles and self-consistent tight binding. *Physical Review Letters*, 81:5149, 1998.

[96] B. Silvi and A. Savin. Classification of chemical bonds based on topological analysis of electron localization functions. *Nature*, 371:683, 1994.

[97] J. Burdett and T. McCormick. Electron localization in molecules and solids: the meaning of ELF. *Journal of Physical Chemistry Part A*, 102:6366, 1998.

[98] I. D. Brown. *The Chemical Bond in Inorganic Chemistry: The Bond Valence Model.* Oxford University Press, New York, 2002.

[99] S. Ho. On the structural chemistry of zirconium oxide. *Materials Science and Engineering*, 54:23–29, 1982.

[100] I. Kaiser-Bischoff, H. Boysen, F. Frey, J. Hoffmann, D. Hohlwein, and M. Lerch. The defect structure of Y- and N-doped zirconia. *Journal of Applied Crystallography*, 38:139–146, 2005.

[101] M. Subramanian, G. Aravamudan, and G. Subba Rao. Oxide pyrochlores - a review. *Progress in Solid State Chemistry*, 15:55, 1983.

[102] C. Heremans, B. Wuensch, J. Stalick, and E. Prince. Fast-ion conducting $Y-2(Zr_yTi_{1-y})_2O_7$ pyrochlores: neutron rietveld analysis of disorder induced by Zr substitution. *Journal of Solid State Chemistry*, 117:108, 1995.

[103] B. Wuensch, K. Eberman, C. Heremans, E. Ku, P. Onnerud, E. Yeo, S. Haile, J. Stalick, and J. Jorgensen. Connection between oxygen-ion conductivity of pyrochlore fuel-cell materials and structural change with composition and temperature. *Solid State Ionics*, 129:111, 2000.

[104] F. Brisse and O. Knop. Pyrochlores. III. X-ray, neutron, infrared, and dielectric studies of $A_2Sn_2O_7$ stannates. *Canadian Journal of Chemistry*, 46:589, 1968.

[105] K. Wurst, E. Schweda, D. Bevan, J. Mohyla, K. Wallwork, and M. Hofmann. Single-crystal structure determination of $Zr_{50}Sc_{12}O_{118}$. *Solid State Sciences*, 5:1491, 2003.

[106] S. R. Searle. *Linear Models.* Wiley, New York, 1971.